UNIVERSITÀ DEGLI STUDI DI TRIESTE

XXXII CICLO DEL DOTTORATO DI RICERCA IN

Scienze della terra, fluidodinamica e matematica. Interazioni e metodiche

Finanziatore della borsa: CNR-INM

Computational hydroacoustic analysis of the BB2 submarine using the advective Ffowcs Williams and Hawkings equation with Wall-Modeled LES

Settore scientifico-disciplinare: **ICAR/01**

DOTTORANDO	**ANDREA ROCCA**
COORDINATORE	**PROF. S. MASET**
SUPERVISORE DI TESI	**PROF. V. ARMENIO**
CO-SUPERVISORE DI TESI	**DR. R. BROGLIA**

ANNO ACCADEMICO 2018/2019

Contacts

Author: Andrea Rocca
e-mail: andrea.rocca@phd.units.it /andrearocca17@gmail.com
Affiliation: Doctoral School in Earth Science, Fluid-Dynamics and Mathematics. Interactions and methods". Dipartimento di Ingegneria e Architettura, University of Trieste, Piazzale Europa 1, I-34127 Trieste, Italy

Supervisor: Prof. Vincenzo Armenio
e-mail: armenio@dia.units.it
Affiliation: Dipartimento di Ingegneria e Architettura, University of Trieste, Piazzale Europa 1, I-34127 Trieste, Italy

Co-Supervisor: Dr. Riccardo Broglia
e-mail: riccardo.broglia@cnr.it
Affiliation: CNR-INM, Instituto di INgegneria del Mare, via di Vallerano, 139 - 00128 Rome, Italy

A. Rocca and soviet Russian submarine in background. Moskva river bank

Day of the defence: 27.10.2020

To cite this work: Andrea Rocca, Computational hydroacoustic analysis of the BB2 submarine using the advective Ffowcs Williams and Hawkings equation with Wall-Modeled LES, Ph.D. Thesis**.**
School of Earth Science, Fluid Mechanics and Mathematics. Interactions and Methods.
University of Trieste (2019).

Digital resource deposited in the National Legal Deposit service. NBN: to be assigned

I dedicate this thesis to the ladies of my life.
To my Mother Paola, who passed away on the 7th of April 2020. We miss you.
To my Wife Marina, who supported me from the beginning with Love and Care.
To my Baby Daria, who is giving us Joy and Strength.

Acknowledgments

I'm deeply in debit with both Prof. Vincenzo Armenio and Dr. Riccardo Broglia.

Ph.D. has been a great experience. It was about study, work and life. I thank them for their help, their teachings and the patience they have shown me. I express my gratitude to CNR-INM for founding my studies.

Besides my supervisors I have to thank many other persons. From university of Trieste I need to express my gratitude to Dr. Petronio and Dr. Roman (I.E. Fluids) and, in particular, to Dr. Marta Cianferra (the hydroacoustic lady of our research group) for her help during these last months. I can not forget all the guys of the laboratory of computational fluid mechanics in Trieste, Santiago, Giulia, Marco, Carlo, Elizabeth, Sara and Ahmad. Thank you all.

I'am deeply in debit with Dr. Joel Guerrero (Wolf Dynamics) for his important help with the OpenFOAM software.

Then I have to thank also Professor Kevin Maki and Dr. Greg Filip of the University of Michigan, for their inspiring work during my short visit in the States.

During my PhD program I took also classes. For this reason I thank Professor Omari for his brilliant way to explain PDEs. Professor Maset and Professor Pedrizzetti for the useful "numerical analysis" course. Professor Armenio for the interesting classes of "Turbulence" and "CFD".

I'am in debit with Dr. Mark C. Bettle (Defence Research and Development Canada) for developing the base topology of the grid.

I also want to express my gratitude to the Italian Ministry of Education and Ministry of University and Research for founding HPC CINECA consortium, in particular I offer my thanks to the support staff of HPC CINECA, an example of professionalism and talent.

I express my thankfulness to Prof. Kranjcevic, Dr. Janes and Dr. Sikirica (University of Rijeka, Croatia) to allow my to use BURA HPC to run my LES and help me with setting up the machine.

Thank you Dr. Michele Potenza (University of Rome "Tor Vergata") for the suggestions about this dissertation.

I also want to thank Dr. Durante and Dr. Posa (CNR-INM of Rome) for the inspiring talks about fluid mechanics.

I feel really lucky to had the chance to listen at Prof. Piomelli, Prof. Sagout, Prof. Balaras and Prof. Verzicco at Von Karman Institute for Fluid Dynamics.

I thank Troyer AG/SPA to offer me the conditions to complete this Ph.D.

Abstract

The research activity reported in this thesis concerns the numerical characterization of the hydrodynamics and the hydroacoustics of a Notional submarine geometry; the selected geometry is the model developed by the Defence Science and Technology Organization (DSTO) currently known as the BB2 submarine. It is representative of a Diesel submarine, with a large casing, two fore fins placed on the side of the sail and an X-form rudder arrangement. Simulations are performed at model scale with flow conditions mimicking those of a classical wind-tunnel test. Preparatory Wall-Resolved and Wall-Modeled Reynolds Averaged Navier-Stokes Simulations (hereafter denoted as WR- and WM-RANS, respectively) have been performed at two speeds, corresponding to length based (model scale) Reynolds numbers of $Re_L = 9.57 \times 10^6$ and $Re_L = 1.2 \times 10^6$. WM-RANS solution was used to initialize Wall-Modeled Large-Eddy Simulation (WMLES) at $Re_L = 1.2 \times 10^6$. For what LES simulation concerns, the grid utilized is composed of approximately 40 million cells. The grid cells in a layer surrounding the submarine surface and in its wake are of hexahedral shape. The hydroacoustic analysis is based on the Acoustic-Analogy (AA), which allows to decouple the fluid dynamic simulation from the acoustic estimation. The acoustic pressure is governed by the Ffowcs Williams and Hawkings (FW-H) equation, that, in the present case, has been considered in its advective formulation, which is the most suitable form for wind-tunnel-like problems. The non-linear quadrupole term is estimated by the fluid-dynamic data from the WMLES. The quasi-axisymmetric turbulent boundary layer predicted by LES exhibits a skin-friction coefficient (C_f) lower compared to a planar turbulent boundary layer under similar conditions, as well as to the WR-RANS solution. On the other hand, WM-RANS overestimates C_f. Concerning the wake, LES predictions are in a good agreement with available data in literature, up to 18 D downstream (with D the diameter of the submarine). In accordance with the equilibrium self-similarity theory, the mean streamwise velocity profiles, when made non-dimensional with the characteristic velocity and length scales of the wake, collapse into a single curve. Moreover, it has been determined that the wake is in a state of evolution to local high-Re regime (i.e. no shift from high- to low-Re solution was observed). Finally, it has been highlighted that, turbulence furnishes the most important contribution to the hydroacoustic noise. The contribution to the noise of the pressure load on the submarine surface results negligible compared to the non-linear effects. Sound pressure level spectra at the sail side are characterized by peak at 1 Hz. High frequency noise increases downstream as result of the eddies breaking up process in the wake.

Sommario

Il lavoro di ricerca riportato nella presente tesi riguarda la caratterizzazione idrodinamica e idroacustica di una geometria non classificata di sottomarino, tramite simulazioni numeriche. La geometria in esame è il modello sviluppato dal ”Defence Science and Technology Organization (DSTO)”, noto come BB2. Questo modello è rappresentativo di un sottomarino diesel, con un largo ”*casing*”, due timoni anteriori posizionati sulla torretta e quattro timoni posteriori disposti ad ”X”. Le simulazioni sono state effettuate in scala modello e le condizioni di flusso sono quelle di un classico test in galleria del vento. Sono state effettuate delle simulazioni preparatorie utilizzando metodologie numeriche basate sulle equazioni di Navier-Stokes mediate alla Reynolds (RANS). Sono stati utilizzati due approcci differenti: in un caso, le equazioni RANS sono state integrate lungo tutta l'altezza dello strato limite (approccio ”wall-resolved”, WR-RANS); nell'altro caso, il comportamento del flusso nella zona vicino alle pareti solide è stato approssimato tramite i cosiddetti ”modelli di parete” (approccio ”wall-modeled”, WM-RANS). Le simulazioni sono state effettuate per due diverse velocità del flusso, alle quali corrispondono i numeri di Reynolds (basati sulla lunghezza del sottomarino, L): $Re_L = 9.57 \times 10^6$ e $Re_L = 1.2 \times 10^6$. La soluzione ottenuta utilizzando l'approccio WM-RANS è stata utilizzata per inizializzare il calcolo della simulazione LES, anch'essa effettuata utilizzando modelli di parete (WMLES); quest'ultima analisi è stata condotta a $Re_L = 1.2 \times 10^6$. Per quanto concerne la simulazione LES, la griglia utilizzata è composta da 40 milioni di celle circa. Le celle della griglia attorno al sottomarino e in scia sono sostanzialmente ortogonali con fattore di forma vicino ad uno. L'analisi idroacustica è basata sulla tecnica delle ”Analogie-Acustiche” (AA) che permette di disaccoppiare la simulazione fluidodinamica dal calcolo acustico. Nell'ambito delle AA, la pressione acustica è governata dall'equazione di Ffowcs Williams e Hawkings (FW-H) che, nel presente lavoro, è stata considerata nella sua formulazione advettiva, adatta all'analisi di problemi con condizioni di flusso simili a quelle di un test in galleria del vento (come nel caso in esame). Il termine di quadrupolo acustico, non lineare, è calcolato a partire dai dati fluidodinamici forniti dalla LES. Lo strato limite, quasi assialsimmetrico, predetto dalla LES esibisce un coefficiente di attrito (C_f) minore rispetto quello di uno strato limite piano, a parità di Reynolds; anche confrontata con la soluzione WR-RANS, la simulazione WMLES mostra una sottostima del contributo viscoso alla resistenza. Al contrario, la RANS con modelli parete mostra una sovrastima del valore di C_f. Per quanto riguarda la scia, le stime fornite dalla LES mostrano un buon accordo con i dati presenti in letteratura; l'accordo è buono anche a notevoli distanze dal sottomarino (fino ad una distanza pari a 18 D a valle del corpo, dove con D si è indicato il diametro del corpo centrale dello scafo). I profili di velocità assiale media, opportunamente scalati con le grandezze caratteristiche della scia (velocità e lunghezza) collassano su un'unica curva, come indicato dalla teoria dell'auto-similarità in equilibrio. Inoltre, è stato osservato che la scia mostra uno stato di evoluzione verso un regime di alto-Reynolds locale; questo vuol dire che non si è osservata nessuna transizione da regime ad alto a regime a basso Reynolds. E' stato infine evidenziato che i moti turbolenti (di dimensioni comparabili con D) forniscono il contributo più importante al rumore idrodinamico. Il rumore provocato dal carico di pressione sulla superficie del sottomarino risulta trascurabile se comprato agli effetti non lineari. Gli spettri della pressione acustica in corrispondenza della torretta sono caratterizzati da un picco alla frequenza di 1Hz. Il rumore alle alte frequenze aumenta a valle del corpo come risultato del processo di evoluzione verso strutture turbolente sempre più piccole, a scapito di quelle di dimensioni maggiori.

Contents

1

Introduction

1.1 Introduction and literature review

The present research work addresses the numerical simulation of the turbulent flow around a notional submarine geometry (namely the BB2 Joubert (2004, 2006)) together with the characterization of its own hydroacoustic signature. This geometry is representative of a Diesel submarine, with a large casing, two fore fins placed on the side of the sail and an X-form rudder arrangement (Overpelt *et al.*, 2015). The BB2 geometry has been chosen since it has been and it is still considered for several experimental and numerical research activity; therefore, a large amount of data are available. Among others, Kumar *et al.* (2012) performed a particle image velocimetry measurements, while Quick *et al.* (2012); Quick & Woodyatt (2014) performed load measurements. Anderson *et al.* (2012) reported accurate skin-friction coefficient measurements (using different tripping strategies), while in Anderson *et al.* (2012); Fureby *et al.* (2016); Lee *et al.* (2019) can be found interesting flow visualization. Moreover, the BB2 is also the object of various CFD studies, as, for example, within the *NATO AVT-301* collaboration group for flow field prediction for maneuvering underwater vehicles (Toxopeus, 2017).

The fluid flow is resolved using Wall-Modeled Large-Eddy Simulation (WMLES) method. WMLES opens to high-fidelity hydroacoustic signature characterization of the submarine, in straight-ahead flight, using the acoustic analogies.

From hydrodynamic and hydroacoustic perspectives, nowadays submarines can be considered among the most complex marine vessels, because of their own intricate fluid dynamics, which is the result of three-dimensional interaction between the sail and hull wakes, the presence of turbulent boundary layer and massive separations. Also, propeller's wake and cavitation phenomenon may represent a rich source of noise and the hydroacoustic signature detection is of fundamental importance for military purposes (Renilson, 2018).

Because of the flow complexity and the importance of minimizing the noise emission, the design of submarines is oriented toward optimization, and the noise generated should not be considered as an unavoidable ”processing waste”. Thus, the development of reliable and accurate predictive tools assumes a central role in the optimization and understanding of hydrodynamics and hydroacoustics of underwater vehicles, and computational sciences are becoming the ”Swiss Army Knife” of design engineers. In particular, among other things, the role of the computational hydroacoustic (CHA) is to investigate the sound generated as a consequence of the solid-flow interaction. CHA is still relatively unexplored respect to CFD.

A very efficient way to deal with this problem is decoupling the fluid-dynamic and the hydro-acoustic solution processes. This is known as *hybrid-approach* and it is alternative to the *direct method*, which requires the direct solution of the *compressible* Navier-Stokes equations, or any approximation of them. To be noted that for incompressible flows, it is not possible to determine the acoustic pressure using an incompressible solver as direct solution; however, when $Ma << 1$, it is still possible to make a comparison between the pressure field from an incompressible solver and the sound pressure from an acoustic solver (Ianniello *et al.*, 2013).

Hybrid-approaches are also known as *acoustic-analogies* (AA). The idea behind the acoustic analogy is that of feeding the hydro-acoustic solver with fluid dynamic fields, constituting the noise source and then to radiate the noise in the far field solving the integral form of an inhomogeneous wave equation. Sir Michael James Lighthill is considered the pioneer of acoustic analogies. He was a British mathematician working in applied science. In his work (Lighthill, 1952) he derived an inhomogeneous wave equation starting from the fundamental principles of fluid mechanics, i.e. mass and momentum conservation laws. Lighthill's work was first extended by Curle (Curle, 1955), who derived a new formulation including solid reflecting boundaries in the flow. Later, thanks to the work of the two English professors Ffowcs-Williams and Hawkings (Ffowcs-Williams & Hawkings, 1969), relative motion between flow and rigid body was included in the formulation. It is worth to underline that it is possible to derive Lighthill and Curle equations starting from the FW-H equation. The original FW-H is a partial differential equation, but generally scientists and engineers prefer to consider its integral formulation that is better suited for numerical implementations. These formulations, known as **Formulations 1** and **1A** (Farassat, 1975, 1981; Farassat & Succi, 1980), are commonly employed in rotor and propeller noise studies. In the FW-H equation (1A), the acoustic pressure is composed of a number of forcing terms: two of them are surface integrals and are calculated on the surface of the solid body. They are the linear terms and represent the noise generated by the fluid displaced by the body in motion (thickness component) and the noise coming from the fluid dynamic pressure acting on the body surface (loading component). The other terms are volume integral and contribute for the non linear sources, namely the pressure and velocity disturbance around the body; they are also known as *quadrupole* terms. Generally, their computation is omitted and the reason is twofold. First of all, these integrals contain terms to be evaluated at specific times (time-delay) depending on the compressibility of the flow, and their evaluation is very expensive in terms of computational time and data storage. For this reason an alternative computationally-cheaper porous formulation has been developed (Lyrintzis, 1994; Francescantonio, 1997). The second reason is more related to history: in Computational AeroAcoustic CAA (developed before than CHA) the non-linear quadrupole term was generally omitted, being in general less important than the linear contribution. In transonic or supersonic regime the difficulties related to the calculation of the quadrupole term was the driving force for the development of the porous formulation. When lately CHA started to gain popularity between researchers, the experience gained in the CAA field was brought uncritically in the hydro-problems (Ianniello *et al.*, 2013), where the speeds are typically very low and the speed of sound is very large. This led to a general underestimation of the noise produced in hydrodynamic applications. Recently Cianferra *et al* (Cianferra *et al.*, 2019*a*) clarified this issue and provided a general criterion for an accurate and efficient evaluation of the quadrupole terms.

To obtain the hydro-acoustic solution using the acoustic analogies it is necessary to get a good hydro-dynamic solution, which successively has to be post-processed by the acoustic solver. In principle one may obtain the fluid-dynamic field through direct numerical simulation (DNS) of the Navier-Stokes equations. Unfortunately this is computationally-unfeasible for most flows in the turbulent regime, since the computational cost increases as $Re^{3.5}$ in wall-bounded turbulence (Re is the Reynolds number of the flow) (Piomelli & Balaras, 2002). On the opposite side, the Reynolds-averaged Navier-Stokes equations either in their steady-state formulation (RANS) or in the unsteady one (URANS) provide the mean turbulent field. In this case the effect of turbulent fluctuations on the acoustic signature is hardly detectable, since the turbulent fluctuations are not resolved at all (in the RANS approach only their effects on the mean flow are considered by a suitable model). In between, Large-Eddy Simulation (LES) or Detached Eddy-Simulation (DES) provide the unsteady 3D turbulent field at a reasonable computational cost even in the high-Re number limit. In LES, the large and energy-carrying scales of turbulence are solved by an unsteady 3D simulation, while the smallest ones, more isotropic and dissipative, are modeled through a suitable subgrid scale parametrization. Without going into details, as discussed in (Piomelli & Balaras, 2002) LES suffers when simulating wall-bounded flows because of the thin viscous sublayer which needs to be resolved. The computational cost required to solve the boundary layer with LES increases with $Re^{2.5}$, a bit less than a that of a DNS, still unaffordable for high Re-number flows. Nowadays this problem is address by modeling the near wall region through the use of special functions (wall-layer models) allowing for a dramatic reduction of the the computational cost up to acceptable levels. In this case the simulation is named Wall-Modeled LES (WMLES). A very recent example of WMLES employed in conjunction with the FW-H equation for the characterization of the acoustic signature of a ship propeller can be found in (Cianferra *et al.*, 2019*b*).

In most applications when dealing with acoustic, the fluid-dynamic field is generally computed solving the Unsteady Reynolds-Averaged Navier-Stokes equations (URANS). In subsonic aeroacoustic the mean flow might be sufficiently accurate for a good acoustic simulation. Using RANS/URANS, most of the important information on the frequency content of the resulting noise is lost (Piomelli *et al.*, 1997). For example, in Ianniello (2016) the authors clearly discuss the reasons why RANS simulations are not adequate for the hydro-acoustic investigation of turbulent flows. This because they are unable to feed the quadruple term with turbulent fluctuating fields, losing the information related to sound generated by turbulence, which in incompressible fluids it is not negligible. At this scope, LES or also DES are promising techniques to apply in the acoustic research field.

Even if computational fluid dynamic is already a mature field, CFD engineers and scientist need experimental data to validate their results. It is very common to simulate wind-tunnels representation of full-scale problems. In this case the ambient medium is in motion and the observer is stationary. A first consequence of this approach are the difficulties arising when comparing experiments carried out in different flow conditions. The second consequence, inherent the CHA, is that the wave equation has to be written in its convective form. Najafy-Yazdi *et al.* (2010) proposed an extension of the two surface integral of FWH-equation and related formulations contained in the works of Farassat (1981) and Farassat & Succi (1980) to sound propagation in moving medium, using a convective form of the wave equation. This is known as **formulation 1C**. Recently Cianferra *et al.* (2019*a*) formulated the volume term of FWH equation in the convective form **formulation 1D**. This allows for avoiding the use of the porous methods which suffers from the choice of the position of the porous surface itself.

Fischer *et al.* (2017) performed aeroacoustic test on a BB2 model using 64 microphones randomly located at the DST Group's Low Speed Wind Tunnel. The model was studied at different pitch and yaw angles and at two flow speeds. Spectra obtained with and without the model in the tunnel were compared and it was observed that the noise from the model is the same as the background except at one single frequency and only for the highest flow speed where a peak is observed when the model is present.

In this work we apply the acoustic-analogy in its **formulation 1D** for the characterization of the hydro-acoustic signature of a fully appended un-propelled BB2 submarine; the flow field is determined before by using WMLES. As mentioned above, the turbulent flow around a submarine, even in a simple straight ahead advancement, is rather complex. Considering the bare hull configuration in straight ahead conditions, starting from the nose of the submarine, a first stagnation point occurs at the bow; here the velocity approaches to zero and the pressure coefficient increases to a maximum. The boundary layer is initially laminar and the flow develops under an adverse pressure gradient. At about $0.1L$ (with L the submarine length) from the bow, the boundary layer undergoes to a transition to turbulent and the pressure gradient in streamwise direction goes rapidly to zero. Despite the circumferential pressure gradient is not uniform, the friction coefficient resembles that of a canonical zero-pressure-gradient turbulent boundary layer flow over a flat plate. Moving downstream, close to the stern, the flow separates and a turbulent

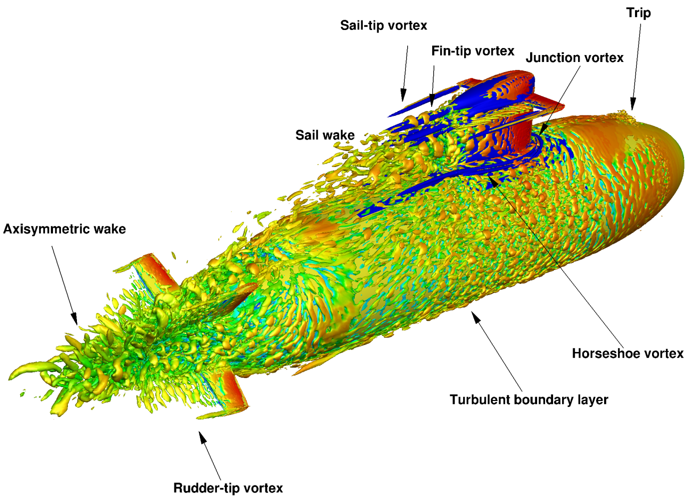

Figure 1.1: Visualization of the turbulent flow around the BB2 submarine at Reynolds number $Re_L = 1.2 \times 10^6$: flow patterns. Iso-surfaces of Q-criterion colored by the pressure coefficient

axisymmetric two-dimensional wake develops. As suggested by Townsend (1956), sufficiently far from the generator the wake reaches a state of moving-equilibrium and becomes self-similar. Under these conditions, the mean velocity profile can be described using a velocity scale u_0 and a length scale l_0 only. The same doesn't hold for the Reynolds stresses that in the wake never attain self-similarity, as discussed in Jiménez *et al.* (2010a), Posa & Balaras (2016) and Kumar & Mahesh (2018). The presence of the appendages makes the flow substantially more complex, as shown in figure 1.1.

The appendages substantially modify the turbulent field compared to an archetypal axial-symmetric body, in fact, the shear layer from the trailing edge of the fins affects the wake. This was shown experimentally by Jiménez *et al.* (2010b) and numerically by Posa & Balaras (2016). Further, the sail on the upper side of the hull generates an adverse pressure gradient that determines the formation of a horse-shoe vortex. This vortex structure surrounds the sail and it is advected downstream by the free stream current, interacting with the boundary layer over the hull. From the top side of the sail, additional vortices develop from the trailing edge and from the widest section of the sail (Fureby *et al.*, 2016). The wake, on the side of the sail, can not be considered axisymmetric due to the sail-wake effect on the velocity deficit at the center line of the wake.

Further, three dimensional vortical structures arise from the sail, from the horizontal hydroplanes and from the rudders, whereas a couple of counter rotating vortices develop from the bottom of the hull. Among these complex processes, turbulent wakes and boundary layers can be considered the fundamental fluid dynamic canonical flows developing around streamlined bodies as submarine ships. The wakes from such vehicles differ from the wakes over bluff bodies attaining self-similarity quicker as suggested by Kumar & Mahesh (2018). Far downstream the stern the wake attains self-similarity and Reynolds number independence. Kumar & Mahesh (2018) showed that for streamlined bodies the axisymmetric wake follows a high-Re equilibrium self-similar solution close to the stern while away from the stern, in a short streamwise distance, it decades to a different low-Re behavior.

From a more practical perspective, wakes can be considered the footprint left by a submarine. They propagates downstream for very long distances leaving an unavoidable trace. This is the reason why the characterization of the wakes is of fundamental importance in military engineering applications.

Numerical simulations of turbulent wakes require a fine computational grid extending far away downstream the body generator. For example, in the recent works of Posa & Balaras (2016) and Kumar & Mahesh (2018), huge grids have been employed to solve the boundary layer up to the viscous sub-layer and to capture the wake till 15 submarine's diameters beyond the stern. The authors investigated the flow of the idealized submarine shape named DARPA Suboff (DSub) (C.Groves *et al.*, 1989), moving straight ahead. The Suboff model is archetypal of a nuclear submarine. Both used LES and, for these reasons, the above mentioned works, can be considered as benchmark cases.

In the past, due to limited computational resources, the majority of the numerical works regarding submarines flow analysis were conducted using Reynolds-averaged Navier-Stokes (RANS) techniques. Today RANS simulation are still largely employed in numerical maneuvering studies for both surface vessels and submarines. For example, (Broglia *et al.*, 2015) performed an in-depth analysis of the maneuverability characteristics of a surface vessel in a conventional twin-rudders twin-skrews configuration and in (G. Dubbioso & Broglia, 2016) for a less conventional single-rudder twin-skrews one. In these works Di Mascio *et al.* (2007); Broglia *et al.* (2014); Dubbioso *et al.* (2017) an in-house developed URANS solver has been used, and then it was coupled with a suitable model for the propellers (Broglia *et al.*, 2013). The same tool has been used for the analysis of the maneuverability of a submarine in two different stern appendage configurations in Dubbioso *et al.* (2017). For what submarine geometries concerns, self-propelled horizontal and vertical maneuvers of the DSub submarine were investigated by Martin *et al.* (2015), whereas, Bettle *et al.* (2009) studied the buoyantly rising maneuver of the DRDC-STR submarine model. Free running maneuvers were investigated in Carrica *et al.* (2016, 2018).

Nowadays the growing availability of High-Performance Computing HPC resources allows investigation of the complex flow field around submarines using DES and even both wall resolved and wall modelled LES. Some interesting works, such those by Alin *et al.* (2010) and Bhushan *et al.* (2013) provide an interesting comparisons between LES, DES and RANS predictions for the DSub geometry. DES and RANS approaches have been adopted by Chase *et al.* (2013) and Chase & Carrica (2013) for the analysis of the flow field and the performances of the DSub in self-propulsion, in captive steady turn and horizontal overshoot maneuvers.

Posa & Balaras (2016) performed LES for the flow over the fully appended DSub at 0 yaw angle and Reynolds number equal to $Re_L = 1.2 \times 10^6$ using a 2.8 billion nodes grid. The authors used a direct-forcing immersed boundary method (Posa & Balaras (2014)) solving the governing equations over a staggered grid in cylindrical coordinates. They adopted the Wall-Adapting Local Eddy-Viscosity (WALE) subgrid scale model of Nicoud & Ducros (1999), which it has to be proven to be as accurate as any dynamic model at a lower computational expense. Posa & Balaras (2016) carried out a comprehensive analysis of the flow. The mean velocity and Reynolds stress fields were calculated and validated against experimental and DNS data. Mean velocity and Reynolds stress profiles in the intermediate wake, at 6 submarine's diameters downstream, were compared with experimental data from Jiménez *et al.* (2010b). The authors also discussed the bimodal behavior of the wake and the evolution downstream towards self-similarity.

Kumar & Mahesh (2018) investigated the axisymmetric body of revolution, i.e. the submarine DSub without the appendages and propeller, using a body fitted unstructured grid, at Reynolds number $Re_L = 1.1 \times 10^6$ based on the length of the hull and the free-stream velocity. They used the dynamic Smagorinsky sub-grid scale stress model (Germano *et al.* (1991), Lilly (1992)). The algorithm ensured good conservation properties despite the unstructured mesh. A deep analysis of the turbulent boundary layer and of the wake till 15 diameters downstream was carried out. They both found a good agreement with the experimental data of Jiménez *et al.* (2010b) and Jiménez *et al.* (2010a), Jiménez *et al.* (2010b) respectively.

As discussed above, to make LES more affordable at high Reynolds number, WMLES approach can be used. Two main families can be identified: the hybrid RANS/LES models and the wall-stress models. In the present thesis we follow the second strategy. Review papers on the use of wall-layer models in conjunction with LES are given in Piomelli & Balaras (2002) and Larsson *et al.* (2016). It is well known that WMLES suffers from the log-layer mismatch (Larsson *et al.* (2016), Mukha (2018)) which causes a shifting (upward or downward) of the mean velocity profile, scaled using friction velocity u_τ. This is strongly related to the wall shear-stress value modeled by the wall function and influences the drag force, the separation point and the wake.

WMLES has been successfully applied to the analysis of the flow around a submarine model by (Anderson *et al.*, 2012; Fureby *et al.*, 2016); they investigated the BB1 model (which is a geometry similar to the BB2, the major difference is the absence of the forward planes), at 0 and 10 degrees yaw and at Reynolds number $Re_L = 4.5 \times 10^6$. In their work, numerical simulations using WMLES and RANS were validated against experimental data in low speed wind tunnel tests at $Re_L = 2.7 \times 10^6$. The focus of the work was on the sail wake and the fin-tip vortex displacement. The solution was obtained using the OpenFOAM toolkit and discretizing the equations on an unstructured grid composed of $340 \cdot 10^6$ cells and using wall-stress models as boundary conditions at the solid surfaces. The authors used the sub-grid scale Mixed Model (MM) and the Localized Dynamic Kinetic energy Model (LDKM). Friction coefficient along the hull was not shown or even mentioned. It has to be highlighted that in a following papers (Norrison *et al.*, 2016) and (Petterson *et al.*, 2018), WMLES was employed for the analysis of the self-propelled submarine advancing in straight ahead motion.

Large-eddy simulation data can be processed to characterize the hydro-acoustic field, although, to the best of our knowledge, this represents a novelty in literature.

To summarize, the present work focuses on WMLES of the BB2 submarine model at Reynolds number equal to $Re_L = 1.2 \times 10^6$, paying special attention to the axisymmetric wake development. The flow conditions are the same as in Jiménez *et al.* (2010b) and Posa & Balaras (2016). Modeling the near-wall flow allows for substantial reduction of the computational cells up to about $40 \cdot 10^6$, making the simulation more affordable. We apply the acoustic-analogy in the formulation 1D and characterize the hydro-acoustic signature of a fully appended BB2 submarine. To be noted that the the presence of propeller is not considered in the present study for a main reason. Since this is the first literature study where the acoustic signature of the BB2 submarine is investigated, it is more convenient to focus on the main body in order to obtain a full characterization. To be noted that the interaction with the propeller may vary the acoustic signature also in view of the characteristics of the propeller.

The thesis is organized as follows. Chapter 1 introduces the problem (in section 1.1), the tools related to fluid dynamic analysis (in section 1.4 and 1.4.10) and to hydroacoustics (in section 1.5). Section 1.2 reports the motivations for the study. Chapter 2 shows the results of RANS simulations at Reynolds number 9.57×10^6 and 1.2×10^6, and a comparison between the solution obtained with a wall-resolving grid and the solution obtained using wall-layer models. Chapter 3 describes the wall-modeled large-eddy simulation model and the results of simulations are reported. In Chapter 4 the noise signature of the BB2 is evaluated. Finally concluding remarks and suggestions for future research are reported in chapter 5.

1.2 Motivations

The motivations for this work are twofold. As explained in section 1.1, the acoustic signature of submarines is, among others, of great military interest. Applying the advective form of the FW-H equation to the BB2 submarine allows to provide a complete computational hydro-acoustics characterization, including also the contribution of the non-linear quadrupole terms on acoustic noise. In the past, the computation of non-linear term has been often omitted because considered unimportant with respect to the linear terms. Recent advancements in the field clarified their role in the correct evaluation of the turbulence induced noise. The study is carried out focusing on the submarine in its own basic configuration without propeller for two reasons: first to highlight the acoustic properties of the hull by itself; second because of more practical reasons, in fact to reduce the possibility to be detected by surface ships which make use of SONAR, submarines may advance in silence running, by shutting down nonessential source of noise and reducing the speed to minimize propeller noise. In this configuration, the wake is the main source of noise.

To the best of our knowledge, both the methodology and the application represent a novelty in literature.

The second motivation is to show that approximating the near-wall flow using the well-known wall-layer models yields an accurate hydrodynamic representation of the turbulent wake in the far field. Wall-modeling allows to move the limited available computational resources from the turbulent boundary layer (as in the case of WR-LES discussed in section 1.1) to the solution of the turbulent wake, making such simulation more affordable.

1.3 Short description about the BB2 submarine

The Joubert (Joubert, 2004, 2006) hull form was developed to provide a notional representation for a diesel electric submarine, with large casing, fin, and an X-form rudder arrangement. The most recent modification is known as model ”BB2” (previous hull form modification is known as ”BB1”). The design has an overall length of $L_{oa} = 70.2$ m. Hereafter we refer to L or L_{oa}. The model length here considered it is L=3.826 m. Table 1.1 reports additional geometrical characteristic lengths. The nose shape (derived from a NACA0018 forebody) was designed with the aim of maintaining natural laminar flow over the bow. It is axisymmetric for the first $0.070L$. The sail shape is that of a NACA0022 with a height of $0.080L$. On the sail there are two NACA0015 hydroplanes (Lee *et al.*, 2019).

Description	**Symbol**	**Magnitude**		**Unit**
Length overall submerged	L_{oa} or L	70.2	3.8260	m
Depth to deck	D	10.6	0.5777	m
Depth to top of sail	D_{sail}	16.2	0.8829	m

Table 1.1: Submarine geometry (model scale 1 : 18.348)

1.4 Fluid-Dynamics: mathematical background

In this section we provide the mathematical formulations together with the turbulence closure approaches employed in the present research work.

1.4.1 Governing equations

Present work deals with incompressible flow, namely the flow of water around a submarine. In absence of vertical variation of density, the fluid motion in incompressible flow conditions can be completely described by the continuity equation, which expresses the conservation of the mass, and the momentum equations. This set of equations constitute a non linear system of partially differential equations.

For isothermal incompressible fluids (ρ is constant) the conservation laws can be written in the following conservative form:

- **Continuity equation**

$$\frac{\partial U_i}{\partial x_i} = 0 \tag{1.1}$$

- **Momentum equation**

$$\frac{\partial U_i}{\partial t} + \frac{\partial}{\partial x_j}(U_i U_j) = -\frac{1}{\rho}\frac{\partial p}{\partial x_i} + \nu \frac{\partial^2 U_i}{\partial x_j \partial x_j} \tag{1.2}$$

where:

- i, j, k=1, 2, 3
- U_i is the velocity component along the x_i direction $[ms^{-1}]$. It is a three dimensional vector field depending on position $\mathbf{x}$ and time t
- ν is the kinematic viscosity $[m^2s^{-1}]$
- p is the kinematic pressure $[m^2s^{-2}]$ and is equal to $\frac{P}{\rho}$

In equation 1.2, constitutive relations for Newtonian fluids were applied and the gravity force term was omitted, since unimportant in the absence of both density variations and free-surface effects.

The previous set of equations has to be equipped with suitable initial and boundary conditions (usually we refer to Dirichlet, Neumann or Robin boundary conditions types (Salsa, 2008)).

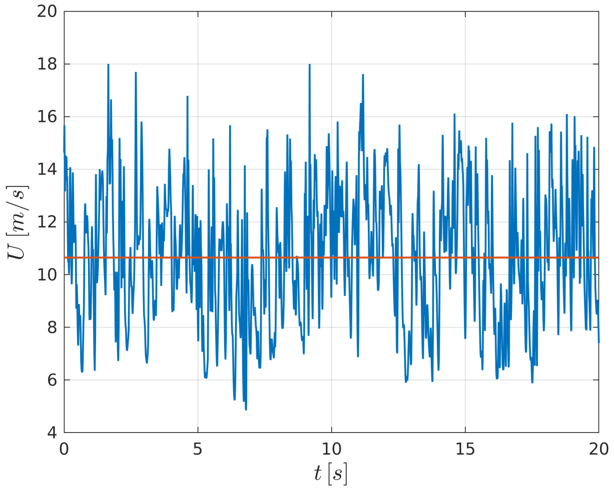

Figure 1.2: Time-signal of axial velocity $U(t)$ (—) at distance y/δ=0.0105 from the bottom wall of a doubly-periodic channel at Re_τ=180. Time-averaged signal $\langle U(t)\rangle$ (—)

1.4.2 Turbulence modeling

Most of the engineering fluid-dynamic problems are characterized by rather high Reynolds numbers and we define such flows as ”turbulent”. We may encounter turbulent flows in many applications and in many day-life actions. Despite that, we do not have unique definition of what Turbulence is. A recent definition of turbulence is a flow characterized by the presence of coherent structures (eddies) evolving randomly in space and time. The coherence is associated to a number of unstable vortex structures which, on average, tend to be destroyed generating smaller and smaller structures up to the scales where energy is dissipated. This process causes energy dissipation from one side and rapid mixing from the other side. Although chaotic in nature (meaning that a turbulent field cannot be reproduced in a deterministic way), turbulence can be considered an ergodic process and afforded using statistical analysis. For example, we consider velocity signal sampled in a canonical plane channel flow (the flow driven by a steady pressure gradient and developing between two parallel and infinite plates), as shown in figure 1.2.

Introduction

To characterize this random signal, under the assumption of ergodic process, we can calculate the mean value (—), its second, third and fourth order statistics, PDFs, two-point correlations, etc.

A turbulent flow has the ability to transport and mix fluid much more effectively then a comparable laminar one (Pope, 2000). Turbulent flows are always three-dimensional and time dependent, even when external conditions do not change. Turbulence is a multi-scale phenomena: it goes from the smallest turbulent eddies characterized by Kolmogorov micro-scales η, to the geometry dimensions scale. Moreover, also time scales vary intensely. These few considerations clearly show that to simulate a turbulent flow is a demanding and challenging task, and its complexity and computational cost increase exponentially with the flow Reynolds number ($Re = UL/\nu$ where U and L are a velocity and length scale of the flow and ν is the kinematic viscosity).

There are many possible ways to simulate a turbulent flows. The first, Direct Numerical Simulation (DNS) (Davidson, 2004) numerically integrates the governing equations 1.1 and 1.2 over the whole range of turbulent scales. The requirements on mesh resolution and time-step size put very high demands on the computer resources, making it unsuitable for engineering applications. The computational cost has been estimated to increase with Re^3 in free-shear flows and with $Re^{3.5}$ in wall bounded flows (see (Piomelli & Balaras, 2002) and literature therein reported). This makes unaffordable DNS at engineering values of Re.

On the opposite side of DNS, we find the Reynolds-Averaged Navier-Stokes equations (RANS). These equations, are derived from the original Navier-Stokes equations, after an operation of decomposition of the total field in an average part and a fluctuating one. RANS are the equations expressing conservation laws for the mean flow, and the effect of turbulence is quantified by the Reynolds stress tensor, which, indeed represents the contribution of turbulence to the mean field. Although the RANS approach is the tool most used in engineering, it suffers because of inaccuracy associated to the turbulence models. To be highlighted that the asymptotic behavior of a RANS solution, still remains a solution of the mean field, where the approximation error associated to the grid resolution have been eliminated, still containing the errors associated with the turbulence model employed. In between RANS and DNS we find Large-Eddy Simulations (LES). LES resolves the governing equations up to a filter length scale, modeling the unresolved part by means of a sub-filter scale model. The underlying idea of LES is that the large and energy carrying scales of turbulence, which depend on the peculiarities of the flow field, are resolved directly through an unsteady and 3D simulation, whereas the small and more isotropic scales are parametrized using a subgrid scale model. To be noted that the asymptotic behavior of a LES is a DNS. To derive the LES equations it is necessary to filter the Navier-Stokes equations, using a low-pass filter which removes the high wave-number eddies (the smallest one). LES is still a highly computationally expensive tool to be applied extensively in engineering applications, nevertheless its usage is fast growing also in industrial applications.

A special class of unsteady RANS is that developed by Menter & Egorov (2010) where the model is able to adapt to the scale which is resolving, furnishing a LES-type behavior, without giving any information about the grid size in the model.

An overview of the most common turbulence modeling approaches is shown schematically (for the sake of clearness, the computational cost does not increase linearly between different approaches) in figure 1.3, where the common acronyms are explained below:

- **RANS** Reynolds-Averaged Navier-Stokes equations
- **URANS** Unsteady RANS
- **PANS** Partially-Averaged Navier-Stokes equations (Girimaji & Suman, 2012)
- **SAS** Scale-Adapting Simulations (Menter & Egorov, 2010)
- **DES** Detached-Eddy Simulation (Spalart, 2009)
- **LES** Large-Eddy Simulation
- **DNS** Direct Navier-Stokes Simulation

Within the general classes of methodologies (DES, RANS, LES) there are a large number of different derivations, turbulence and sub-grid scale models. The reader interested in these topics can find detailed information about turbulence modeling in Davidson (2004), Pope (2000), Wilcox (1994).

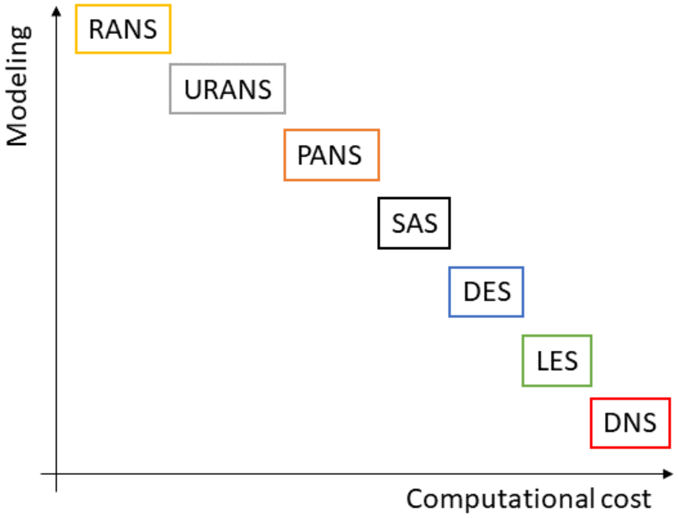

Figure 1.3: Most common approaches in numerical solution of turbulent flows

1.4.3 Averaging in computational fluid-dynamic

Reynolds first introduced the concept of averaging in modern fluid-dynamic in terms of math relations. In turbulence we can recognize three time of averages: time average, space average and ensemble average. Time averaging is most suitable for stationary turbulent flows; In that case, if we consider a field variable $F(\mathbf{x}, t)$, its time average $\langle F(\mathbf{x}) \rangle$ is given by

$$\langle F(\mathbf{x}) \rangle = \lim_{T \to \infty} \frac{1}{T} \int_{t}^{t+T} F(\mathbf{x}, t) dt \tag{1.3}$$

Space average is convenient when turbulence is homogeneous in one or more directions; In the case the flow is homogeneous in all directions we can write the averaged field $\langle F(\mathbf{x}) \rangle$ as

$$\langle F(\mathbf{x}) \rangle = \lim_{V \to \infty} \frac{1}{V} \iiint_{V} F(\mathbf{x}, t) dV \tag{1.4}$$

Ensemble average is the average of the same quantities for N repetitions of the same experiment. It is summation of $F_i(\mathbf{x}, t)$ over all experiments and we can write it as:

$$\langle F(\mathbf{x}) \rangle = \lim_{N \to \infty} \frac{1}{N} \sum_{i=1}^{N} F_i(\mathbf{x}, t) \tag{1.5}$$

The results of these operation is simply called *mean* and will not be specified which kind of averaged is performed to get this mean unless it is necessary to describe a particular procedure adopted.

For more details about averages and statistical tool in turbulence the reader is refereed to classic books as Pope (2000), Davidson (2004) and Wilcox (1994), or the paper of Kim *et al.* (1986).

1.4.4 Mean-flow equations

In the previous section, it was mentioned that to describe turbulence it is possible to use various statistical quantities as means, PDFs, etc. It is possible to derive equations for the evolution of all of these quantities, starting from Navier-Stokes equations. The most basic of these equations are those that govern the mean velocity field $\langle \mathbf{U}(\mathbf{x}, t) \rangle$.

The first step is to decompose the instantaneous quantity (*i.e.* velocity component) $\mathbf{U}(\mathbf{x}, t)$ onto the sum of its mean value $\langle \mathbf{U}(\mathbf{x}, t) \rangle$ and its fluctuation:

$$\mathbf{u}(\mathbf{x}, t) \equiv \mathbf{U}(\mathbf{x}, t) - \langle \mathbf{U}(\mathbf{x}, t) \rangle \tag{1.6}$$

Despite its apparent simplicity, equation 1.6 is one of the most important achievement in turbulence and fluid mechanics. It is the mathematical translation of what Leonardo da Vinci observed and sketched many years before. John L. Lumley (Cornell University) translated one of da Vinci's expressions as follows (Tennekes & Lumley, 1972): *"Observe the motion of the surface of the water, which resembles that of hair, which has two motions, of which one is caused by the weight of the hair, the other by the direction of the curls; thus the water has eddying motions, one part of which is due to the principal current, the other to the random and reverse motion."*

"So moving water strives to maintain the course pursuant to the power which occasions it and, if it finds an obstacle in its path, completes the span of the course it has commenced by a circular and revolving movement."

"... The small eddies are almost numberless, and large things are rotated only by large eddies and not by small ones, and small things are turned by both small eddies and large" .

Combining equation 1.6 and the continuity equation 1.1 follows that both $\langle \mathbf{U}(\mathbf{x}, t)\rangle$ and $\mathbf{u}(\mathbf{x}, t)$ are solenoidal. It means that

$$\nabla \cdot \langle \mathbf{U} \rangle = 0 \tag{1.7}$$

and then

$$\nabla \cdot \mathbf{u} = 0 \tag{1.8}$$

To take the equation 1.2 of momentum for the mean flow is not trivial because of the non linear convective term. To do that, it is necessary to start from the variation of momentum within a control volume. Under the assumption of incompressible flows:

$$\frac{\partial U_j}{\partial t} + \frac{\partial (U_j U_i)}{\partial x_i} \tag{1.9}$$

and perform the average

$$\frac{\partial \langle U_j \rangle}{\partial t} + \frac{\partial \langle U_j U_i \rangle}{\partial x_i}. \tag{1.10}$$

Applying the Reynolds decomposition to the non-linear term we obtain

$$\langle U_j U_i \rangle = \langle U_j \rangle \langle U_i \rangle + \langle u_j u_i \rangle \tag{1.11}$$

The tensor $\langle u_j u_i \rangle$ is known as **Reynolds-stress tensor**, and we denote it as τ_{ij}. Moving from the Eulerian to the Lagrangian framework, we can obtain the *mean substantial derivative* which, given a property $\phi(\mathbf{x}, t)$, represents its rate of change following a point moving with the local mean velocity:

$$\left\langle \frac{DU_j}{Dt} \right\rangle = \frac{\partial \langle U_j \rangle}{\partial t} + \langle U_i \rangle \frac{\partial \langle U_j \rangle}{\partial x_i} + \frac{\partial}{\partial x_i} \langle u_j u_i \rangle \tag{1.12}$$

The time-averaged LHS of equation 1.2 is simply equal to

$$= -\frac{\partial \langle p \rangle}{\partial x_i} + \frac{\partial}{\partial x_j}(2\nu \bar{S}_{ij}) \tag{1.13}$$

where

$\mathbf{\bar{S}_{ij}}$ is the mean rate of strain tensor

$\langle p \rangle$ is a mean kinematic pressure

Writing down and manipulating the last two equations we get the **Reynolds-averaged Navier-Stokes equation (RANS)**

$$\frac{\partial \langle U_j \rangle}{\partial t} + \langle U_i \rangle \frac{\partial \langle U_j \rangle}{\partial x_i} = -\frac{\partial \langle p \rangle}{\partial x_i} + \frac{\partial}{\partial x_j}(2\nu \bar{S}_{ij} - \langle u_j u_i \rangle) \tag{1.14}$$

To be noted that the time derivative of mean velocity means that the problem is not steady in a statistical sense, and the average is taken over a turbulent time scale which is much smaller than the time scale of inertial unsteadiness in the flow.

1.4.5 The closure problem

In previous section 1.4.4 we derived the Reynolds Averaged Navier-Stokes equations taking the time average of the momentum and continuity equations. In these equations the unknown are the mean velocity field and the mean pressure. Solve the mean flow is far computationally cheaper compared with any scale-resolving simulation. For industry purpose analysis mean flow could be sufficient for most of the cases. Unfortunately, mean-flow equations are not in a close-form: the Reynolds stress tensor is symmetric and accounts for six additional unknown terms. After the averaging process, the equations available are still four, the continuity and the three components of momentum equations, and the system is not closed yet. To close this system we must find the exact number of equations to solve for our unknowns. This is known in literature as the 'closure problem', denoting the fact that equations written at the order 'n' introduce new variables at the order 'n+1'. As an example, the mean flow equations (1st-order) introduce unknown at the 2nd-order, the Reynolds stresses.

The Reynolds stresses need a parametrization so that over the latter 40 years a large amount of models have been developed and used in a wide class of flow fields. Turbulence modeling has to provide the necessary physical information to derive approximations of the unknowns in terms of the known quantities and close the system.

Practical terminology refers to algebraic (zero-equations models), one-equations models, two-equations models and Stress transport models. We define n-equation model a model that requires the solution of n additional differential transport equations in addition to conservation of mass, momentum and energy. Hereafter we briefly mention some of them.

1.4.6 Eddy-viscosity hypothesis

Eddy-viscosity hypothesis prescribes Reynolds stresses as a function of turbulent-viscosity mean velocity gradients, it is:

$$\langle u_i u_j \rangle = \frac{2}{3} k \delta_{ij} - \nu_t \left(\frac{\partial \langle U_i \rangle}{\partial x_j} + \frac{\partial \langle U_j \rangle}{\partial x_i} \right) \tag{1.15}$$

Where ν_t is the eddy-viscosity, k is the turbulent kinetic energy and δ_{ij} is the Kronecker's delta.

The tensor a_{ij}, defined as $a_{ij} \equiv \langle u_i u_j \rangle - \frac{2}{3} k \delta_{ij}$, corresponds to the anisotropic part of Reynolds stress tensor and it is in charge of transport momentum. We could now express Reynolds stress anisotropy through the mean rate of strain tensor and obtain a more familiar expression:

$$a_{ij} = -2 \nu_t \bar{S}_{ij} \tag{1.16}$$

After this hypothesis the Reynolds averaged Navier-Stokes equations apparently become totally similar to Navier-Stokes equations:

$$\frac{\partial \langle U_i \rangle}{\partial t} + \langle U_i \rangle \frac{\partial}{\partial x_j} \langle U_i \rangle = -\frac{1}{\rho} \frac{\partial p^\star}{\partial x_i} + \nu_{eff} \frac{\partial^2 \langle U_i \rangle}{\partial x_j \partial x_j} \tag{1.17}$$

where $\nu_{eff} = \nu + \nu_t$ and $p^\star$ is a modified pressure $p^\star = \langle p \rangle + \frac{2}{3} k \delta_{ij}$ (for simplicity we will refer to $p^\star$ as p)

This hypothesis is particularly poor from a mathematical point of view and it is correct just in few cases. Nevertheless it remains still the most convenient closure to the averaged Navier-Stokes equations. We actually move our unknown from a tensor, $\langle u_i u_j \rangle$ to a scalar function of time and space, ν_t constraining the principal axes of the Reynolds stresses to those of the mean rate-of-strain tensor.

1.4.7 Two equation turbulence models

A short description of the turbulent models utilized in this thesis follows. The reader interested in the particular topic is addressed to the classical book of Wilcox (1994).

$k-\varepsilon$ family turbulence model

Two-equation $k-\varepsilon$ models are widely used. In history of turbulence modeling they were developed just after simpler algebraic turbulence length-scale model, giving the mathematical formulation deeper insight about the physics of turbulence. Over the years, several different versions were developed, trying to overcome the limitations of the previous formulations or to be more general. Despite the strength applied in this field, still we do not have a universal model, and is a task of the CFD-user to choose the right one. We might additionally say that CFD is nowadays a large community, and this kind of information are largely available.

Standard $k-\varepsilon$ The standard $k-\varepsilon$ (Launder & Spalding, 1974) two-equations RANS model solves two transport equation for turbulence quantities k and ε. From dimensional point of view we can form a quantity of the dimensions of ν_t by simply combing k^2/ε. And so we can derive ν_T from k and ε. The constant, $C_\mu = 0.09$, fit ν_t to appropriate values (it actually can be derived from turbulent channel flow DNS data freely available for download, as done in Pope (2000).

The model equation for turbulent kinetic energy k is:

$$\frac{\partial k}{\partial t} + \frac{\partial k \langle U_i \rangle}{\partial x_i} = \frac{\partial}{\partial x_j}\left[\frac{\nu_T}{\sigma_k}\frac{\partial k}{\partial x_j}\right] + \mathcal{P} - \varepsilon \tag{1.18}$$

The LHS of the equation takes into account the rate of change of k plus its convective transport and sets it equal to diffusion of turbulent kinetic energy plus its rate of production minus turbulence kinetic energy destroyed by unity of time. The same rationale can be applied to ε, which is:

$$\frac{\partial \varepsilon}{\partial t} + \frac{\partial \varepsilon \langle U_i \rangle}{\partial x_i} = \frac{\partial}{\partial x_j}\left[\frac{\nu_T}{\sigma_\varepsilon}\frac{\partial \varepsilon}{\partial x_j}\right] + C_{1\varepsilon}\frac{\varepsilon}{k}\mathcal{P} - C_{2\varepsilon}\frac{\varepsilon^2}{k} \tag{1.19}$$

$\mathcal{P}$ - is the rate of production of turbulent kinetic energy

$$\nu_t \equiv C_\mu \tfrac{k^2}{\varepsilon}$$

In the equations are also present four additional constants, namely: σ_k, σ_ε, $C_{1\varepsilon}$, $C_{2\varepsilon}$. Their value is set by using data fitting from experiments of many turbulent flows, they are: $\sigma_k = 1.00$, $\sigma_\varepsilon = 1.30$, $C_{1\varepsilon} = 1.44$, $C_{2\varepsilon} = 1.92$.

$k - \omega$ SST

The Russian scientist A. Kolmogorov, lately in 1942, introduced a new quantity ω to describe the rate of dissipation of energy for unit volume and time that, together with the model equation for k allows to close the system of equation under the Boussinesq eddy-viscosity approximation (1877). Kolmogorov's $k - \omega$ model has been developed and improved for decades becoming, in its latter version which is called Shear Stress Transport (SST), one of the most used turbulence model in RANS simulations environment. SST model was introduce by Menter in 1994 and it combines the k-ω turbulence model and k-ε turbulence model in a way that the first is used to solve boundary layer switching then to k-ε in the free shear flow.

Transport equations of turbulence kinetic energy and specific dissipation rate are shown below.

$$\frac{\partial(\rho\, k)}{\partial t} + \frac{\partial(\rho\,\langle U_j\rangle\, k)}{\partial x_j} = P - \beta^*\,\rho\,\omega\,k + \frac{\partial}{\partial x_j}\left[(\mu + \sigma_k\mu_t)\,\frac{\partial k}{\partial x_j}\right]$$
$$\frac{\partial(\rho\,\omega)}{\partial t} + \frac{\partial(\rho\,\langle U_j\rangle\,\omega)}{\partial x_j} = \frac{\gamma}{\nu_t}P - \beta\,\rho\,\omega^2 + \frac{\partial}{\partial x_j}\left[(\mu + \sigma_\omega\mu_t)\,\frac{\partial \omega}{\partial x_j}\right] + 2(1-F_1)\frac{\rho\sigma_{\omega 2}}{\omega}\frac{\partial k}{\partial x_j}\frac{\partial \omega}{\partial x_j}$$

Where,

$$P = \tau_{ij}\frac{\partial\langle U_i\rangle}{\partial x_j}$$

$$\tau_{ij} = \mu_t\left(2S_{ij} - \tfrac{2}{3}\tfrac{\partial\langle U_k\rangle}{\partial x_k}\delta_{ij}\right) - \tfrac{2}{3}\rho k\delta_{ij}$$

$$S_{ij} = \tfrac{1}{2}\left(\tfrac{\partial\langle U_i\rangle}{\partial x_j} + \tfrac{\partial\langle U_j\rangle}{\partial x_i}\right)$$

$$\mu_t = \frac{\rho a_1 k}{\max(a_1\omega, \Omega F_2)}$$

Introduction

$$\phi = F_1\phi_1 + (1 - F_1)\phi_2$$

$$F_1 = \tanh\left({\arg_1}^4\right)$$

$$\arg_1 = \min\left[\max\left(\frac{\sqrt{k}}{\beta^*\omega d}, \frac{500\nu}{d^2\omega}\right), \frac{4\rho\sigma_{\omega 2}k}{\mathrm{CD}_{k\omega}d^2}\right]$$

$$\mathrm{CD}_{k\omega} = \max\left(2\rho\sigma_{\omega 2}\frac{1}{\omega}\frac{\partial k}{\partial x_j}\frac{\partial \omega}{\partial x_j}, 10^{-20}\right)$$

$$F_2 = \tanh\left(\arg_2^2\right)$$

$$\arg_2 = \max\left(2\frac{\sqrt{k}}{\beta^*\omega d}, \frac{500\nu}{d^2\omega}\right)$$

Introduction

Andrey N. Kolmogorv it is considered a great scientist for his contributes to pure math and turbulence (Davidson *et al.*, 2011). During my master's degree study at the university I was simply amazed by his work about scales of turbulence. For this reason, when I had the possibility, I did not lost the chance to "meet" him. Hereby a picture I took personally:

Figure 1.4: A. N. Kolmogorov's memorial in Novodevichy cemetery, Moscow

To summarize, RANS constitute an invaluable tool for prediction of turbulent flow. They validity and accuracy is mostly associated to the characteristics of the turbulence model. Very complex flow fields, like those characterized by massive separation substantial three-dimensionality, rotation, stratification etc. can hardly be represented by eddy-viscosity type models, or by even more complex 2nd-order models. This mainly because the fact a turbulence model in the RANS framework has to represent the entire turbulent spectrum even in presence of very complex physical processes. To overcome these issues, eddy-resolving methodologies have been developed; among the others, LES is one of the most popular.

1.4.8 Filtered Navier-Stokes equations

In LES the large three-dimensional unsteady turbulent motions are directly represented, modeling the effect of the smaller and more isotropic scales of motion on the larger and more energetic ones. As stated in Pope (2000), there are four conceptual steps in LES:

1. To decompose the velocity $\mathbf{U}(\mathbf{x}, t)$ into a sum of a filtered (resolved) component $\overline{\mathbf{U}}(\mathbf{x}, t)$ and a residual or subfilter-scale (SFS) or subgrid-scale (SGS), component $\mathbf{u}(\mathbf{x}, t)$, a filtering operation has to be defined.
2. The equations for the evolution of the filtered velocity field are derived from the Navier-Stokes equations. The momentum equation containing the *residual stress tensor* (SFS stress tensor) that arises from the residual motions.
3. Closure is obtained by modeling the SFS stress tensor, most simply by an eddy-viscosity model, that conceptually is the same done for RANS closure.
4. The model filtered equations are solved numerically for $\overline{\mathbf{U}}(\mathbf{x}, t)$, which provides an approximation to the large-scale motions in one realization of the turbulent flow.

The filtering operation is usually said "implicit" when the grid resolution and the discretization error attenuate the high wave numbers and no filter is directly applied to the resolved quantities. Otherwise the resolved quantities are directly filtered out, as happens using an explicit filter, see Bose *et al.* (2010). In particular, referring to the momentum equation for incompressible flows, which reads as

$$\frac{\partial U_i}{\partial t} + \frac{\partial}{\partial x_j}(U_i U_j) = -\frac{1}{\rho}\frac{\partial p}{\partial x_i} + \nu \nabla^2 U_i \tag{1.20}$$

we know that we have to solve it down up to the Kolmogorov scales, for both time and space; it is the approach of DNS. Solving on a grid coarser than the Kolmogorov length scale η, and advancing in time using a time-step larger than τ_η, the characteristic time of the smaller scales, the relation 1.20 turns to be unbalanced. In this case the simulated physics is not the one predicted from the momentum equation. This can be solved modeling extra terms able to account the effect of the not resolved scales. From a mathematical point of view, the only way to get till this point coherently is applying a generic low-pass filter, G, operation to the Navier-Stokes equations (Bose *et al.*, 2010), otherwise each term in the LES equation would be subject to a different one-dimensional (1D) filter, making the actual equation to be solved, not rigorously derivable from the Navier-Stokes equations.

Filtering and differentiation commute, so that we obtain:

$$\frac{\partial \bar{U}_i}{\partial t} + \frac{\partial}{\partial x_j}(\overline{U_i U_j}) = -\frac{1}{\rho}\frac{\partial \bar{p}}{\partial x_i} + \nu \nabla^2 \bar{U}_i \tag{1.21}$$

where $\bar{\mathbf{U}}$ is soleinodal. This can be rewritten in a more familiar form

$$\bar{U}_i(x_i, t) = \int_{\Omega} G(x_i, x_i', \Delta) U_i(x_i', t) dx_i', \tag{1.22}$$

$$\frac{\partial \bar{U}_i}{\partial t} + \frac{\partial}{\partial x_j}(\bar{U}_i \bar{U}_j) = -\frac{1}{\rho}\frac{\partial \bar{p}}{\partial x_i} + \frac{1}{\rho}\frac{\partial \tau_{ij}^R}{\partial x_i} + \nu \nabla^2 \bar{U}_i, \tag{1.23}$$

$$\tau_{ij}^R = \rho(\bar{U}_i \bar{U}_j - \overline{U_i U_j}), \tag{1.24}$$

$$\frac{\partial \bar{U}_i}{\partial x_i} = 0 \tag{1.25}$$

which looks similar to Reynolds-averaged momentum equation 1.17, which in turns was similar to the classic momentum equation 1.2. The same apparent structure with very different physical meanings.

Thus filtering leads to the introduction of fictitious stresses, called *residual stresses*, which are apparently analogous to Reynolds stress introduced when time-averaging the Navier-Stokes equations (RANS). The residual stresses are the contribution of the resolved scales to the resolved instantaneous motion. The filter resolution (we understood already which is closely related to the local grid spacing) should lie in the inertial subrange. The unknown residual stresses have to be modeled. The most popular method to account for the unresolved scales is to use an eddy-viscosity model which is based on the eddy-viscosity hypothesis to relate the resolved stress to the rate of strain tensor, in analogy with the molecular viscous stress in laminar flows. In this case we write the residual stresses as

$$\tau_{ij}^R = 2\rho\nu_R \overline{S}_{ij} + \frac{1}{3}\delta_{ij}\tau_{kk}^R = 2\rho\nu_r \overline{S}_{ij} + \frac{2}{3}k_r \delta_{ij} \tag{1.26}$$

where ν_r (sometimes ν_{sgs} or ν_T) is the eddy viscosity of the residual motion and k_r (sometimes k_{sgs}) is the residual kinetic energy. This yields

$$\frac{\partial \bar{U}_i}{\partial t} + \frac{\partial}{\partial x_j}(\bar{U}_i \bar{U}_j) = -\frac{1}{\rho}\frac{\partial \bar{p}^\star}{\partial x_i} + 2\frac{\partial}{\partial x_i}\Big[(\nu + \nu_r)\overline{S}_{ij}\Big], \tag{1.27}$$

where $\bar{p}^\star$ is a modified pressure (we will refer to $p^\star$ simply as p) and $\overline{S}_{ij}$ is the filtered rate of strain tensor, which can be written as

$$\overline{S}_{ij} \equiv \frac{1}{2}\left(\frac{\partial \overline{U}_i}{\partial x_j} + \frac{\partial \overline{U}_i}{\partial x_j}\right). \tag{1.28}$$

From this follow the definition of the characteristic rate of strain

$$\overline{S} \equiv (2\overline{S}_{ij}\overline{S}_{ij})^{1/2} \tag{1.29}$$

The last step is to prescribe ν_r. Physical arguments suggest that ν_r should be determined by the most energetic of the unresolved eddies (Davidson, 2004), it means eddies of a scale a little smaller than $\Delta{=}L$. Using dimensional arguments $\nu_r \sim L(v^2{}_L)^{1/2}$, where $(v^2{}_L)^{1/2}$ is the kinetic energy of eddies of size L. In the *Smagorinsky model*, which was developed in the meteorological community in the sixties, $v^2{}_L$ is taken to be of the order of $L^2(\overline{S}_{ij}\overline{S}_{ij})$. Thus ν_r is

$$\nu_r = C_S^2 L^2 (2\overline{S}_{ij}\overline{S}_{ij})^{1/2}. \tag{1.30}$$

The dimensionless constant C_s, which is usually set to a value of ~ 0.1, is called Smagorinsky coefficient. This model, which has been popular for some time, seems to work fine for isotropic turbulence and free shear flows, being too dissipative near walls. This because the eddy viscosity has an nonphysical behavior when approaching the wall. This drawback was eliminated relaxing the eddy viscosity to zero in the wall region, according to an exponential decay (the van Driest function, see (Pope, 2000). We tested it together with the one-equation eddy viscosity SGS model, often called "k-equation" them solving the canonical turbulent channel flow, in appendix. **Note**: Equations 1.23 and 1.17 looks similar. We know that they has been derived in a completely different way. We take memory on the processes of derivation of the equations using $\bar{\bullet}$ or $\langle\bullet\rangle$ symbols. So a question arises spontaneously: if they look similar why do they behave completely differently? Menter & Egorov (2010) answered this question by developing the ”K Square-root-K L” model (KSKL), which is actually able to resolve the scales of turbulence. They claimed that classical URANS behavior of current turbulence models is not a result of the averaging procedure applied to the equations, as widely thought in the community, but of the specific way RANS models were formulated in the past.

1.4.9 Sub-grid scale models

Smagorinsky SGS model

The Smagorinsky subgrid scale (SGS) model is based on the eddy viscosity assumption, which postulates a linear relationship between the SGS shear stress and the resolved rate of strain tensor. Starting from equations 1.25 and 1.26, moved the unknown from τ_{ij}^R to ν_r. In OpenFOAM ν_r is calculated as

$$\nu_r = C_k \Delta \sqrt{k_r}$$

where C_k is a model constant whose default value is 0.094 and Δ is the grid size that define the subgrid length scale, which can be calculated with different methods (in this case we used cubeRootVol). The SGS kinetic energy k_r is computed with the assumption of the balance between the subgrid scale energy production and dissipation (**local equilibrium**), solving for k_r the following equation

$$\overline{S}_{ij} : \tau_{ij}^R + C_e \frac{k_r^{1.5}}{\Delta} = 0$$

where the operator : is a double inner product of two second-rank tensors that can be evaluated as the sum of the nine products of the tensor components.

The wall-adapting local eddy-viscosity sub-filter scale model

The wall-adapting local eddy-viscosity, shortly WALE, was developed by Nicoud & Ducros (1999). This model has many advantages and for this reason is becoming popular in the LES community.

The authors suggested to account for both strain rate and rotational rate. The derivation of the model starts looking at a common structure of many SFS model:

$$\nu_T = C_m \Delta^2 \widetilde{OP}(\vec{x}, t), \tag{1.31}$$

where $\widetilde{OP}$ it is an operator defined from the resolved scales.

It is clear the definition of the operator is of fundamental importance in modeling the subgrid scales. In this case it was proposed with the following characteristics:

- Galilean invariant
- to be easily adapting to any computational grid
- function of both strain rate and rotation rate
- goes to zero at the wall, so the use of work around as Van Driest dumping function is not required.

For analogy with other model, the velocity gradient tensor is a building block of this operator. In particular, considering the traceless symmetric part of the square of the velocity gradient tensor

$$S^d_{ij} = \frac{1}{2}(\tilde{g}^2_{ij} + \tilde{g}^2_{ji}) - \frac{1}{3}\delta_{ij}\tilde{g}^2_{kk} \tag{1.32}$$

$$\tilde{g}^2_{ij} = \tilde{g}_{ik}\,\tilde{g}_{kj} \tag{1.33}$$

After some math

$$\nu_T = \Big(C_w \Delta\Big)^2 \frac{\Big(S^d_{ij} S^d_{ij}\Big)^{3/2}}{\Big(\widetilde{S}_{ij}\,\widetilde{S}_{ij}\Big)^{5/2} + \Big(S^d_{ij}\,S^d_{ij}\Big)^{5/4}} \tag{1.34}$$

The WALE model formulation accounts for rotational rate, naturally goes to 0 with the expected slope at the wall, without the need for any ad hoc methods and it is computationally cheap.

1.4.10 Two different approaches: wall-resolving and wall-modeling

For wall-bounded flows, the near-wall region is characterized by high gradients that must be numerically resolved requiring the grid to be designed properly. In 3D-flows this might results in an high computational cost. It follows that when approaching a CFD analysis, a decision has to be taken before starting working on the grid topology (let's focus on body-fitted grid simulations), namely how to treat the near-wall region. In RANS's word, conceptually, there are two ways:

- To solve the RANS equations up to the inferior limit of the viscous sub-layer.
- To use a mathematical model, called wall-function, and solve the RANS equation up to a certain distance from the solid boundary, where the mathematical model is true.

The advantage of resolving the wall-layer is to get a more accurate solution. As already said, this is paid in terms of an higher computational cost, and the more the Reynolds number increases the more the wall-layer needs to be refined. Another drawback is that refining the cells towards the solid wall determines an increasing of the cell aspect-ratio and this might cause numerical instabilities.

At this stage, it clearly appears the advantage of avoiding to solve the viscous sublayer, especially for very high Re numbers.

To that scope *the law of the wall* is applied in the near-wall region. It states that statistically, the velocity of a turbulent flow at a certain distance from a solid boundary, is proportional to the logarithm of the distance from that point to the solid boundary. This is a *self-similar* solution for the mean velocity parallel to the boundary, and its application allows to determine with good approximation the velocity and the wall-shear stress. The limitation of this formulation are that it is valid only for very high Reynolds flows (say $Re > 10^5 \div 10^6$) and the flow has to be attached where the law is applied (Wilcox, 1994).

In general the ideal flow conditions should be as close as possible to a those that allow the developing of a turbulent boundary layer on a flat surface. In practice, wall-functions are widely applied especially in industrial applications.

In LES word, from operative point of view, the strategy is similar. So what one does is to create a grid with big cells close to the wall and apply as boundary condition to some flow quantity the log-low. However, conceptually the difference with RANS is huge. In RANS we are solving the time averaged Navier-Stokes equation and applying a statistical law makes not problems. In LES we are solving the filtered Navier-Stokes equation and we should take care that, in the point where we are applying the log-low, these statistical behavior holds. The flow dynamics in the near-wall determined by the dynamic of the eddies. In a statistical way their behavior is that predicted from the law of the wall, but this might be not true if we analyze their dynamic taking few snapshots at different times. What we could see it is large quantities of eddies going through their own life, so they are created, develop and break down. Said that, if the grid cells are large enough to contain ”many” of these eddies, or better a sample large enough, the inner layer can be assumed to be governed by the Reynolds-averaged Navier-Stokes equations, rather than the filtered Navier-Stokes equations solved in LES in the outer layer, and statistical arguments hold. Another way to explain that comes from thermodynamics. At the micro-nanoscale particles, such as atoms, molecules, and electrons, constituent in the body whose temperature is to be measured are in motion. They represent our eddies. We could measure their velocity and kinetic energy. At the macroscopic scale we are not interested in the single particle but at the whole average behavior, which can be represented by the temperature function or, in our case by the wall-function. A more comprehensive review of this topic can be found in Piomelli & Balaras (2002); Larsson *et al.* (2016). Further specific details regarding the application of the law of the wall to the present case will be given in sections 2.2.9 and 2.3.8.

1.5 Hydroacoustics: mathematical background

In this section we will go into a quick review of computational hydroacoustics (CHA), as it is relatively unexplored field. In particular, we briefly recall the governing equations of CHA and the computational techniques over which our radiated noise estimation is based.

1.5.1 Hydroacoustic noise in the oceans

Noise at sea is the result of the ambient noise and the noise generated by ships, whose the propellers and engines contribute mostly. There are many reasons why we should investigate hydro-acoustic noise level. Among them, the environmental acoustic noise level should be kept below a reasonable level for protection of the animal species living in the oceans. Sailors and passengers of ships should also travel with a comfortable feeling (Ianniello *et al.*, 2013; Ianniello, 2016). Moreover, military ships need to advance in silent running in order to hide themselves from sonars. Marine propellers are among the most important noise generators. They operate at very low Mach numbers and create a persistent turbulent wake (which sums to the wake generated by the ship's hull), which is not avoidable effect, and cavitation bubbles. The wake is a quadrupole noise source and propagates downstream in the far field. Cavitation bubbles act on the near field and excite only short bands of the spectra (Ianniello, 2016). Both constitute noise sources and are design-dependent; for these reasons, and for the limited availability computational resources, we preferred to focus this work on the acoustic noise of the wake generated by the BB2 geometry.

The hydroacoustic noise is usually characterized in laboratory tests or numerically. Both these two approaches usually give a simplified description of the hydroacoustic signature. Experiments are generally carried out inside a closed ambient and the reflection of the acoustic waves upon the solid surfaces influences measurement of the far field noise (Fischer *et al.*, 2017). Additionally, the physical conditions of the water and the operative conditions can not be completely reproduced (just think about stratification, salinity, temperature gradient). On the other hand, computational simulations of noise in principle do not suffer of such issues. For example, stratification and temperature gradient might be properly taken into account. Conversely, these kind of simulations are still limited almost to the academic field because of the fluid-dynamic solution, being extremely complicated and expensive.

In the next sections the basic equations of computational hydroacoustics will be presented. In the derivation of the the mathematical formulation, the focus is given on the particular practical application of submarine in a moving medium.

1.5.2 Towards Ffowcs Williams and Hawkings equation

The direct computation of the acoustic sound requires the solution of the three-dimensional, compressible, unsteady Navier-Stokes equations. This approach would require facing with several issues. For example, in a direct acoustic simulation, the computational domain should be wide enough (and well resolved) to extend the acoustic analysis in the far field avoiding spurious reflections form the non-physical boundaries. If the fluid considered is water, density is constant, and the use of a compressible solver is not appropriate. The time-step for a direct acoustic analysis would be much smaller than the one required by the fluid-dynamic counterpart, especially if the fluid considered is water. Fortunately, it can be assumed that the radiating sound has no influence on the flow itself and this allows to uncouple the fluid dynamic solution from the acoustic one. This kind of technique is usually referred as *acoustic analogy* and is considered as ”hybrid” methodology. This means that, the solution of the flow equations can be addressed choosing the most appropriate fluid dynamic solver, i.e. compressible or incompressible, depending on the characteristics of the flow. The resulting solution will be treated as a *source* of noise and radiated in the domain by an inhomogeneous wave equation.

Lighthill (1952) proposed a way to calculate the turbulence induced sound by considering turbulence as a distribution of noise sources in a medium at rest, and radiating it in the far field using mass and momentum conservation laws, re-written as an inhomogeneous wave equation. In this formulation, the presence of solid bodies is not considered. This approach allows avoiding the solution of the compressible Navier-Stokes equations and to treat the numerical acoustic problem as a post-process of the known fluid dynamic field.

Lighthill’s work started from the flow equations, where the momentum equation has been written in a more convenient form:

$$\frac{\partial \rho}{\partial t} + \frac{\partial\,(\rho\,U_i)}{\partial x_i} = 0 \tag{1.35}$$

$$\frac{\partial(\rho\,U_i)}{\partial t} + \frac{\partial}{\partial x_j}(\rho\,U_i U_j + p\,\delta_{ij}) = 0 \tag{1.36}$$

Taking the time derivative of mass conservation equation and eliminating the term $(\rho\,U_i)$ yields to:

$$\frac{\partial^2\rho}{\partial\,t^2} = \frac{\partial^2}{\partial x_i \partial x_j}(\rho U_i U_j + p\delta_{ij}) \tag{1.37}$$

which can be written in the form of inhomogeneous wave equation:

$$\frac{\partial^2\rho}{\partial\,t^2} - c_0^2 \nabla^2 \rho = \frac{\partial^2}{\partial x_i \partial x_j}(T_{ij}), \tag{1.38}$$

where $T_{ij} = \rho U_i U_j + p\delta_{ij} - c_0 \rho \delta_{ij}$ is the Lighthill's tensor.

Equation 1.38 can be rewritten in compact form using the d'Alembertian operator, denoted by $\Box^2$:

$$c_0^2 \Box^2 \rho = \frac{\partial^2}{\partial x_i \partial x_j}(T_{ij}),$$

As a measure of the acoustic noise amplitude, it is convenient to replace the dependent variable ρ with $\tilde{\rho} = \rho - \rho_0$, which indicates the density perturbation with respect to an initial state. Same reasoning applies to the pressure, thus substituting $p\,\delta_{ij}$ with $\tilde{p}\,\delta_{ij} = (p - p_0)\,\delta_{ij}$.

Finally we obtain:

$$c_0^2 \Box^2 \tilde{\rho}(\mathbf{x}, t) = \frac{\partial^2}{\partial x_i \partial x_j}(T_{ij}), \tag{1.39}$$

This equation describes acoustic pressure propagation in a medium at rest where the only source considered is the quadruple noise T_{ij}, which accounts for all the non-linear sources, as turbulence, shocks or cavitation.

The most natural evolution of Lighthill's work has been developed by Curle (1955) in the work "*The influence of solid boundaries upon aerodynamic sound*", where the presence of a solid reflecting bodies has been considered for the first time in literature. Ffowcs-Williams & Hawkings (1969) (FWH) extended and generalized the work of Curle, deriving an equation able to predict the sound generated by a rigid body moving in a fluid medium.

The body is described by a surface $f(\mathbf{x}, t) = 0$, with outward normal vector given by $\hat{\mathbf{n}}$.

1.5.3 FW-H equation

To derive the FWH equation in differential form, it is needed to proceed similarly to Lighthill (1952), including the terms relative to the fluid-body interaction in the mass and momentum equations. This is shown in equation 1.40:

$$\Box^2 p'(\mathbf{x}, t) = \tfrac{\partial}{\partial t}\Big(\rho_0 v_n \delta(f)\Big) - \tfrac{\partial}{\partial x_i}\Big(\tilde{p}\hat{n}_j \delta(f)\Big) + \tfrac{\partial^2}{\partial x_i \partial x_j}\Big[\Big(\rho u_i u_j + (\tilde{p} - c_0^2)\delta_{ij}\Big) H(f)\Big] \tag{1.40}$$

This result is based on the assumption that the contribution to the noise of the viscous effects is small compared to the contribution of the pressure, of massive separations and turbulence. This implies that only pressure field determines the interaction between the body and the flow. In LHS equation 1.40, pressure is the argument of $\Box^2$ operator (instead of the density). p' represents the acoustic pressure. If we assume the flow to be isentropic then $p' = c_0^2\tilde{\rho}$. The mechanisms of propagation of the acoustic pressure appear on RHS of equation 1.40. The first term is called *thickness* and accounts for the displacement of fluid given by the motion of the body. v_n is the body velocity projected in direction normal to the body surface $f(\mathbf{x}, t) = 0$. $\delta(f)$ is the Dirac function, it is 1 at the body and 0 elsewhere. The second term is known as *loading*; it represents the sound generated by the pressure forces on the rigid body surface. The last term is called *quadrupole*. We already met it in Lighthill (1952) analysis. At this stage it is multiplied by the Heaviside function, to force it to be null at the body surface.

1.5.4 Formulations 1 and 1A

Equation 1.40 can be turned into integral form using free-space Green function (Farassat, 1975). The Green function of the wave equation in the unbounded three dimensional space is given by:

$$G(\mathbf{x}, t; \mathbf{y}, \tau) = \begin{cases} 0 & \tau > t \\ \delta(\tau - t + r/c_0)/(4\pi r) & \tau \leq t \end{cases} \tag{1.41}$$

The two couples $(\mathbf{x}, t)$ and $(\mathbf{y}, \tau)$ describe the position in time of the observer and the source. The distance observer-source is indicated by $r = |\mathbf{x} - \mathbf{y}|$. Usually $g = \tau - t + r/c_0$.

As explained in Farassat (2007), the surface $g = (\tau - t + r/c_0)/(4\pi r) = 0$ can be visualized as a contracting sphere. It has maximum extension "in the past", for $\tau = -\infty$, and for $\tau = t - r/c_0$ it is zero. The solution of the inhomogeneous wave equation leads to sound pressure level expression. This is an integral-differential equation which formally has the aspect of

$$p'(\mathbf{x}, t) = p'_T(\mathbf{x}, t) + p'_L(\mathbf{x}, t) + p'_Q(\mathbf{x}, t) \tag{1.42}$$

where T stands for "thickness", L for "loading" and Q is the quadruple term.

The first two terms are:

$$4\pi p'_T(\mathbf{x},t) = \frac{\partial}{\partial t}\int_S \left[\frac{\rho_0 v_n}{r\,|1-M_r|}\right]_\tau dS \tag{1.43}$$

$$4\pi p'_L(\mathbf{x},t) = \frac{1}{c_0}\frac{\partial}{\partial t}\int_S \left[\frac{\tilde{p}\hat{\mathbf{n}}\cdot\hat{\mathbf{r}}}{r\,|1-M_r|}\right]_\tau dS + \int_S \left[\frac{\tilde{p}\hat{\mathbf{n}}\cdot\hat{\mathbf{r}}}{r^2\,|1-M_r|}\right]_\tau dS \tag{1.44}$$

These two relations constitute the *formulation 1*, derived by Farassat (1975), where $\hat{\mathbf{r}}$ is the unit vector in direction of r and M_r is the projection of Mach vector in direction observe-source. Few observations:

- The kernls of the integral terms are all evaluated at emission time τ
- In the loading term two contributes appear: one proportional to r^{-1} acting in the far field; others characterized by r^{-2}-behavior which prevails in the near field.
- Time difference between emission τ and receiving of the signal t is called *compressibility delay* and indicates the sound travels at finite speed.
- Formulation 1 takes into account only the contribution of the thickness and loading components.

From a computational point of view, formulation 1 is not convenient because the time-derivatives are computed out the integrals, bringing numerical inaccuracy in the solution. For this reason, Farassat (1981) proposed a new formulation, where commutation between derivation and integration is performed. This is known as *formulation 1A*.

$$4\pi p'_T(\mathbf{x},t) = \int_S \left[\frac{\rho_0 \dot{v}_n}{r\,|1-M_r|^2}\right]_\tau dS + \int_S \left[\frac{\rho_0 v_n (r\dot{M}_i\hat{r}_i + c_0 M_r - c_0 M^2)}{r\,|1-M_r|^3}\right]_\tau dS \tag{1.45}$$

$$\begin{aligned} 4\pi p'_L(\mathbf{x},t) = {} & \frac{1}{c_0}\int_S \left[\frac{\dot{\tilde{p}}\cos\theta + \tilde{p}\dot{\hat{n}}_i\hat{r}_i}{r\,|1-M_r|^2}\right]_\tau dS + \int_S \left[\frac{\tilde{p}\cos\theta - \tilde{p}M_n}{r^2\,|1-M_r|^2}\right]_\tau dS \\ & + \int_S \left[\frac{\tilde{p}\cos\theta}{r^2\,|1-M_r|^3}\left(r\dot{M}_i\hat{r}_i + c_0 M_r - c_0 M^2\right)\right]_\tau dS \end{aligned} \tag{1.46}$$

where $\dot{v}_n = \dot{v}_i\hat{n}_i + v_i\dot{\hat{n}}_i$, θ is the angle formed by the two directions $\hat{\mathbf{n}}$ and $\hat{\mathbf{r}}$.

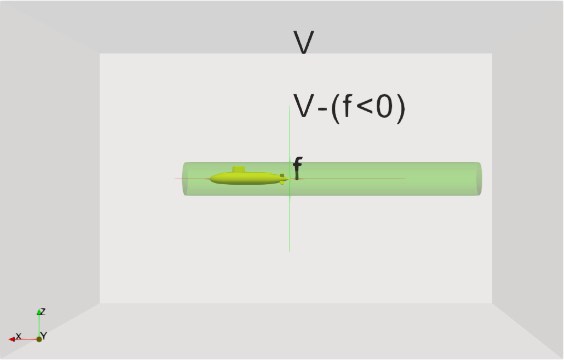

Figure 1.5: Schematic representation of the porous surface f, enclosing a solid body, inside the computational domain V

1.5.5 The porous formulation

The surface f can be identified with the body surface or might be an external porous (or equivalently permeable) surface, containing the body (Francescantonio, 1997) (Lyrintzis, 1994) within its boundaries, as schematically shown in figure 1.5. This means that the flow is allowed to cross f with velocity u_n, which in turns may be in motion with its own velocity $\mathbf{v}$. In general $u_n \neq v_n$. The surface f is contained itself into the fluid-dynamic grid, keeping enough away from the boundaries. In this case, the acoustic solution is radiated towards f, whose task is to capture the contributes to the noise deriving from the linear terms and the fraction of the volume quadrupole term contained within f. In addition, the computation of the volume term for the computational domain outside the porous surface should be done. Obviously, the larger is f, the less the contribution of the volume integral will be important. In the limit it will be negligible. This offers a convenient way to resolve the acoustic problem, which might require to resolve only surface integrals.

The porous formulation of the FW-H integral equation assumes the form:

$$\begin{aligned}4\pi\hat{p}_{2D}(\mathbf{x},t) =&\frac{\partial}{\partial t}\int_{f=0}\left[\frac{\rho_0 U_i\hat{n}_i}{r\,|1-M_r|}\right]_\tau dS_p+\frac{1}{c_0}\frac{\partial}{\partial t}\int_{f=0}\left[\frac{L_{ij}\hat{n}_j\hat{r}_i}{r\,|1-M_r|}\right]_\tau dS_p+\\ &\int_{f=0}\left[\frac{L_{ij}\hat{n}_j\hat{r}_i}{r^2\,|1-M_r|}\right]_\tau dS_p+\hat{p}_{3D}|_{V-(f<0)},\end{aligned} \tag{1.47}$$

Where the terms $U_i = (1-\frac{\rho}{\rho_0})v_i + \frac{\rho}{\rho_0}u_i$ and $L_{ij} = \tilde{P}_{ij}\hat{n}_j + \rho u_i(u_n - v_n)$ allow to maintain a structure of the equation similar to that already seen. One of the drawbacks of this formulation is that the surface should enclose all possible noise sources. In practice this is sometimes not possible (or really difficult to realize), as for example in the case of a turbulent wake, which propagates downstream for distances larger than the porous surface (as we saw in chapter 3). When the turbulent wake crosses the porous surface it generates spurious contribution to noise (Cianferra *et al.*, 2019*a*). This is know as "end-cap problem". Another feature of this formulation is the need for a convergence study, as the solution might depend upon the dimensions of the arbitrary chosen surface f surrounding the acoustic fluid-dynamic sources and from the grid resolution enclosed into the porous surface. Nevertheless, today the porous formulation is the standard approach implemented in computational acoustic solvers.

1.5.6 Formulations 1C and 1D. The advective FW-H equation

Lighthill's work has been subject to continuous improvements. After Farassat (1975) and Farassat (1981), the prediction of sound pressure level was made possible for problems of a moving body in quiescent medium. The classical FW-H equation and its 1 and 1A formulations do not explicitly take into account the presence of a mean flow. In the case of mean flow we talk about *wind tunnel problem* (Najafy-Yazdi *et al.*, 2010). The acoustic solution to this problem applying formulation 1A requires to transform the given wind-tunnel problem into a moving-observer problem, where the observer is assumed to be moving at a constant speed in a quiescent environment. Morino (1974) proposed a different approach, where the presence of the mean flow explicitly appears into the resolving wave equation in advective form. Casalino (2003) proposed to change the time derivative of the FW-H with Lagrangian derivative:

$$\frac{\partial}{\partial t} \rightarrow \frac{\partial}{\partial t} + U_0 \frac{\partial}{\partial x_1} \tag{1.48}$$

Obviously this substitution applied *tout court* to FW-H equation is not sufficient to get the correct results. Thus, to arrive to the FW-H in advective form it is necessary to repeat the whole procedure, starting from conservation laws written in advective form. The process of derivation of FW-H in advective form is done in Najafy-Yazdi *et al.* (2010). The author limited the analysis to the only linear terms and, using Green function (also in advective form), derived the acoustic pressure.

$$\begin{aligned} 4\pi\hat{p}_{2D}(\mathbf{x},t) =& \frac{\partial}{\partial t}\int_{f=0}\left[\left(1-M_0\hat{r}_1\right)\frac{\rho_0 u_i \hat{n}_i}{r^*}\right]_\tau dS - U_\infty \int_{f=0}\left[\frac{\rho_0 u_i \hat{n}_i \hat{r}_1^*}{r^{*2}}\right]_\tau dS \\ &+ \frac{1}{c_0}\frac{\partial}{\partial t}\int_{f=0}\left[\frac{L_{ij}\hat{n}_j\hat{r}_i}{r^*}\right]_\tau dS + \int_{f=0}\left[\frac{L_{ij}\hat{n}_j\hat{r}_i^*}{r^{*2}}\right]_\tau dS, \end{aligned} \tag{1.49}$$

where the second order tensor L_{ij} is given by:

$$L_{ij} = [\rho_0 u_i(u_j + U_\infty \delta_{1j}) + P_{ij}]. \tag{1.50}$$

and $P_{ij} = \tilde{p}\delta_{ij} - \sigma_{ij} \approx \tilde{p}\delta_{ij}$. This is know as **formulation 1C**. In this case the surface f is stationary but permeable.

When both the observer and the source are stationary ($\mathbf{v} = \mathbf{0}$), the surface f coincides with the solid wall of the immersed body (therefore the non-porosity condition is verified $u_n = v_n$), and the medium is moving at finite velocity, the equation 1.49 assumes the simpler form of advective Curle's equation (this happens also in the present study about BB2).

$$4\pi\hat{p}_{2D}(\mathbf{x},t) = \frac{1}{c_0}\frac{\partial}{\partial t}\int_{f=0}\left[\frac{\tilde{p}\hat{n}_i\hat{r}_i}{r^*}\right]_\tau dS + \int_{f=0}\left[\frac{\tilde{p}\hat{n}_i\hat{r}_i^*}{r^{*2}}\right]_\tau dS, \tag{1.51}$$

The work of Najafy-Yazdi *et al.* (2010) excludes the quadruple term because considered negligible with respect to thickness and loading terms. This last statement can be considered true in many applications, but not in hydroacoustic, where the quadruple term has the same dignity (or even more) of the other terms. Cianferra *et al.* (2019*a*) extended the work of Najafy-Yazdi *et al.* (2010) to include the quadruple term. We name this formulation as **formulation 1D**.

In formulation 1D, the acoustic pressure from the quadruple term is given by:

$$\begin{aligned}4\pi\hat{p}_{3D}(\mathbf{x},t) =& \frac{1}{{c_0}^2}\frac{\partial^2}{\partial t^2}\int_{f>0}\left[T_{ij}\left(\frac{\hat{r}_i\hat{r}_j}{r^*}\right)\right]_\tau dV \\ &+ \frac{1}{c_0}\frac{\partial}{\partial t}\int_{f>0}\left[T_{ij}\left(\frac{2\,\hat{r}_i\hat{r_j}^*}{{r^*}^2} + \frac{\hat{r^*}_i\hat{r_j}^*{R_{ij}}^*}{\beta^2\,{r^*}^2}\right)\right]_\tau dV \\ &+ \int_{f>0}\left[T_{ij}\left(\frac{3\,\hat{r}_i\hat{r_j}^*}{{r^*}^3}\right)\right]_\tau dV\end{aligned} \tag{1.52}$$

where:

$$T_{ij} = \rho_0 u_i u_j + (\tilde{p} - {c_0}^2\tilde{\rho})\delta_{ij} \tag{1.53}$$

and $\tau = t - r/c_0 = t - \frac{|\mathbf{x}(t)-\mathbf{y}(\tau)|}{c_0}$.

1.5.7 Compressibility delays

Compressibility delay indicates that, because sound travels at finite speed, the observer receives the signals emitted by all sources at the times $\tau < t$, only at time t. This can be seen by looking at the general structure of equations 1.49 and 1.52. Taking for example the linear term we have:

$$\hat{p}(\mathbf{x},t) \propto \int_{f=0}[\cdots]_\tau\, dS,$$

where the sum in the space of the kernels of the integrals, evaluated at times τ, gives the sound pressure level in one point at a certain time step.

To perform this kind of integral (i.e. considering also the compressibility delay) requires huge amount of computational time and memory and, for this reason, it is preferable to avoid it where is possible. In particular in cases the compressibility delay is negligible, time delay can be neglected and volume integration becomes This scenario can be reached as a trade off between the range of frequencies considered (not all the frequency band is relevant to engineering applications) and the distance source-observer. To discriminate whether time delays can be omitted, Cianferra *et al.* (2019*a*) proposed a parameter called *Maximum Frequency Parameter*. MFP states that if:

$$\frac{1}{MFP} = \Delta_{del}\, f_{max} < 1, \tag{1.54}$$

then the effect of compressibility can be omitted and the sound pressure wave can be considered traveling at infinite speed. In equation 1.54 f_{max} is the maximum frequency of the fluid dynamic phenomena and Δ_{del} is given by:

$$\Delta_{del} = \frac{\max\limits_{\mathbf{y}\in S} |\mathbf{y} - \mathbf{x}_{mic}| - \min\limits_{\mathbf{y}\in S} |\mathbf{y} - \mathbf{x}_{mic}|}{c_0}. \tag{1.55}$$

From practical point of view, it is necessary to know the highest significant frequency of the problem. If the product $f_{max}\,\Delta_{del} > 1$, then it is possible to reduce Δ_{del}, which is a measure of the distance between source and observer.

2

RANS of the BB2 submarine

2.1 Overview

In the present chapter Reynolds-Averaged Navier-Stokes simulation results will be analyzed and discussed. Qualitative description of the flow generated around the BB2 was addressed in section 1.1 relatively to figure 1.1. The flow has been studied at two different Reynolds number $Re_L = 9.57 \times 10^6$ and $Re_L = 1.2 \times 10^6$ and using two different methodologies: resolving the RANS equations up to the viscous sub-layer (WR-RANS) and using mathematical models (wall-functions) to predict the flow behavior at the wall (WM-RANS). In all cases, we use the OpenFOAM framework which solves the governing equations using finite volume discretization over unstructured grids. Initially the analysis was conducted at high Reynolds number, accordingly to the prescription of the AVT-301 NATO work group. At this flow regime numerical results for comparison purposes were largely available, allowing us also to set up the OpenFOAM environment correctly. Afterwards, pursuing the purpose to perform a Wall-Modeled Large-Eddy Simulation, followed by an hydro-acoustic analysis, we decided to switch to a lower Reynolds number regime. The reason was twofold. The first reason was the available literature about LES of submarines, which is mostly focused on Reynolds number of the order of one million. The second reason was dictated by the availability of computational resources, which must be carefully considered before starting such an analysis. Returning to RANS simulations, we will show that, at high Reynolds with the submarine advancing straight-ahead, the utilization of wall-functions is a reliable approach. On the other hand, at the lower Reynolds number, this strategy appears less robust because of regions of laminar flow and transitional turbulence with the results depending also on the particular discretization scheme adopted.

2.1.1 Reference frame, local and global quantities

Figure 2.1(a) shows the computational domain size. In y- and z-directions the domain bounds are at $\pm 13D$. Figure 2.1(b) shows the global coordinate system. The origin of this right-handed coordinate system is located at the intersection of the longitudinal axis of symmetry of the hull, midship and centre-plane, with x directed forward, y to port side and z vertically upward. Global quantities as forces and moments are provided in dimensionless form and refereed to the reference frame already mentioned.

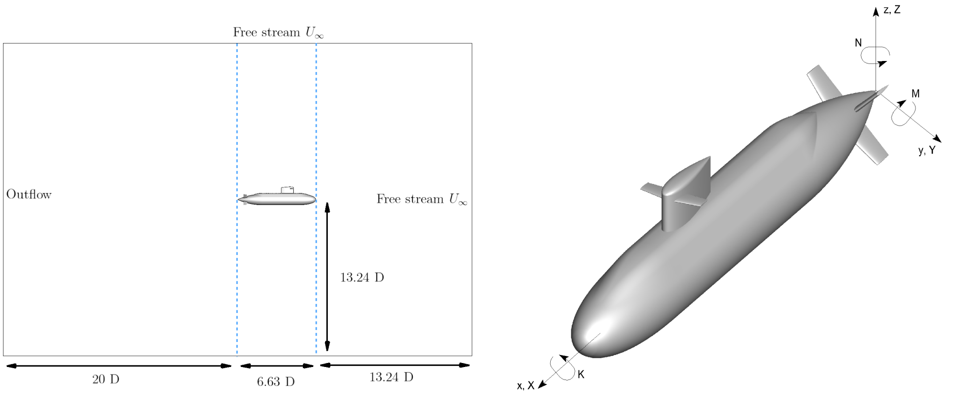

(a) Computational domain (b) Reference frame, forces and moments

Figure 2.1: Computational domain and Reference frame

We will refer to the following list of forces and moments:

- Non-dimensional frictional resistance X'_f
- Non-dimensional pressure resistance X'_p
- Non-dimensional total resistance X'

- Non-dimensional vertical force Z'
- Non-dimensional pitch moment force M'

All integral forces X, Y, Z and moment K, M, N are directed as shown in figure 2.1 and they are made non-dimensional as:

$$X', Y', Z' = \frac{X, Y, Z}{\frac{1}{2}\rho U_\infty^2 L_{oa}^2}$$

$$K', M', N' = \frac{K, M, N}{\frac{1}{2}\rho U_\infty^2 L_{oa}^3}$$

In agreement with the NATO work-group AVT-301, the results of RANS simulations will be reported in non-dimensional form. They are listed in table 2.1

Original variable	**Data reduction**	**Name**
Cartesian coordinates	$\{x', y', z'\} = \{x, y, z\}/L_{oa}$	x, y, z
velocities	$\langle U \rangle / U_\infty$	u, v, w
vorticity	${\omega'}_{\{x,y,z\}} = \omega_{\{x,y,z\}} \cdot L_{oa}/U_\infty$	$vortx$, $vorty$, $vortz$
pressure	$C_p = (p - p_\infty)/(\frac{1}{2}\rho U_\infty^2)$	C_p
skin friction	$C_f = \tau_x/(\frac{1}{2}\rho U_\infty^2)$	C_f
turbulent kinetic energy	$k' = k/U_\infty^2$	k'

Table 2.1: Flow quantities

RANS local results are provided at submarine's hull surface and in W, P, Y and H planes, which are shown in figure 2.2 and described in table 2.2.

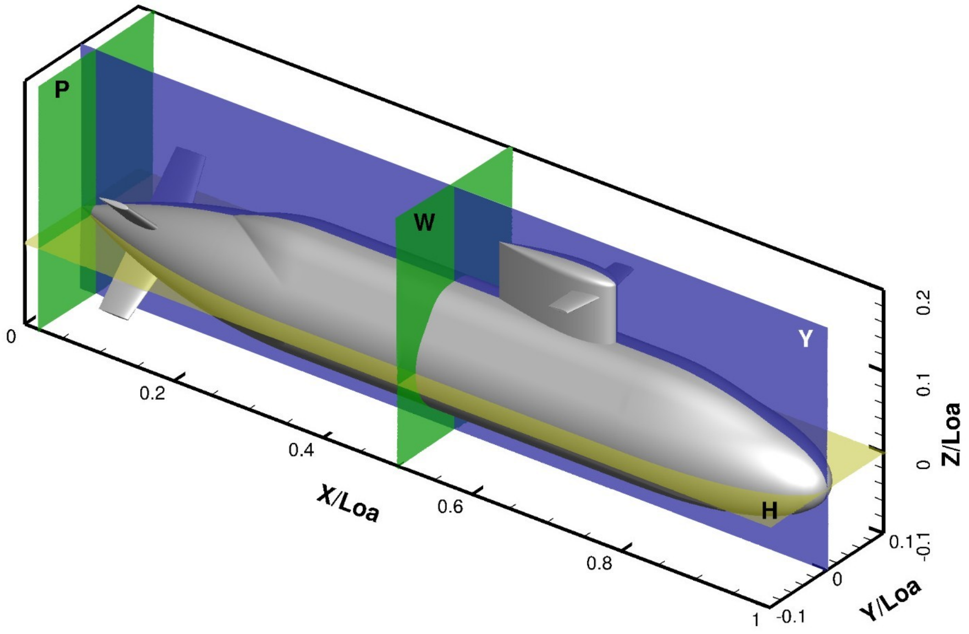

Figure 2.2: Definition of planes W, P, Y, H

Name	Location	Description
W	x/L_{oa}=0.5	Behind sail plane
P	x/L_{oa}=0.0189	Propeller plane
Y	y/L_{oa}=0	ZX symmetry plane (transverse plane)
H	z/L_{oa}=0	XY symmetry plane (horizontal plane)

Table 2.2: Reference planes

2.1.2 Spatial discretization: RANS Grids

RANS simulations were performed on different grids. The grids differ in topology, cell/point density, near-wall resolution (i.e. the distance of the cell-center of wall-adjacent cell from the wall). Table 2.3 reports these information. GR1 and GR2 are multi-blocks structured grids. GR1, contains an unstructured block, populated by only tetrahedral cells and surrounding the structured core and occupies the far field. For this reason we still classify it as a multi-block structured grid (although OpenFOAM treats all the grids as unstructured). Tetrahedral meshes with prism boundary-layer cells around the fuselage will be named "hybrid-grids". **GR1** was shared in AVT-301 work group from the **Defence Research and Development Canada**. In particular, they provided the Pointwise [1] file of the grid and we modified it to our purposes. **GR2** was shared by **Marin** in OpenFOAM format and was not modifiable.

Grid topology	**Grid ID-code**	**N. cells** ($\times 10^6$)	**Wall treatment**	**hull** $\langle y^+ \rangle$	**Re**
GR1	GR1a	24.5	WR	0.088	9.57×10^6
	GR1b	20.3	WM	26.5	9.57×10^6
	GR1c	24.4	WR	0.28	1.2×10^6
	GR1d	15.8	WM	50	1.2×10^6
GR2	GR2a	14.5	WR	1	$9.57 \cdot 10^6$
	GR2b	7.5	WR	1.3	9.57×10^6
	GR2c	3.5	WR	1.7	9.57×10^6

Table 2.3: RANS grids information

2.2 RANS of the BB2 at Re=9,570,000

In the present section RANS simulations for the BB2 submarine in its fully appended configuration will be discussed. Computations are pursued at model scale, with Reynolds number equal to:

$$Re_L = \frac{U_\infty L}{\nu} = \frac{3\ \mathrm{m/s} \times 3.826\ \mathrm{m}}{1.2 \cdot 10^{-6}\ m^2/\mathrm{s}} = 9.57 \cdot 10^6$$

We will proceed making a comparison between the results obtained using the grids GR1a and GR1b. The grid GR1a is designed to solve the RANS equations up to the submarine surface, where the mathematical boundary condition of impermeability is prescribed on the velocity field. In this case the averaged value of $y^+ = \frac{u_\tau y}{\nu}$ is

---

[1] Pointwise is a commercial software for general purposes grid generation

of the order of $\mathcal{O}\left(10^{-1}\right)$. The grid GR1b is tough to use wall-functions. We use the OpenFOAM 's native *nutUSpaldingWallFunction* that calculates u_τ solving the Spalding's continuous law of the wall:

$$y^+ = u^+ + \frac{1}{E}\left[e^{\kappa\, u^+} - 1 - \kappa u^+ - \frac{\left(\kappa\, u^+\right)^2}{2!} - \frac{\left(\kappa\, u^+\right)^3}{3!} \right]$$

where $u^+ = \frac{\langle U \rangle}{u_\tau}$, κ=0.41 is the von Karman constant, E=9.8 is a model constant. The turbulence model utilized is the Shear Stress Transport $k-\omega$.

2.2.1 Computational framework

The solution algorithm for pressure-velocity coupling used is the Semi-Implicit Method for Pressure-Linked Equations Consistent (SIMPLEC) (Patankar, 1980). The solver used for the pressure is the standard OpenFOAM multigrid GAMG with Gauss-Seidel smoother. The solver used for the momentum and the other transport equations is a stabilized preconditioned bi-conjugate gradient, PBiCGStab (for asymmetric matrices), with preconditioner diagonal incomplete-LU DILU (asymmetric).

Table 2.4 reports the relevant information about spatial discretization schemes used in RANS computations. Obviously this is not the only possible choice. Based on our experience the combination of schemes shown in the Table 2.4 gives better results for the large variety of flow conditions investigated in the present research. To arrive to this choice, an intensive campaign of numerical tests was carried out, simulating the turbulent flow at different values of the Reynolds number and using a variety of strategies for the treatment of the near wall flow.

Item	**Discretization**	**Type**	**Accuracy Order**
∇U	Gauss cellMDLimited leastSquares	least squares limited	II
$\nabla\ \{p,\, k,\, \omega\}$	Gauss linear	central differencing	II
$\nabla \cdot (\phi, U)$	bounded Gauss linearUpwind $\nabla\langle U\rangle$	bounded upwind second order	II
$\nabla \cdot k$	bounded Gauss upwind	bounded upwind	I
$\nabla \cdot \omega$	bounded Gauss upwind	bounded upwind	I
$\nabla \cdot \nu(\nabla U)^T$	Gauss linear	unbounded central differencing	II
∇^2	Gauss linear corrected	unbounded central differencing	II

Table 2.4: Discretization schemes for the RANS simulations at $Re_L = 9.57 \times 10^6$

Initial conditions are assigned as follow:

- $U = -3\,\frac{m}{s}$, mean velocity field
- $p = 0\,\frac{m^2}{s^2}$, mean kinematic pressure
- $k = \frac{3}{2}(I\,u_{ref})^2 = 0.00135\,\frac{m^2}{s^2}$, turbulent kinetic energy (with I the turbulence intensity)
- $\omega = \frac{k}{\nu}\left(\frac{\nu_t}{\nu}\right)^{-1} \approx 1125\,s^{-1}$, specific dissipation rate (with ν the fluid viscosity and ν_t the eddy-viscosity)

The boundary conditions prescribed are listed in Table 2.5, grouped by patches. With **sub-walls** it is intended all the solid boundaries of the submarine: hull, sail, sail plane, rudders.

	Inlet	**Outlet**	**Sub-walls WR**	**Sub-walls WM**
$U\ \left[\frac{m}{s}\right]$	-3	zero gradient	noSlip	noSlip
$p\ \left[\frac{m^2}{s^2}\right]$	zero gradient	0	zero gradient	zero gradient
$k\ \left[\frac{m^2}{s^2}\right]$	0.00135	zero gradient	0	kqRWallFunction
$\omega\ [s^{-1}]$	1125	zero gradient	omegaWallFunction	-
$\nu_t\ \left[\frac{m^2}{s}\right]$	calculated	calculated	0	nutUSpaldingWallFunction

Table 2.5: Boundary conditions for the RANS simulations at $Re_L = 9.57 \times 10^6$

2.2.2 Residuals and forces

Figures 2.3 (a) and (b) show the residual convergence history for both simulations. We see a smooth convergence. Looking at figure 2.3 (a), after about 4000 iterations the residuals drop of four orders of magnitude. The convergence history it is similar for all the fluid-dynamic variables. Figure 2.3 (b) shows that after about 3000 iterations residuals values of the simulation WM were not changing anymore. Although not shown explicitly, forces and moments also have reached convergence for both cases (a) and (b). Table 2.6 shows a comparison of the forces and moments between present simulations and with the average value of all the simulations presented in the framework of the AVT-301 group. The usage of wall functions results in higher values of the vertical and streamwise forces.

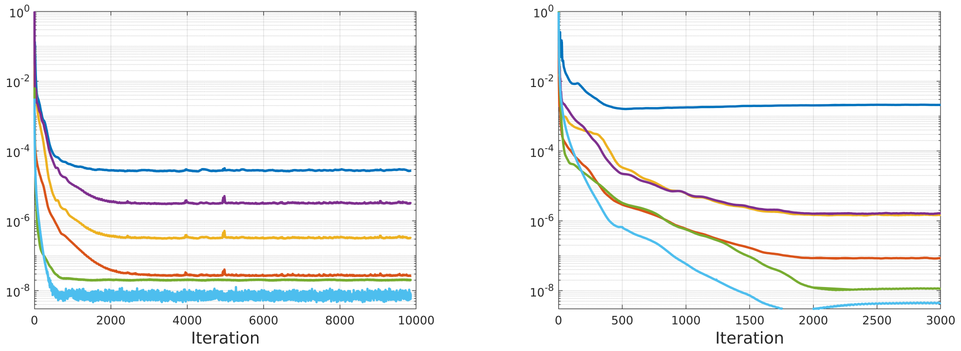

(a) Wall-resolved approach

(b) Wall-modeled approach

Figure 2.3: Linear solver residuals: p (—), U_x (—), U_y (—), U_z (—), k (—), ω (—)

	Wall-resolved	Wall-modeled	AVT-301 Average
$-X'_p \times 10^3$	0.218	0.242	-
$-X'_f \times 10^3$	1.384	1.428	-
$-X' \times 10^3$	1.602	1.668	1.590
$Z' \times 10^3$	1.361	1.369	0.130
$-M' \times 10^3$	0.074	0.080	0.090

Table 2.6: Forces and moments for the RANS simulations at $Re_L = 9.57 \times 10^6$

2.2.3 Hull

Figure 2.4 shows the grid GR1a at the solid surface of the submarine. The cells are hexahedral, characterized by low skewness. When using wall-layer models, the topology is exactly the same of GR1a, and the difference is in the height of the first cell at the wall. Figure 2.4(a) shows cell clustering at the junctions between the sail and the hull and between the sail and the sailplane. The contour plots of y^+ in figure 2.5 show the grids both to be properly designed at the wall for solve the

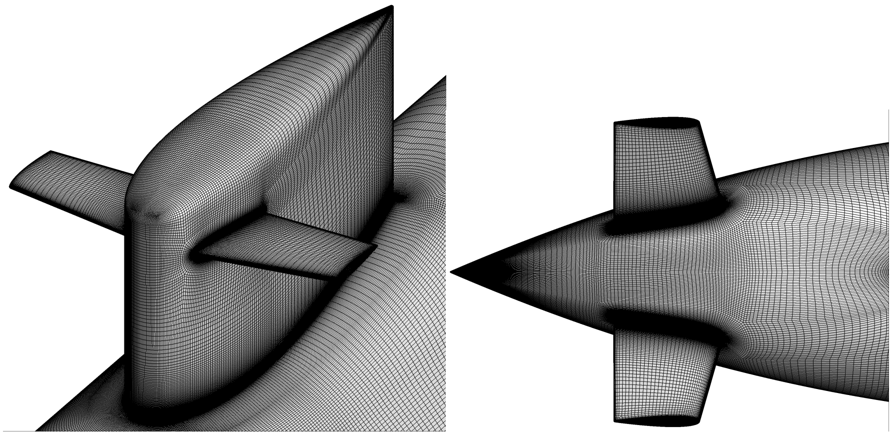

(a) Sail view (b) Rudders view

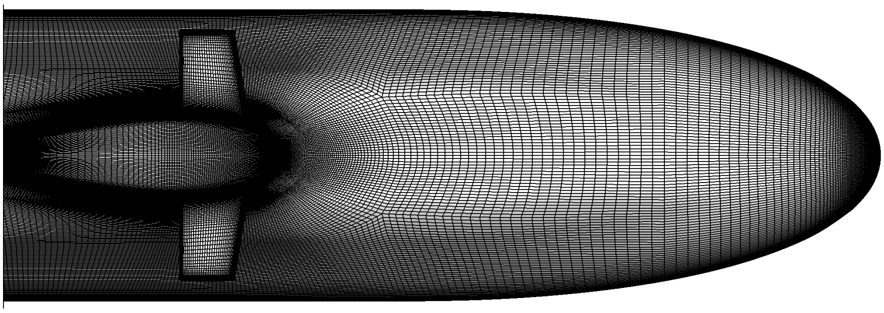

(c) Front top view

Figure 2.4: Surface mesh on submarine used in wall-resolving simulation

boundary layer or to model it, respectively: in figure 2.5(a) y^+ is everywhere below unity and this ensures solution of the RANS equations up to the viscous sub-layer. Within a distance equal to $10\,\delta_\nu$ from the submarine surfaces, the grid contains 20 cells. This guarantees a good resolution of the velocity gradients close to the wall.

Figure 2.6 shows a comparison of the pressure coefficient contours along the submarine. The two fields appear almost identical. A more detailed analysis about the behavior of the pressure on the submarine will be carried out using curves obtained as intersection between the submarine and the plane Y, in subsection 2.2.8. Similarly, the two simulations provide a distribution of the skin-friction coefficient C_f

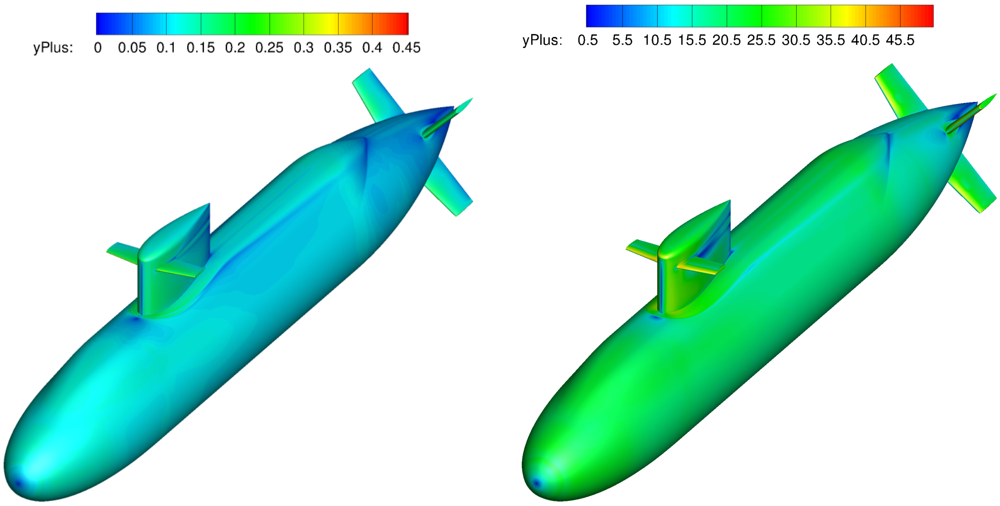

(a) Wall-resolved approach (b) Wall-modeled approach

Figure 2.5: y^+ contours on submarine

in very good agreement with reference data (see figure 2.7). The solution obtained using wall-layer model slightly overpredicts the skin-friction coefficient at the top of the sail, at the front side and at the stern, just before the rudders. A quantitative analysis is carried out in subsection 2.2.8. Around the sail, at the junction with the hull, a horse-shore vortex develops and it is then convected downstream over the upper side of the hull. In this case, its trace is visible observing the contour of τ_w as a thin longitudinal structure with very low wall-shear stress magnitude $|\tau_{\mathbf{w}}|$.

2.2.4 Grid in planes W, P and Y

Before starting the analysis of the velocity field, turbulent kinetic energy and vorticity at the three planes W, P and Y, it is worth to look at the mesh at these locations (figure 2.8). The grid shown is GR1a. The grid used for the simulation WM has the same topology and fewer cells clustered at the solid surfaces. In figure 2.8 (c) it is possible to see the part of the computational domain filled with tetrahedra. At the interface between hexahedra and tetrahedra the mesh quality has its minimum

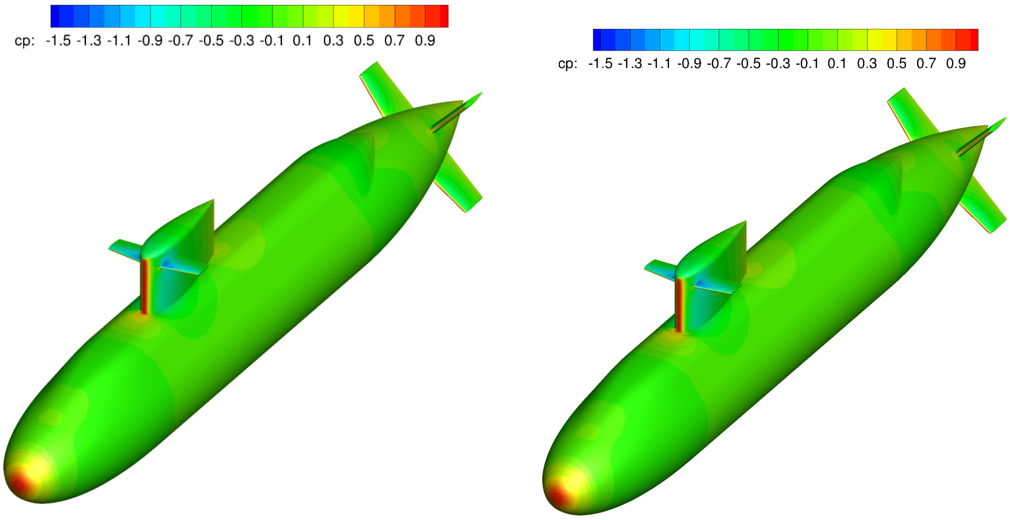

(a) Wall-resolved approach (b) Wall-modeled approach

Figure 2.6: Pressure coefficient C_p contours on submarine

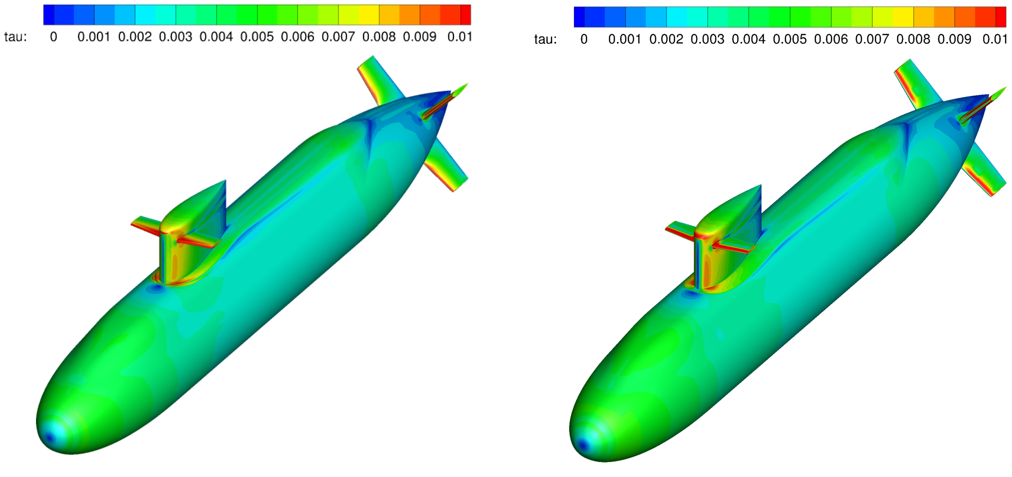

(a) Wall-resolved approach (b) Wall-modeled approach

Figure 2.7: Non-dimensional wall-shear stress contours on the hull

value in terms of non-orthogonality, equal to 74, as calculated by the OpenFOAM tool called *checkMesh*. In OpenFOAM the non-orthogonality is the angle between the line passing through the centers of two adjacent cells, and the vector normal to the face they share. The general recommendation of OpenFOAM developers is to avoid using grid with orthogonality less than 20. In figure 2.8 (d) shows the mesh at the propeller (left) and the sailplane (right) planes.

2.2.5 Behind sail plane

Figure 2.9 shows non dimensional axial velocity $u = -U_x/U_\infty$ contours over the plane behind the sail (i.e. plane W at x/L=0.5), for the two simulations WR and WM. We are looking at the sail wake at the turbulent boundary layer on the main body. At z/L=0.085, y/L=± 0.03 we see the two symmetric footprints of the horseshoe vortex and at z/L=0.15, y/L=0 we observe the presence of the footprints of the fin-tip vortex. The horseshoe vortex and the fin-tip vortex, whose legs are composed of a couple of counter rotating vortices, are easy to recognize also in figure 2.11, as zones of high x-vorticity. In case of simulation with wall-layer model, the sailplane wake is rapidly lost. In fact, its extension in y-direction is just $l \approx 0.02\,L$ while in case of wall-resolving simulation it is about twice. The footprints of the horseshoe vortex are elongated, pointing at the symmetry axes, y=0, while they appear well rounded when modeling the boundary layer.

Figure 2.10 shows the turbulent kinetic energy k contour plot that is given solving the model equation for the turbulence kinetic energy of the Shear Stress Transport $k-\omega$ model. The divergence term of k is solved using a first order upwind scheme which produces numerical diffusivity visible in figures 2.10 and 2.13.

2.2.6 Propeller plane

In the propeller plane P the wake is composed of three elements: the sail wake, where the sailplane wake faded away, the wake from the hull, that from the initially cylindrical shape turned to quasi-square, and the rudders wake. The RANS equations predict the maximum level of turbulence at the junction between the hull and the rudders. An explanation of that resides on the increasing of velocity gradients due to the proximity of the rudders and the hull (in circumferential direction), and

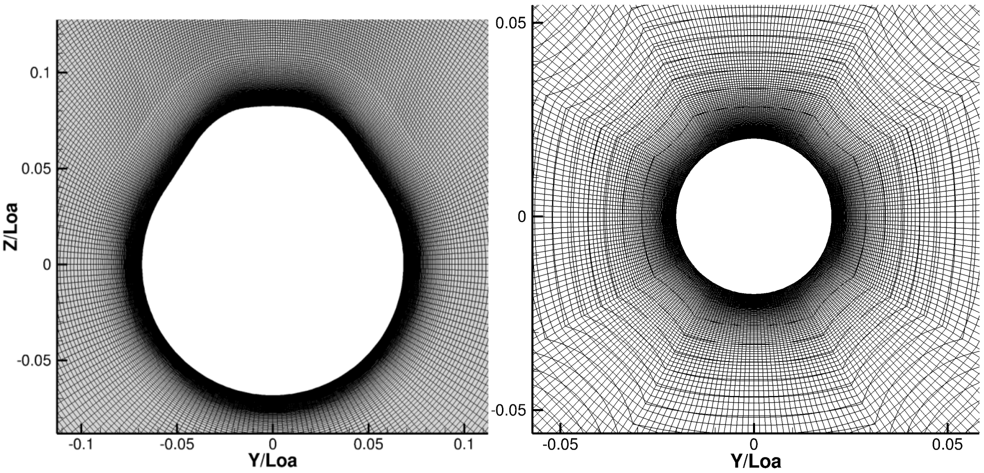

(a) behind sail plane

(b) propeller plane

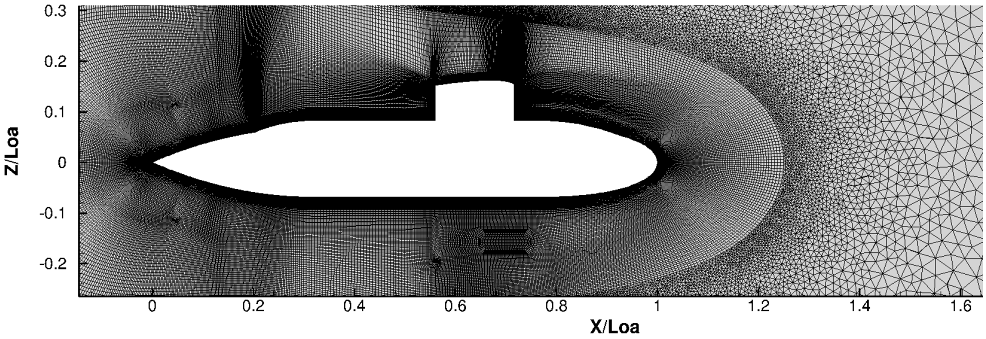

(c) transverse plane

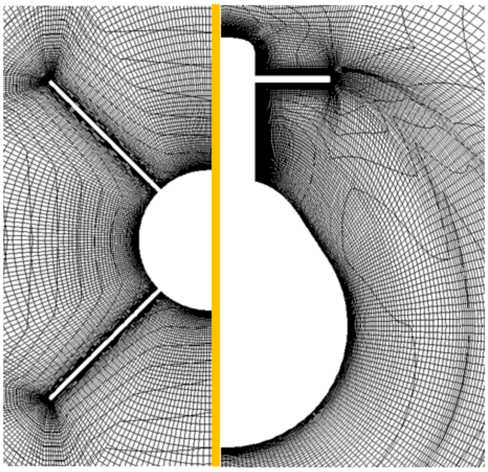

(d) Sail and Rudders view

Figure 2.8: Grid view on different planes

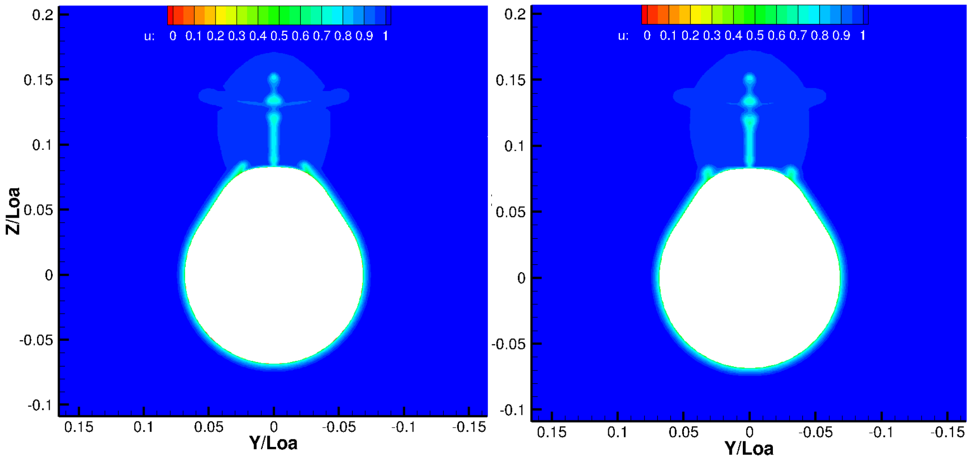

(a) Wall-resolved approach (b) Wall-modeled approach

Figure 2.9: Contours of streamwise velocity u at plane W

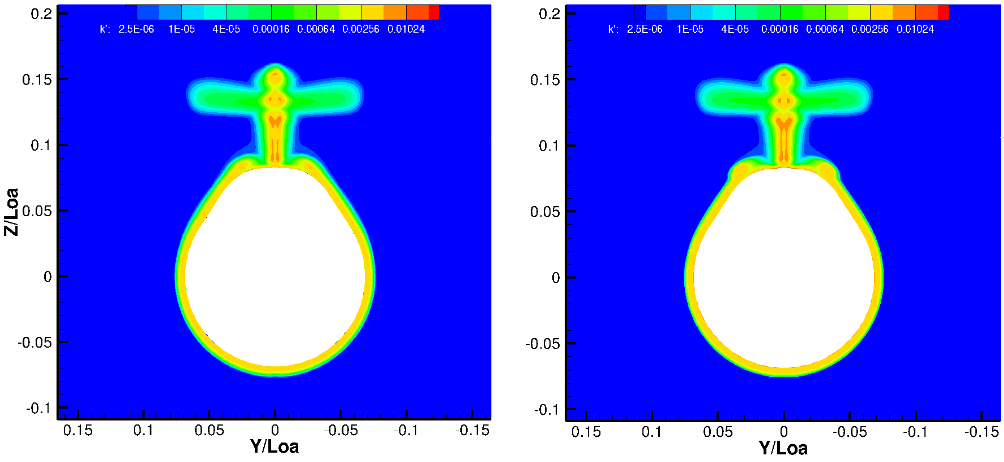

(a) Wall-resolved approach (b) Wall-modeled approach

Figure 2.10: Contours of turbulent kinetic energy k at plane W

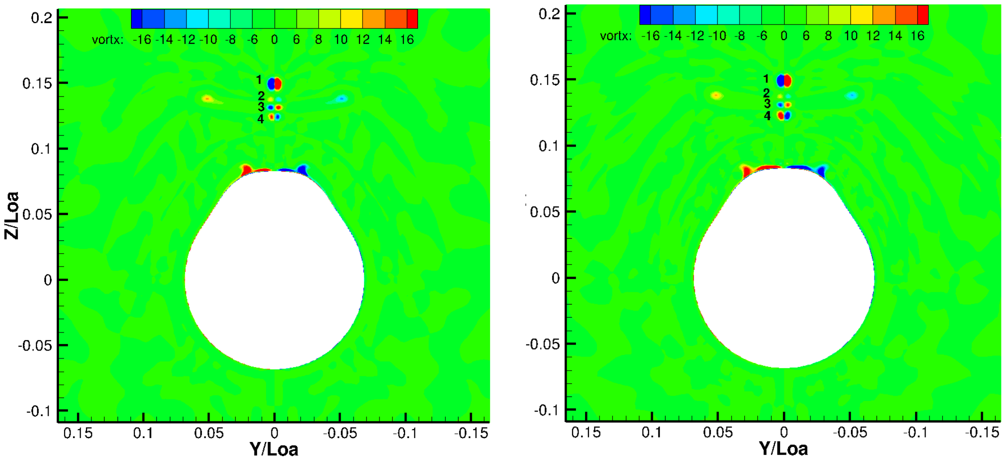

(a) Wall-resolved approach

(b) Wall-modeled approach

Figure 2.11: Contours of x-vorticity ω_x at plane W

because of the adverse streamwise pressure gradient. Velocity gradients activate the production term in the model equation of turbulent kinetic energy.

2.2.7 Transverse plane

In transverse plane of figures 2.15 (a, b) we show the development of the axisymmetric wake downstream, up to a distance L from the stern. A deep analysis of the axisymmetric wake will be carried out when treating the large-eddy simulation results. In the P plane the two solutions appear in very good agreement for u, k and ω_y, as shown in the next figures 2.15 (c, d) and 2.15 (e, f).

2.2.8 Slices

In this section we present the analysis of the pressure coefficient and of the skin-friction factor along the submarine's surface, along curves given by the intersection of the plane Y with the submarine surface. A comparison between wall-resolving and wall-modeled solution is also carried out.

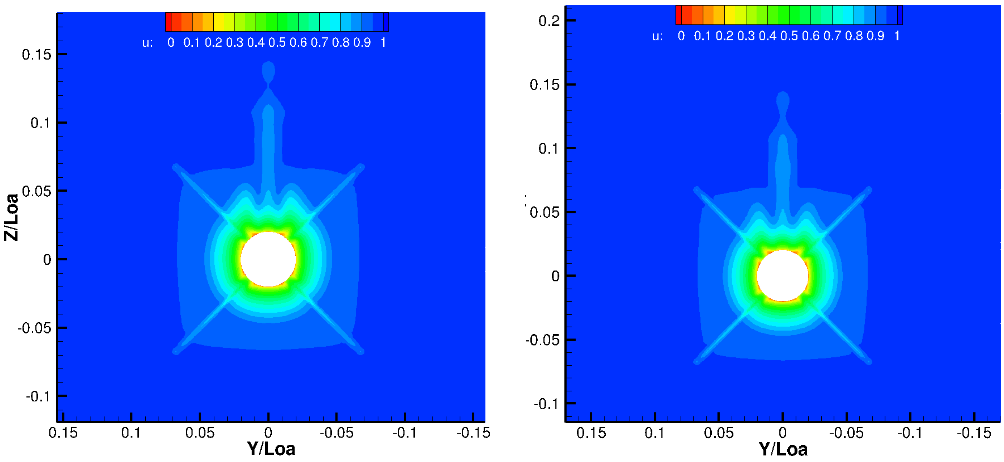

(a) Wall-resolved approach (b) Wall-modeled approach

Figure 2.12: Contours of streamwise velocity u at plane P

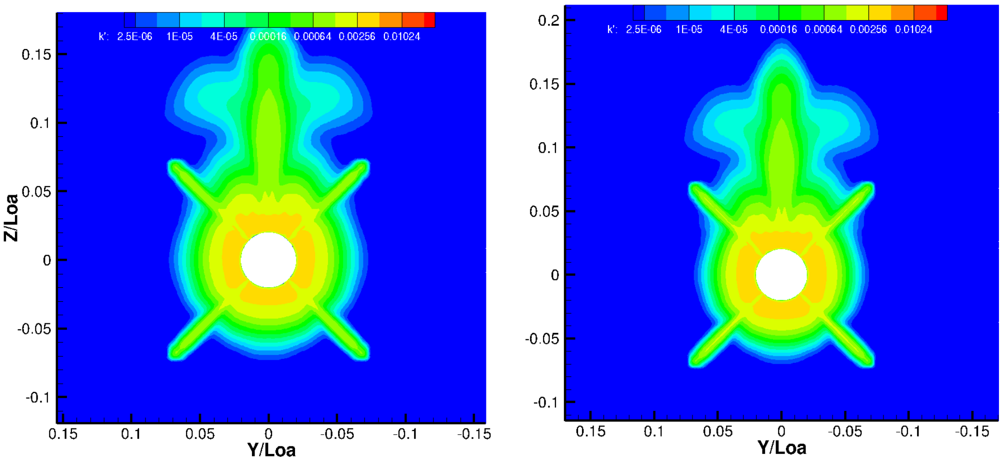

(a) Wall-resolved approach (b) Wall-modeled approach

Figure 2.13: Contours of turbulent kinetic energy k at plane P

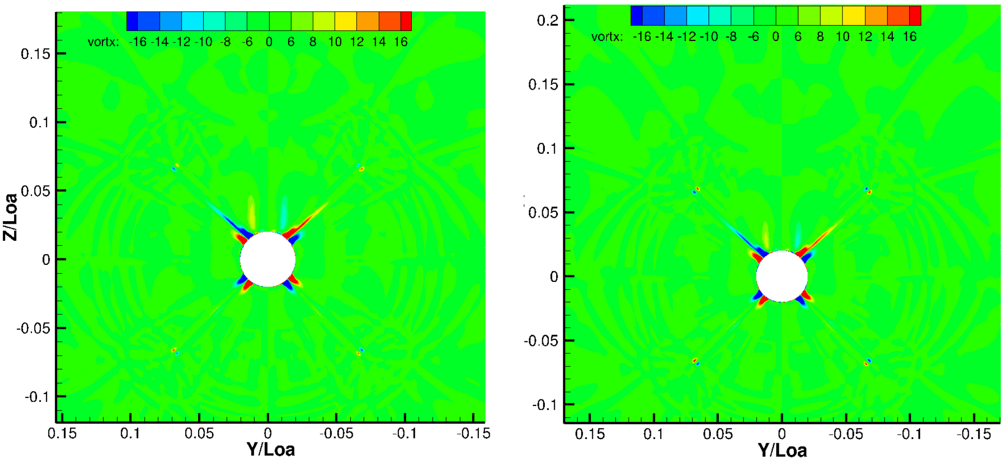

(a) Wall-resolved approach (b) Wall-modeled approach

Figure 2.14: Contours of x-vorticity ω_x at plane P

Figure 2.16 shows the pressure coefficient C_p along the upper side of the submarine for Y=0. We start from the bow, x/L=1, along the flow direction. At the bow, the pressure is maximum and $C_p = 1$. Then, it rapidly decreases related to a flow acceleration moving downstream. For $x/L \approx$0.8, $dC_p/dx = 0$ and pressure coefficient turns to grow again up to unity, at the sail. Beyond the sail, where the hull diameter is constant (from about $x/L = 0.55$) pressure decreases along the hull, reaching a local minimum at $x/L = 0.3$. From this point on, C_p increases till the stern. Figure 2.16(b) shows that the solution obtained using wall-model can predict only one vortex at x/L=0.726, whereas the solution WR reproduces two vortices (the primary at x/L=0.720 and the secondary at x/L=0.724). The presence of the vortex results in a drop of C_p. With exception of these local misalignment, there is an excellent matching between the two solutions, also in consideration of a minor computational cost of that with wall-layer model.

Figure 2.16(c) shows the pressure coefficient C_p along the bottom side of the hull. The shape of the hull on the bottom side (and on portside and starboard side) is slightly different from the upper side, and there is not sail. In the range $0.8 \leq x/L \leq 1$, on the bottom side of the hull, C_p follows a behavior similar to that on the upper side. Then, between $0.4 \leq x/L \leq 0.7$, C_p is approximately zero, as

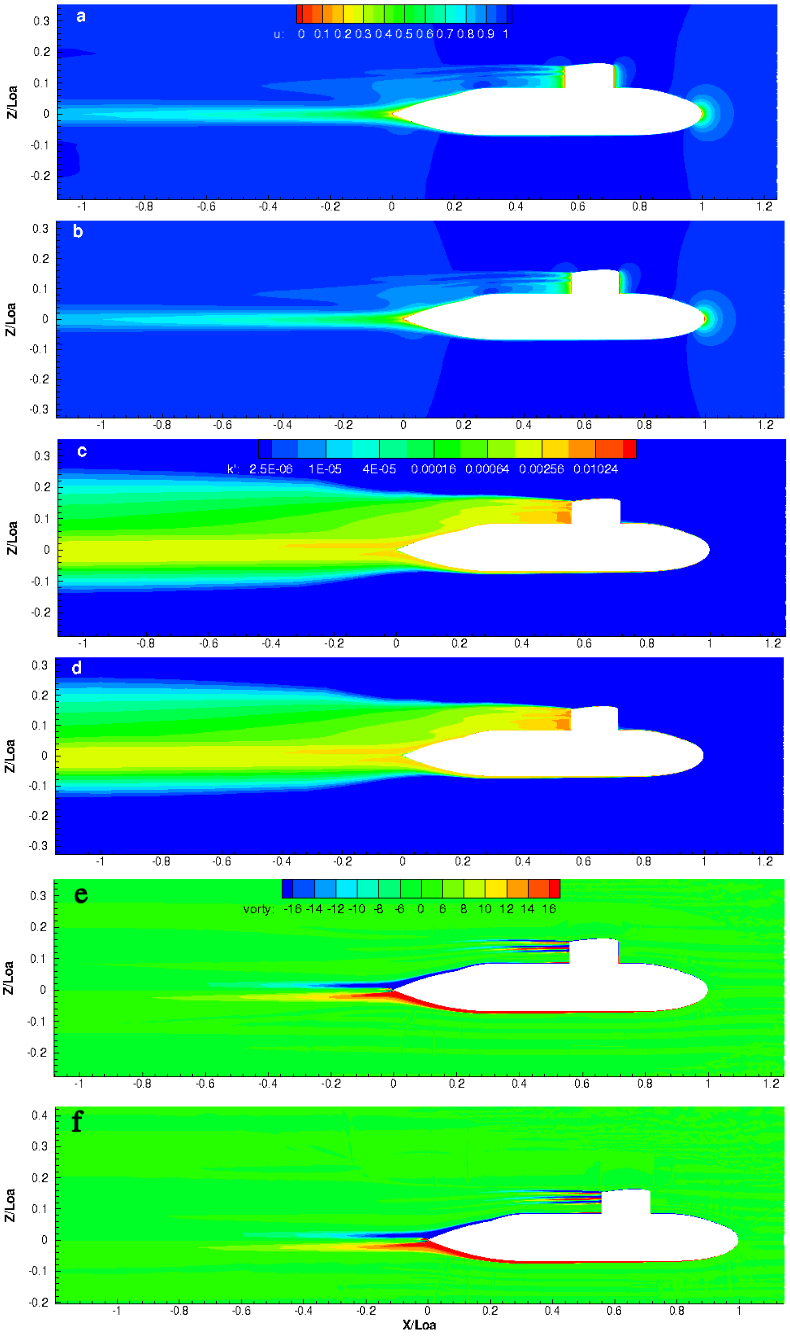

Figure 2.15: Contours of u, k and ω_y at plane Y. Figures a, c and e: wall-resolving simulations. Figures b, d and f: wall-modeled simulations

well as its x-derivative. A zero-pressure-gradient on the hull allows comparison with the canonical "zero pressure gradient turbulent flat plate flow" (ZPGTFP), widely studied in literature.

Similar arguments hold for the skin-friction coefficient C_f, as shown in figure 2.17. The two solutions are still in very good agreement and this is not so obvious, as τ_w is modeled based on the *law-of-the-wall*. We did not experienced issues modeling the boundary layer with the wall shear-stress function at $Re_L = 9.57 \times 10^6$ but, when decreasing Re to one half or one tenth of this, it is not easy to obtain an accurate value of C_f. In LES context the situation is even more complicated, as will be shown later on. The solution using shear-stress models underpredicts the maximum value of C_f by about 50% and overpredicts the minimum value. This happens at x/L=0.7 and, as already mentioned, in case of very sharp variations we have observed the wall-function solution to be smoothed out or cut off.

2.2.9 The law of the wall

Figure 2.16 (c) shows C_p along the bottom side of the hull, for $y = 0$. Around x/L=0.5 the pressure gradient in x-direction is zero. Figure 2.19 (b) shows the pressure coefficient in circumferential direction for x/L=0.5. At the bottom, for $\vartheta = 180°$, the gradient of C_p along the circumferential direction is also zero. This suggests comparison of the solution of the velocity field inside the boundary layer with the analytic log-law of the wall (Pope, 2000; Davidson, 2004). The logarithmic law of the wall holds excellently in very high-Re flows, away from high pressure gradients and separations, sufficiently close to the impermeable smooth walls but far away enough to neglect viscous effects (Bradshaw & Huang, 1995). The well-known logarithmic behavior is valid from the outer edge of the viscous wall region ($y^+ = \frac{u_\tau y}{\nu} \approx 30 - 50$) to the outer limit of y=0.2 δ, with δ being the local boundary layer thickness. It is:

$$\frac{\langle U \rangle}{u_\tau} = \frac{1}{\kappa} \ln \frac{u_\tau y}{\nu} + C \tag{2.1}$$

Finally, figure 2.19 (a) shows the velocity profile u^+ versus the viscous length y^+ in the case of wall-resolved and wall-modeled simulations. Using Spalding's formulation allows to have a relationship $u^+ = f(y^+)$ from $y^+ \approx 1$, which it is below the lower limit of equation 2.1. The agreement between the two simulations

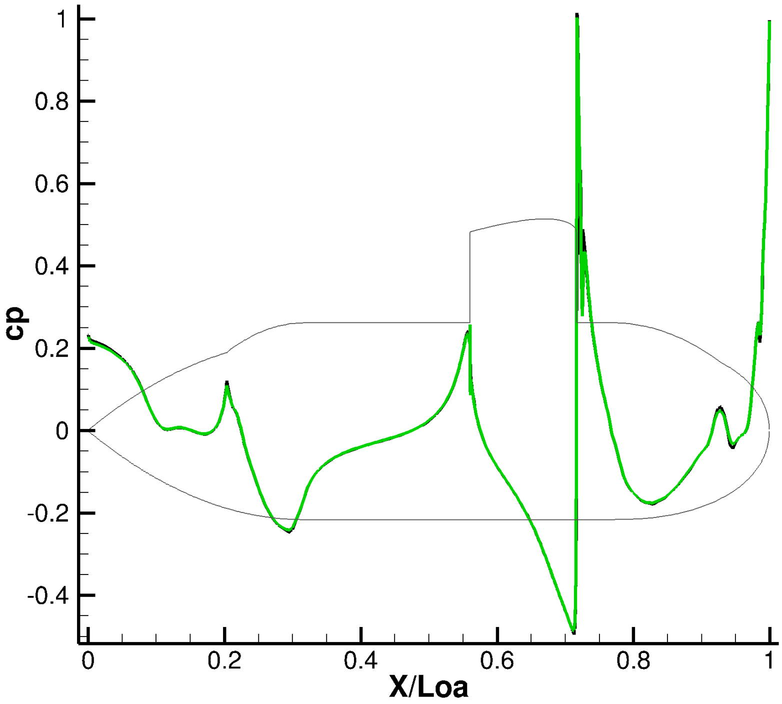

(a) Top side of the hull

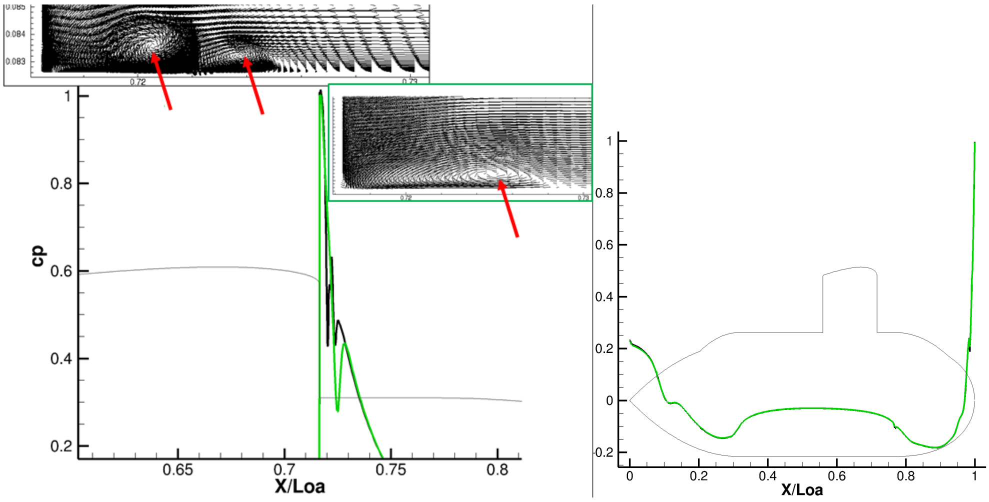

(b) Zoom to the sail

(c) Bottom side of the hull

Figure 2.16: Pressure coefficient C_p along the curve $y = 0$; wall-resolved simulation (—); wall-modeled simulation (—)

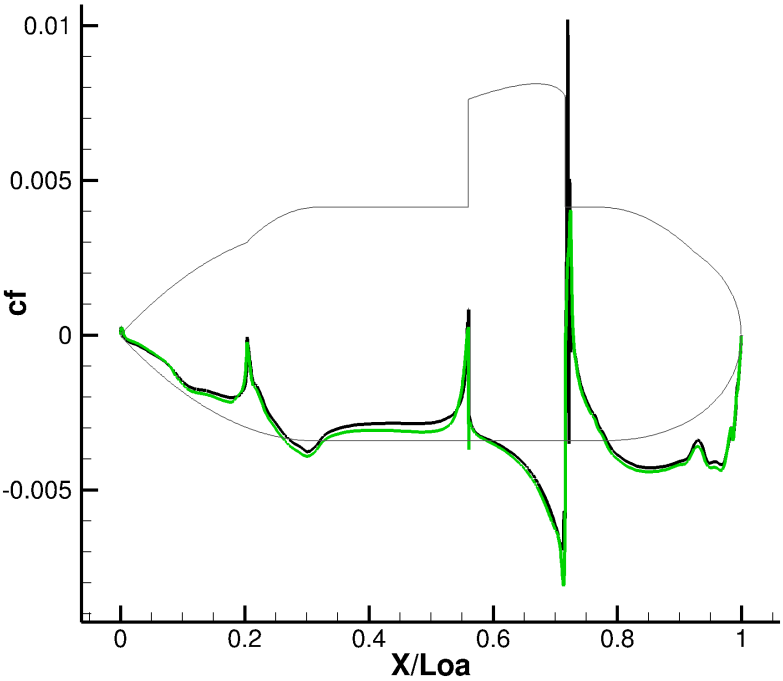

(a) Top side of the hull

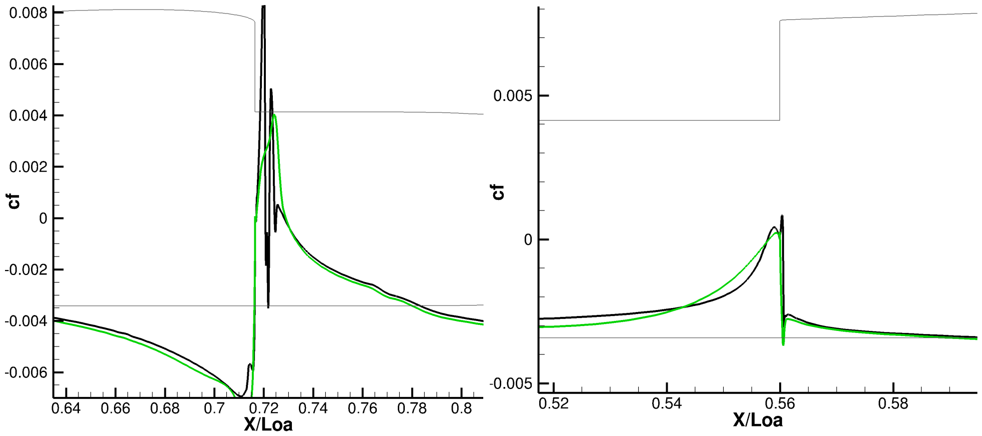

(b) Zoom to front side of the sail (c) Zoom to back side of the sail

Figure 2.17: Skin-friction coefficient C_f along the curve $y = 0$, $z > 0$; wall-resolved simulation (—); wall-modeled simulation (—)

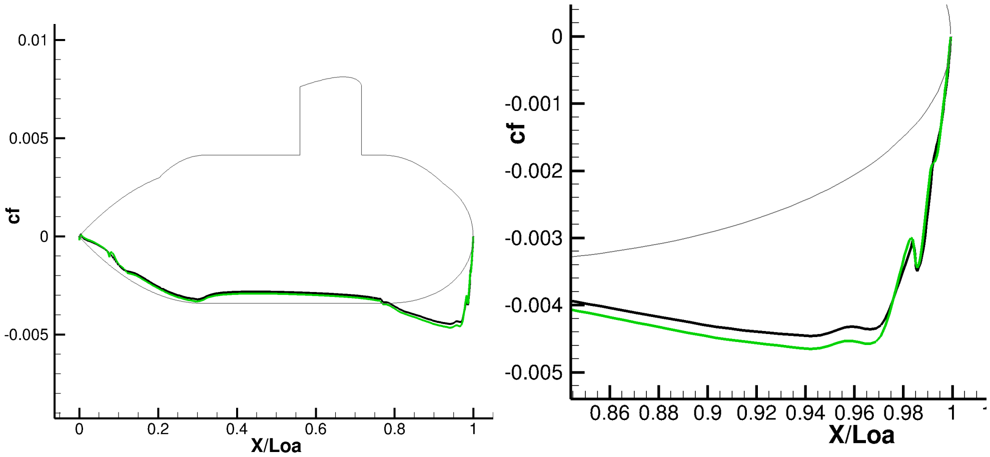

(a) Bottom side of the hull

(b) Zoom to nose

Figure 2.18: Skin-friction coefficient C_f along the curve $y = 0$, $z < 0$; wall-resolved simulation (—); wall-modeled simulation (—)

is excellent, as it is the fit with theory. In this case the law-of-the-wall can be considered valid until $y^+ = 0.2$, $\delta^+ = 420$.

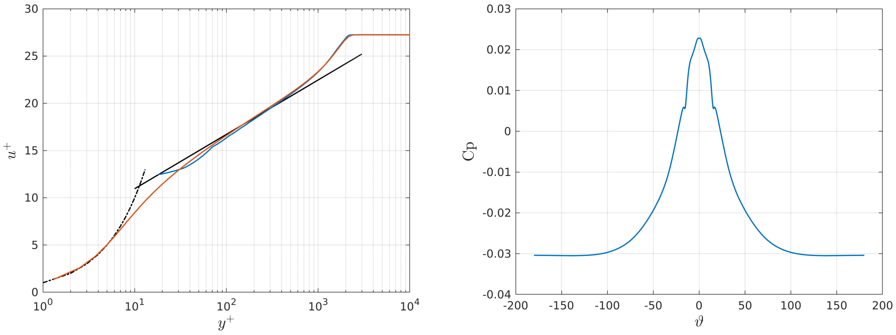

(a) (b)

Figure 2.19: The law of the wall, bottom side of the hull: RANS-WR (—), RANS-WF (—), $u^+ = y^+$ (- - -), the log-law $u^+ = 2.44\,\ln(y^+) + 5.2$ (—). (b) Cp in circumferential direction for x/L=0.5

2.3 RANS of the BB2 at Re=1,200,000

In the present section we analyze RANS simulations for the BB2 submarine at Reynolds number equal to $Re_L = 1.2 \times 10^6$ ($\nu = 9.565 \times 10^{-6}$ m^2/s). The simulations run on grids GR1c and GR1d (see 2.3). The Large-Eddy Simulation will be conducted at this Reynolds number, using the WM-RANS solution as initial condition. Reducing the Reynolds number from $Re_L = 9.57 \times 10^6$ to the present one leads to a dramatic reduction of computational efforts so that it can be afforded with the available resources. Another fact to consider is that increasing the Reynolds number leads to the need of larger grids (in order to keep the same resolution), and associated to this, increases the amount of data to be stored and eventually transferred between the cluster and the local desktop machine.

Also, at this Reynolds number, there are recent numerical works (Posa & Balaras (2016) and Kumar & Mahesh (2018)) and experimental works (Jiménez *et al.* (2010a) and Jiménez *et al.* (2010b)) we can use to make some comparisons. In these works the authors employed wall-resolving LES solution of the flow around the DARPA-SUBOFF submarine with and without appendages, at Reynolds numbers in the range 1.1-1.2 millions (see section 1.1). The previous RANS simulations at higher Re, gave us know-how on setting up a suitable numeric framework for the two cases wall-resolved WR and wall-modeled WM. Our results were compared with those obtained by the other participants in the AVT-301 collaborative work-group. However, the use of wall-functions when decreasing the Reynolds number is not straightforward. We experienced many issues about setting up suitable numerical parameters for this case and choosing the best performing turbulence model. The $k-\omega$ SST equipped with wall-functions responded badly in estimating forces and the wall-shear stress close to the bow. For this reason we adopted the classic $k-\varepsilon$ turbulence model and hereby we propose a comparison between the results from the wall-resolving simulation obtained using $k-\omega$ SST and the wall-modeled simulation obtained using the $k-\varepsilon$. Indeed it is not of our interest to evaluate all the turbulence models on this geometry and, at this stage, we intend just to explore the RANS solutions with and without wall models, in order to move on to the LES. As previously done in our research we will proceed making a comparison between the results obtained using the grids GR1c and GR1d (see table 2.3), based on the topology of *Defence Research and Development Canada*.

2.3.1 Solver and numerical schemes

The solution algorithm for pressure-velocity coupling used is SIMPLEC (Semi-Implicit Method for Pressure Linked Equations Consistent) scheme (Patankar, 1980). The solver used for the pressure is the standard OpenFOAM multigrid GAMG with Gauss-Seidel smoother. The solver used for the momentum and the other transport equations is a stabilized preconditioned bi-conjugate gradient, PBiCGStab (for asymmetric matrices), with preconditioner diagonal incomplete-LU DILU (asymmetric).

Tables 2.7 and 2.8 collect all the relevant information about spatial discretization schemes used in RANS computations. Obviously this is not the only possible choice. Based on our tests, the combination of schemes reported gives superior behavior for the flow conditions analyzed in the present research. Specifically an intensive campaign of numerical tests was carried out, simulating the turbulent flows at different Reynolds numbers and using a variety of strategies for the treatment of the near-wall region.

Item	**OpenFOAM discretization scheme**	**Description**	**Order of Accuracy**
∇U	cellMDLimited Gauss linear 0.5	limited central differencing	II
$\nabla \{p, k, \omega\}$	Gauss linear	central differencing	II
$\nabla \cdot (\phi, U)$	bounded Gauss linearUpwind Gauss linear	bounded second order upwind	II
$\nabla \cdot (\phi, k)$	bounded Gauss linearUpwind Gauss linear	bounded second order upwind	II
$\nabla \cdot (\phi, \omega)$	bounded Gauss upwind	bounded upwind	I
$\nabla \cdot \nu(\nabla U)^T$	Gauss linear	unbounded central differencing	II
∇^2	Gauss linear limited corrected 0.5	limited central differencing	II

Table 2.7: Discretization schemes wall-resolving simulation $Re_L = 1.2 \times 10^6$

Item	**OpenFOAM discretization scheme**	**Description**	**Order of Accuracy**
∇U	cellLimited Gauss linear 0.5	limited central differencing	II
$\nabla \{p, k, \omega\}$	Gauss linear	central differencing	II
$\nabla \cdot (\phi, U)$	bounded Gauss linearUpwind cellLimited Gauss linear 0.5	bounded second order upwind	II
$\nabla \cdot (\phi, k)$	bounded Gauss linearUpwind cellLimited Gauss linear 0.5	bounded second order upwind	II
$\nabla \cdot (\phi, \varepsilon)$	bounded Gauss upwind	bounded upwind	I
$\nabla \cdot \nu(\nabla U)^T$	Gauss linear	unbounded central differencing	II
∇^2	Gauss linear limited corrected 0.5	limited central differencing	II

Table 2.8: Discretization schemes wall-modeled simulation $Re_L = 1.2 \times 10^6$

Initial conditions were assigned as follow:

- $U = -3\,\frac{m}{s}$, mean velocity field
- p=0 $\frac{m^2}{s^2}$, mean kinematic pressure
- $k = \frac{3}{2}(I\,u_{ref})^2 = 0.00135\,\frac{m^2}{s^2}$, turbulent kinetic energy (with I the turbulence intensity)
- $\omega = \frac{k}{\nu}\left(\frac{\nu_t}{\nu}\right)^{-1} \approx 150\,s^{-1}$, specific dissipation rate (with ν the fluid viscosity and ν_t the eddy-viscosity)
- $\varepsilon = C_\mu\,\frac{k^2}{\nu}\left(\frac{\nu_t}{\nu}\right)^{-1} \approx 0.015\,\frac{m^2}{s^3}$, rate of dissipation of turbulent kinetic energy

The boundary conditions are listed in the following table 2.9, grouped by patches. With **sub-walls** we intend the solid boundaries of the submarine: hull, sail, sail plane, rudders.

	Inlet	**Outlet**	**Sub-walls WR**	**Sub-walls WF**
$U\ \left[\frac{m}{s}\right]$	-3	zero gradient	noSlip	noSlip
$p\ \left[\frac{m^2}{s^2}\right]$	zero gradient	0	zero gradient	zero gradient
$k\ \left[\frac{m^2}{s^2}\right]$	0.00135	zero gradient	0	kqRWallFunction
$\omega\ [s^{-1}]$	150	zero gradient	omegaWallFunction	-
$\varepsilon\ \left[\frac{m^2}{s^3}\right]$	0.15	zero gradient	-	epsilonWallFunction
$\nu_t\ \left[\frac{m^2}{s}\right]$	calculated	calculated	0	nutUSpaldingWallFunction

Table 2.9: Boundary conditions RANS simulations $Re_L = 1.2 \times 10^6$

Item	**Wall-resolved**	**Wall-modeled**	**Δ%**
$-X'_p \times 10^3$	0.208	0.226	8.65
$-X'_f \times 10^3$	0.894	0.987	10.40
$-X' \times 10^3$	1.102	1.213	10.07
$Z' \times 10^3$	0.054	0.048	10.04
$-M' \times 10^4$	0.420	0.416	-0.80

Table 2.10: Forces and moments for the RANS simulations at $Re_L = 1.2 \times 10^6$

2.3.2 Residuals, forces and moments

The following analysis, which has analogous structure of the other already presented in the previous section 2.2, starts with the plot of the residuals history during the computation.

Figures 2.20 (a) and (b) show the residuals for simulations WR and WM. The behavior is similar. Pressure residuals drop about three orders of magnitude (while at Reynolds 9.57×10^6 the pressure drops by four orders, see section 2.2.2 for comparison). The residuals of the three momentum equations and of the two turbulence model equations dropped by more than five orders of magnitude.

Table 2.10 shows dimensionless forces and moments calculated in the two cases. The difference in the streamwise and vertical force calculated between the WR and the WM approaches is about 10 %. In the next sections the results obtained using different grids will be analyzed and compared to.

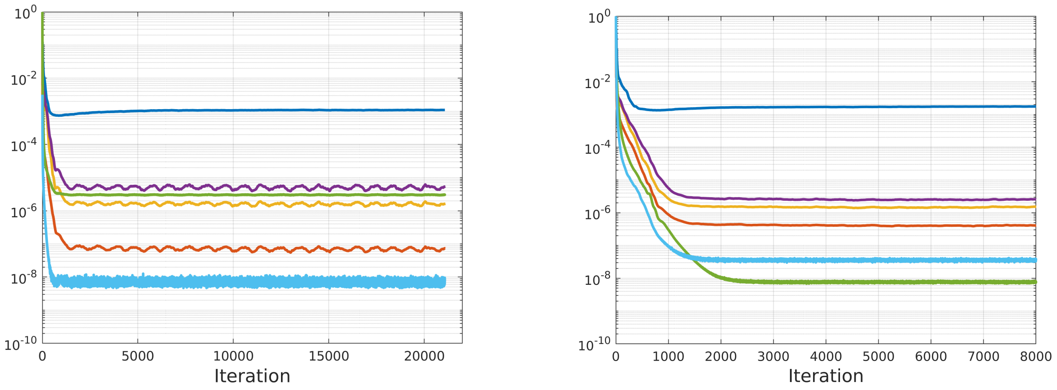

(a) Wall-resolved approach

(b) Wall-modeled approach

Figure 2.20: Linear solver residuals: p (—), U_x (—), U_y (—), U_z (—), k (—), ω-(a) and ε-(b) (—)

2.3.3 Hull

The analysis of the contour plots of y^+ over the submarine surfaces indicates that the grid is well designed for our purposes: in the case of wall-resolving simulation, y^+ is below unity, while when using the continuous Spalding's wall function, y^+ is about 50 and uniform over the hull. y^+ gives also information about the wall-shear stress: in figure 2.21 (b), placed between the bow and the sail, y^+ locally decreases. The wall-adjacent cells of the grid have all uniform height, and so, as we will see in more details soon, this drop is caused by a local underestimation of the modeled wall-shear stress.

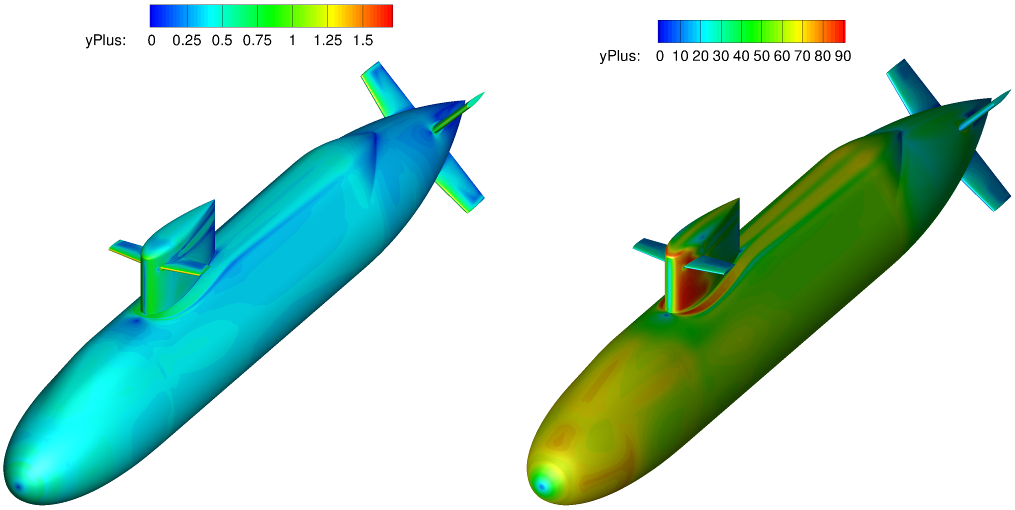

(a) Wall-resolved approach (b) Wall-modeled approach

Figure 2.21: y^+ contours on submarine's hull

Contours of pressure coefficient over the submarine surface show a qualitatively good agreement between the two approaches (figure 2.22). This agreement for pressure was found for all the meshes used and holds for the values of Reynolds number herein considered.

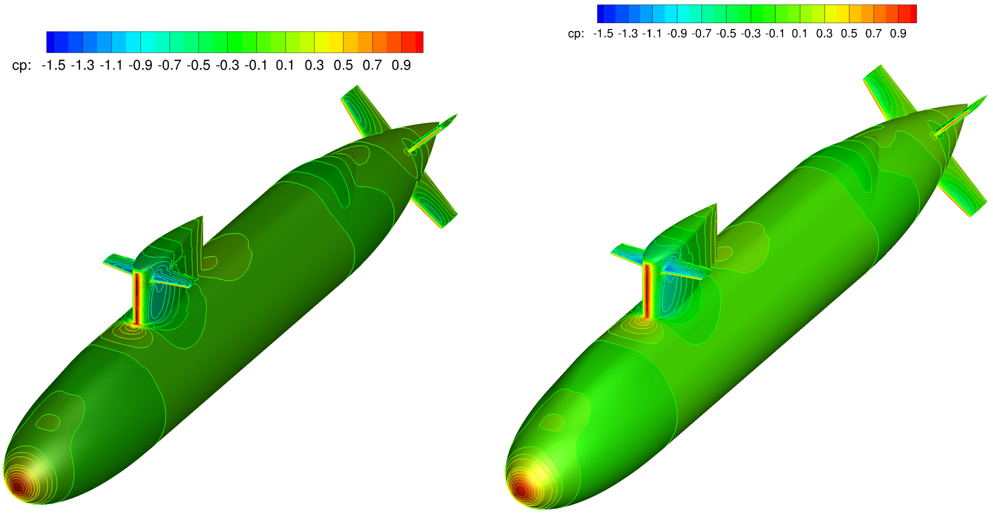

(a) Wall-resolved approach (b) Wall-modeled approach

Figure 2.22: Pressure coefficient C_p contours on submarine's hull

Differently from the pressure coefficient, the modeled dimensionless wall-shear stress magnitude is strongly affected by the Reynolds number of the flow. At $Re_L = 9.57 \times 10^6$ the agreement between the wall-resolved results and the wall-modeled was rather satisfactory. For the author's understanding this can be a result of the different physic to be reproduced (C_f depends on Reynolds) and, might be even more important, by the statistical arguments on which rely the hypothesis behind turbulence modeling and wall-layer models. We also noticed that at high-Re number the results are not sensitive to the numerical schemes selected for the simulation. Figure 2.23 shows that, in this particular case, the wall-layer model is not able to capture τ accurately. As already mentioned when describing figure 2.21, between the bow and the sail, in the case "wall-modeled", τ locally decreases. This behavior is not in compliance with that we calculated when solving the boundary layer, and which we consider to be more accurate. At the sail, the maximum wall-shear stress is as lower as about 50% that calculated without wall-layer model.

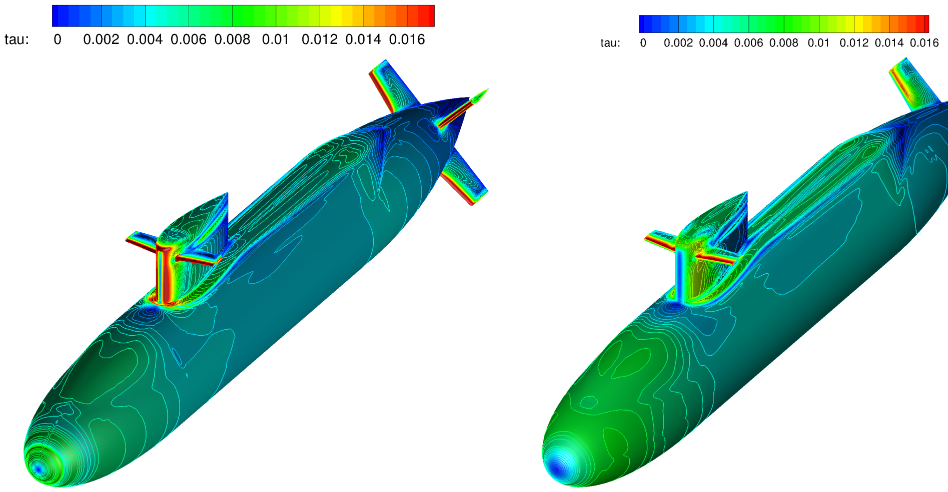

(a) Wall-resolved approach (b) Wall-modeled approach

Figure 2.23: Contours of non-dimensional wall-shear stress on the submarine's hull

2.3.4 Behind sail plane

Figure 2.24 shows the contours of the non-dimensional axial velocity u for the WR and WM results. As it can be observed, the wall treatment affects the development of the wake. In figure 2.24(b) for y/L=0 and $0.1 \leq z/L \leq 0.13$, the wake estimated with the WM approach is wider that that obtained with WR.

Figures 2.25 and 2.26 show contours of the turbulent kinetic energy (TKE) k and x-vorticity ω_x at plane W. TKE levels in the turbulent boundary layer are in good agreement between WR and WM approaches. The flow behind the sail is affected by the wall-approach chosen. In particular, the sail wake in figure 2.25(b) is characterized by slight higher values of turbulent kinetic energy compared to the wall-resolved, at $Y/L \approx 0$.

Figure 2.26 shows contours of ω_x. The number of vortical structures predicted by the two models are different. In the case of wall-resolved simulation 3 couples of vortices are generated by the sail whereas, when using wall-functions, the model predicts 4 couples of vortices. Vortices number 1, 2 and 3 of figure (a) and figure (b) match in position. Considering the case WR, vortices 2 and 3 are characterized

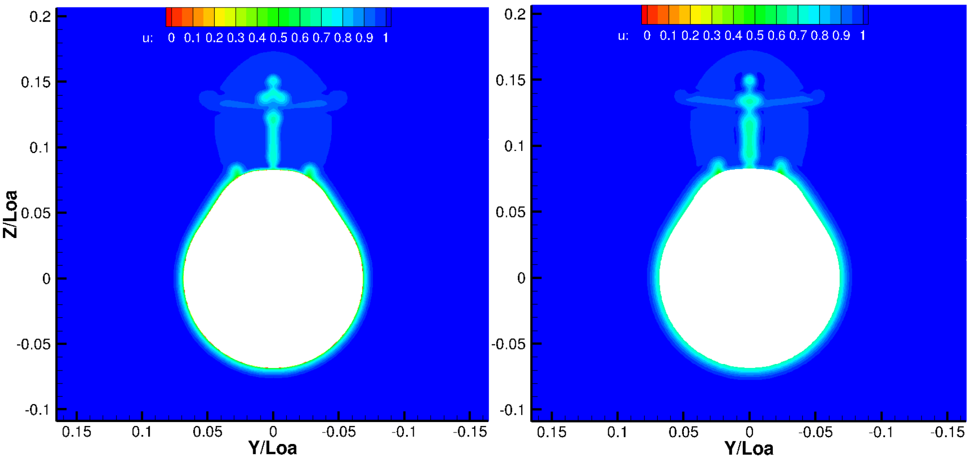

(a) Wall-resolved approach (b) Wall-modeled approach

Figure 2.24: Contours of streamwise velocity u at plane W

by an ω_x with negative and positive sign, respectively. The simulation with wall-functions, instead, predicts ω_x of vortex number 2 to be positive, whereas the vortex number 3 has negative sign.

2.3.5 Propeller plane

At behind sail plane W, we noticed few differences between the two approaches of simulations. In the propeller plane P, these differences persist, especially for the sail wake. Figure 2.29 shows the contours of velocity u. The traces of the "X" rudders and of the stern are superimposed to the trace of the sail. The vortical structures generated behind the sail are dissipated within about $0.3L$ (see also figures 2.30 (e) and (f)).

2.3.6 Transverse plane

Looking at the transverse plane helps to summarize what we stated during the analysis of the other two planes W and P. Qualitatively the sail wakes predicted by the two methodologies appear to be not very similar to each other. In the "wall-

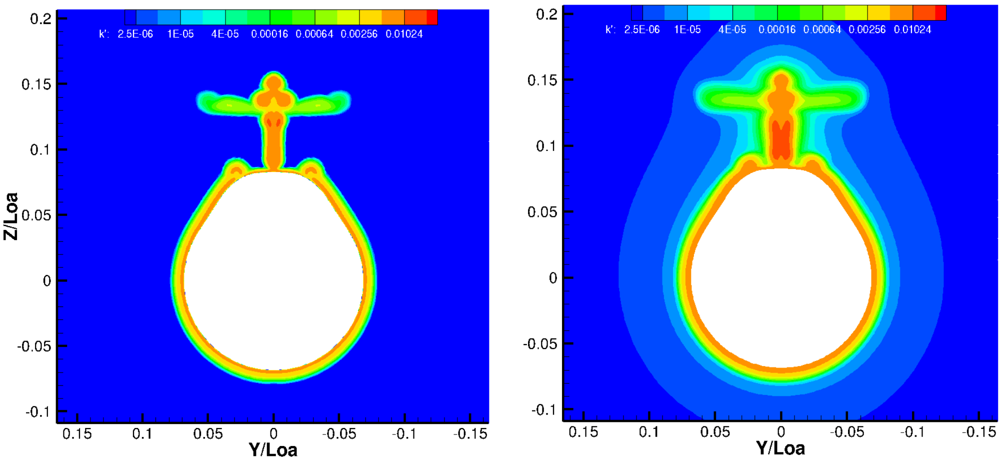

(a) Wall-resolved approach (b) Wall-modeled approach

Figure 2.25: Contours of turbulent kinetic energy k at plane W

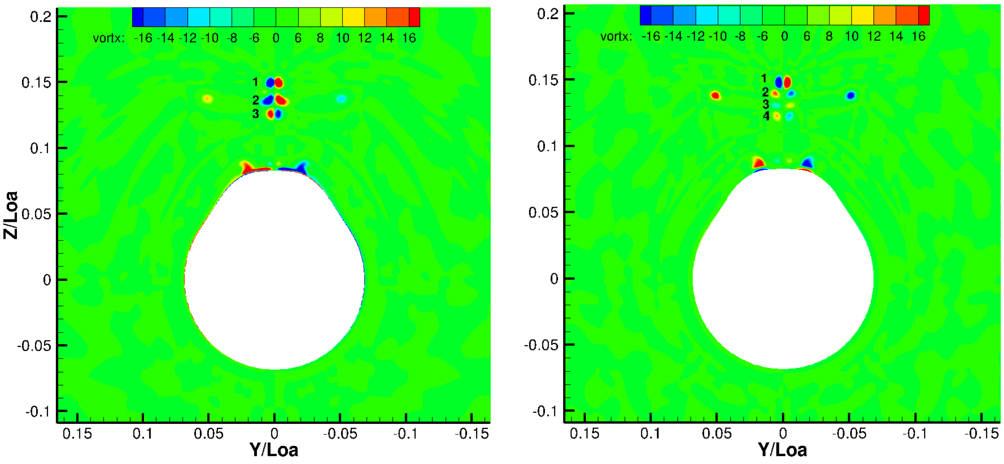

(a) Wall-resolved approach (b) Wall-modeled approach

Figure 2.26: Contours of x-vorticity ω_x at plane W

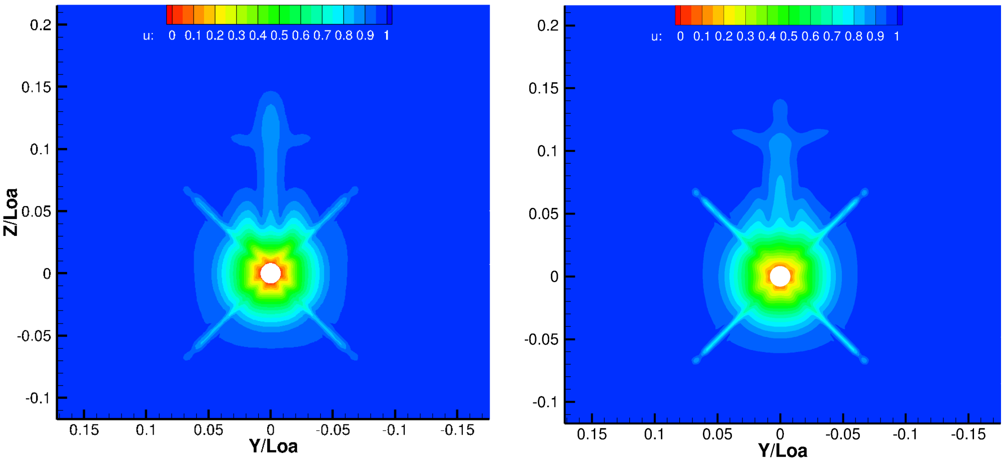

(a) Wall-resolved approach (b) Wall-modeled approach

Figure 2.27: Contours of streamwise velocity u at plane P

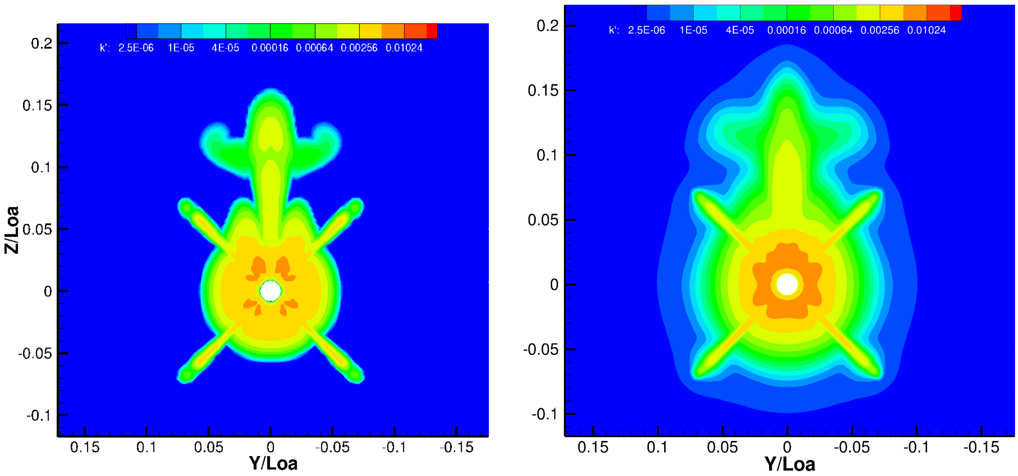

(a) Wall-resolved approach (b) Wall-modeled approach

Figure 2.28: Contours of turbulent kinetic energy k at plane P

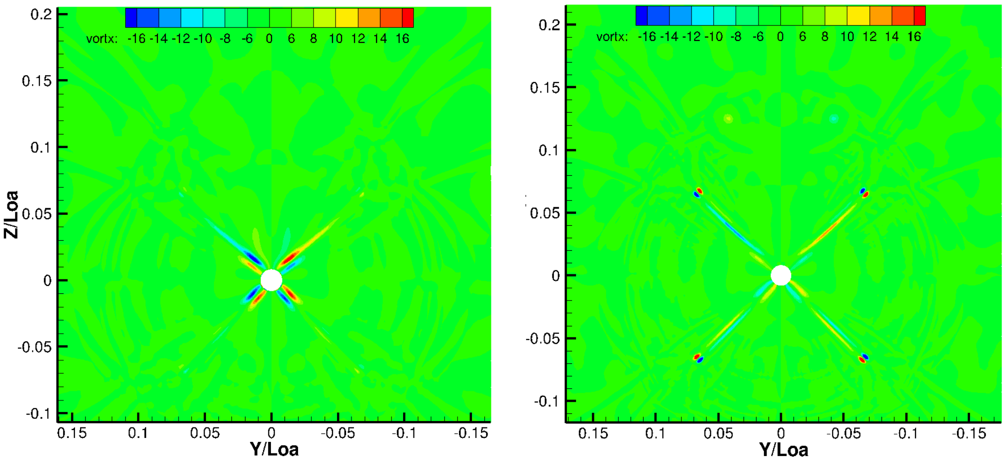

(a) Wall-resolved approach

(b) Wall-modeled approach

Figure 2.29: Contours of x-vorticity ω_x at plane P

resolved" case the sail wake is characterized by an homogeneous zone $x/L \leq 0.57$, figure 2.30 (a), which propagates downstream. On the other hand, using wall-layer models we observe that the wake is constituted by two main structures: the first, more intense, close to the hull, and the second at the sail tip. They propagates downstream separately.

The turbulence kinetic energy in the wake is higher if calculated using wall models especially behind the sail. Numerical diffusivity on the solution with wall-function is probably due to limiters on gradients in the solutions of the convective term of the model equation of the turbulent kinetic energy.

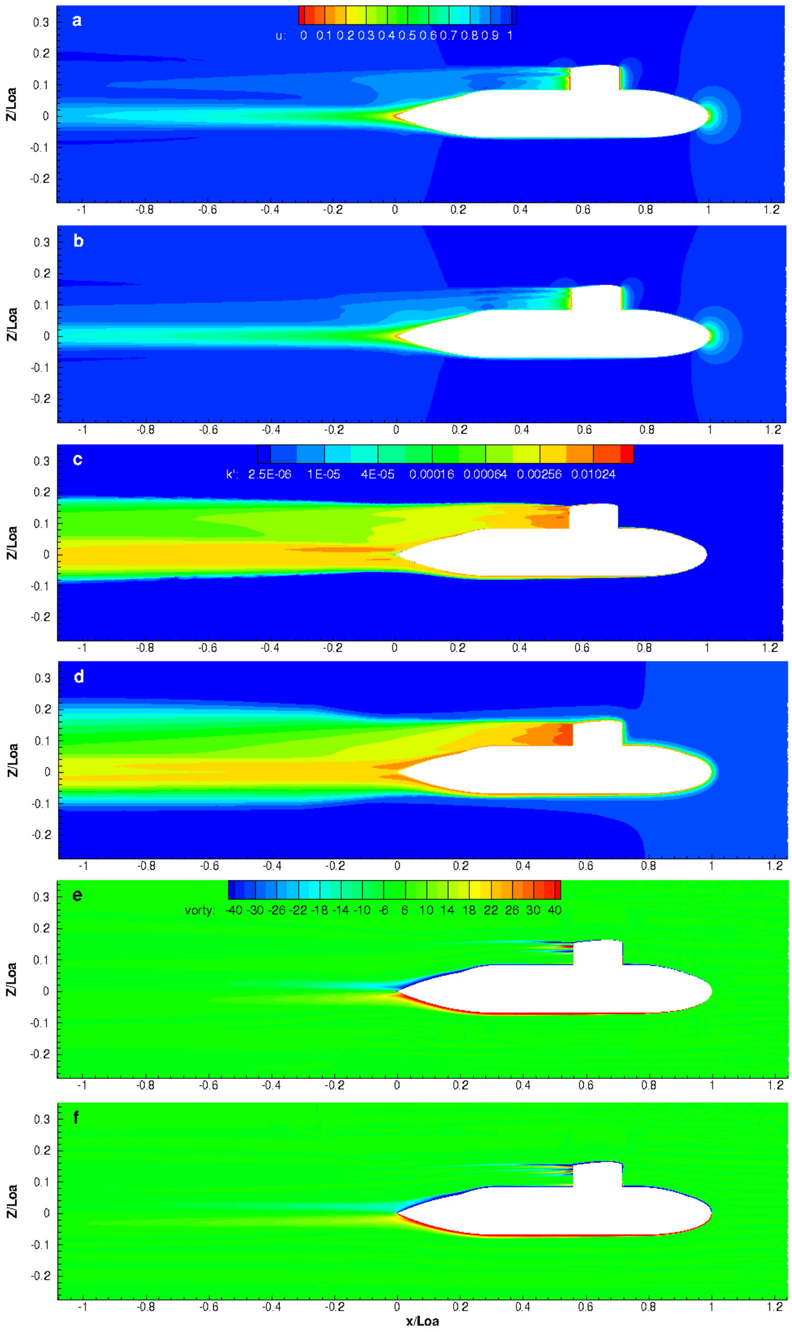

Figure 2.30: Contours of u, k and ω_y at plane Y. Figures a, c and e: wall-resolving simulation. Figures b, d and f: wall-modeled simulation.

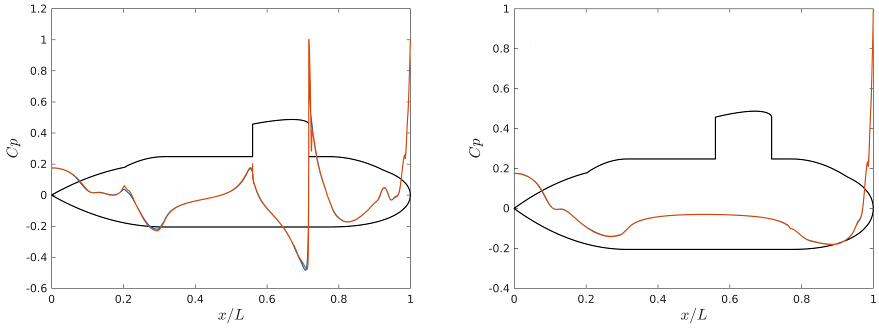

(a) cp along top side, z >0

(b) cp along bottom side z <0

Figure 2.31: Pressure coefficient along the y=0 curve: WR-RANS (—); WM-RANS (—)

2.3.7 Slices

Figure 2.31 shows the analysis of the pressure coefficient plot on the line intersection between the submarine surface and the transverse plane. The agreement is excellent. In figure 2.31 (a), starting from the bow at x/L=1 the solution using wall-layer model follows very well the solution obtained solving the viscous sublayer up to the wall, until x/L=0.8. For x/L=0.77, the blue curve predicts a drop of the order of 10^{-2}, then it starts to increase again with higher slope compared to the WR simulation. On the intersection line between the plane y=0 and the submarine surface, for negative values of z, the two solutions are very close to each other with exception for a small pressure drop predicted using wall-layer model, again at $x/L \approx$0.8, where the pressure gradient turns adverse. The analysis of C_f at $Re_L = 1.2 \times 10^6$ reveals that the solution obtained with wall-layer model moves away from the one WR. In figures 2.32 we observe that in presence of the junctions and sharp shapes, there is an important mismatch between the two solutions. At this value of Reynolds number relaminarization of the flow might occur making the use of wall-layer model ineffective. This is shown in figure 2.33, for $0.8 < x/L < 1$. In the range $0.3 < x/L < 0.8$ there is an unexpected mismatch between the C_f predicted by the two simulations in the cylindrical region of the hull, where the log-law is supposed to work well. The reason of this behavior is that the wall-functions are tough for “very-high” Reynolds number

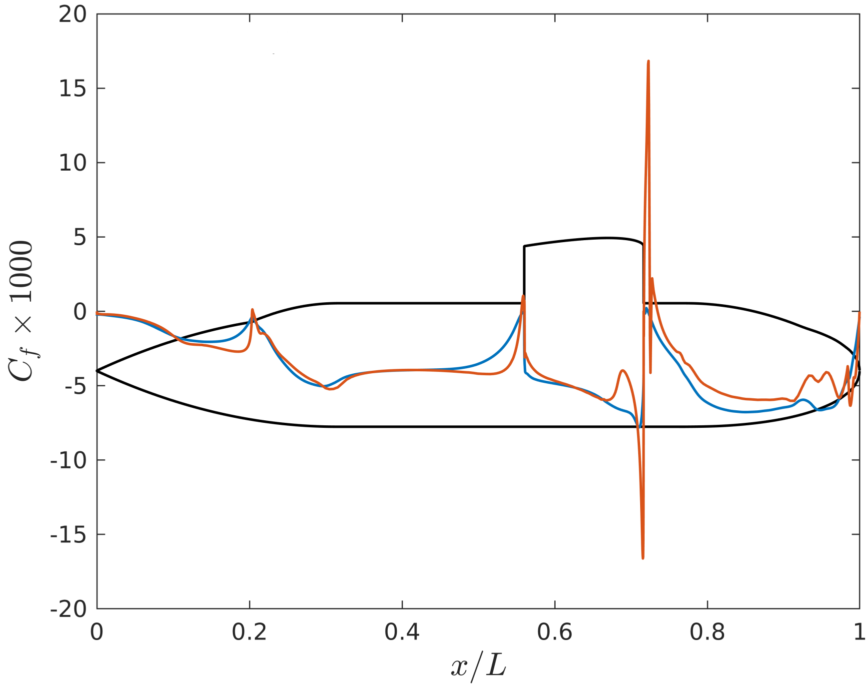

Figure 2.32: Skin-friction C_f coefficient along the $y = 0$ curve, top side of the hull: WR-RANS (🟧); WM-RANS (🟦)

flows (in fact at $Re_L = 9.57 \times 10^6$ we did not faced such problems). Figure 2.34 shows the eddy-viscosity ν_t against the wall distance in wall units y^+, for the simulations at $Re_L = 9.57 \times 10^6$ and $Re_L = 1.2 \times 10^6$, and for WR and WM approaches; ν_t data are extracted from a line at $x/L = 0.5$, $z < 0$ and lying on the symmetry plane. Figure 2.34 (b) shows that, at $Re_L = 1.2 \times 10^6$, the wall model predicts too high eddy-viscosity and this lead to overestimate Cf, because $u_\tau^2 = (\nu + \nu_t)\,(dU/dy)$ $(dU/dy$ indicates the velocity gradient in wall-normal direction). At $Re_L = 9.57 \times 10^6$ the eddy-viscosity predicted by the wall model is in good agreement with that predicted with a WR computation, as shown in Figure 2.34 (a).

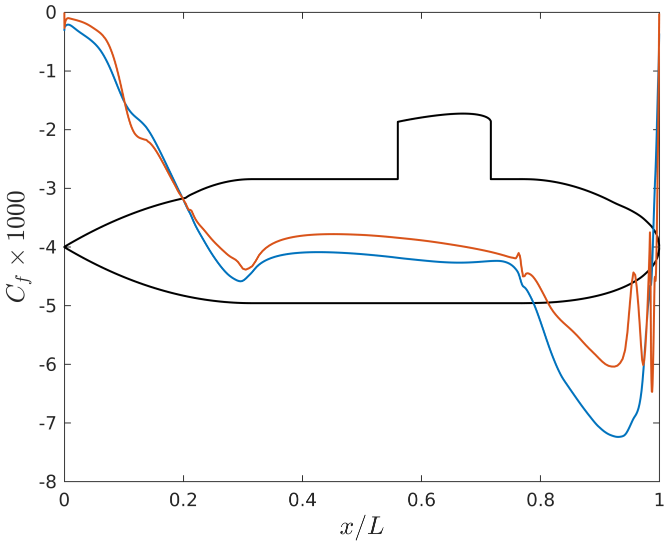

Figure 2.33: Skin-friction C_f coefficient along the $y = 0$, $z \leq 0$ curve: WR-RANS (—); WM-RANS (—)

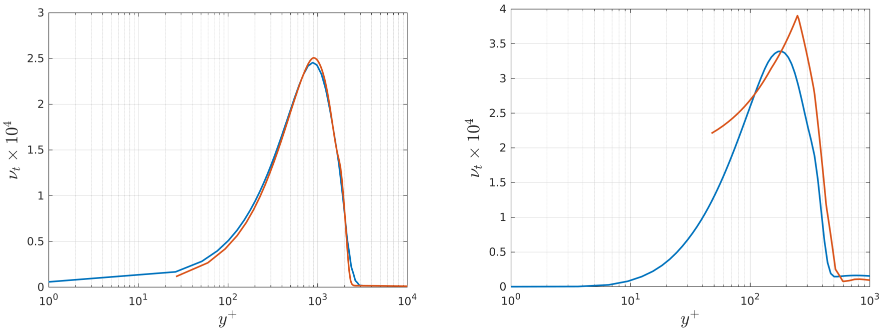

(a)

(b)

Figure 2.34: ν_t vs y^+ at (a) $Re_L = 9.57 \times 10^6$ and (b) $Re_L = 1.2 \times 10^6$. WR-RANS (—); WM-RANS (—)

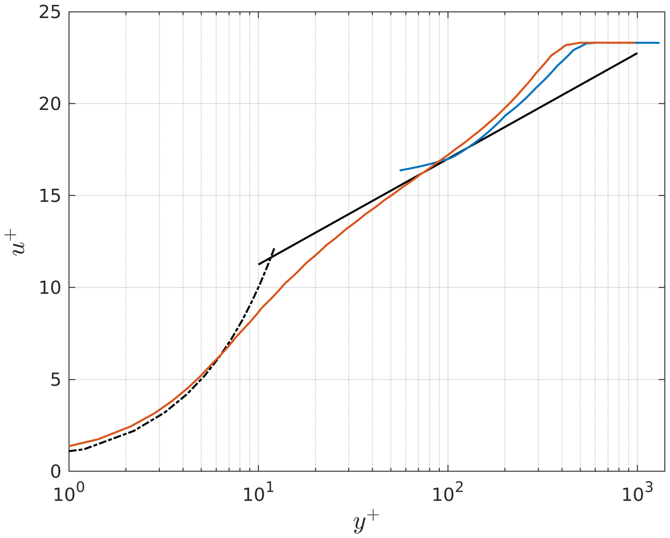

Figure 2.35: The law of the wall, bottom side of the hull: WR-RANS (—), WM-RANS (—), $u^+ = y^+$ (- - -), the log-law $u^+ = 2.44 \log(y^+) + 5.2$ (—)

2.3.8 The law of the wall

Following the discussion of in subsection 2.2.9, the bottom side of the hull is characterized by a zero gradient pressure coefficient for a long extension and the hull is cylindrical. Differently from the other case, the Reynolds number in this case is lower (at Reynolds number 9.57×10^6) making questionable the validity of the wall-layer model based on the log-law velocity profile. As we said, the logarithmic behavior extends from a minimum value of y^+=30-50, to a maximum of 0.2δ. The boundary-layer thickness for a zero-pressure gradient turbulent flat plate flow can be approximated as

$$\delta \approx \frac{0.37\,x}{{Re_x}^{1/5}} \tag{2.2}$$

with x the distance downstream from the start of the boundary layer. In this case the log-law can be considered valid just until y^+=80. This is shown in figure 2.35.

3

LES of the BB2 submarine

3.1 Overview

In this chapter we show and discuss results of Large-Eddy Simulations (LES) of the fully appended BB2 submarine at Reynolds number of 1.2×10^6. The computational grid has a topology similar to those used in RANS (see chapter 2), although modifications have been done in order to make the grid suitable for LES. In particular, the resolution has been increased in the wake and the mesh around the submarine has been modified with the aim to reduce the aspect ratio of the cells on the hull surface. This leads to an increase of the number of cells up to $\approx$ 40 millions.

We adopt the sub-filter scale model is the Wall-Adapting Local Eddy-viscosity (WALE), Nicoud & Ducros (1999), already presented in subsection 1.4.9. This model has been proved to be as accurate as the dynamic Lagrangian model, or the dynamic Smagorinsky model, at a lower computational cost. In the recent works of Posa & Balaras (2016, 2020), the WALE model has also been applied with success to hydrodynamic applications.

To reduce the required computational efforts, wall-functions are used to model the near-wall behavior. The first cell's height should be set to give a y^+ value of $30 \leq y^+ \leq 60$ (with y^+ we intend the wall-normal coordinate using inner scaling). In LES, the discretization along the tangential directions on the surface should assume values of the order of hundreds wall units. In this particular case, the resolution in streamwise direction on the cylindrical part of the hull ($0.25 \leq x/L \leq 0.75$) is Δx^+=100, while in circumferential direction it is $\Delta \theta^+$=100. These values are the result of a compromise between the need of near-wall cells as big as possible with respect to the statistical assumption of the log-law, and the need of cells small enough to furnish a detailed description of the submarine geometry. Using unstructured grids one could avoid this kind of trade off, at the price of working with a grid of inferior quality. It is important to highlight that OpenFOAM treats all grids as unstructured, no matter the way they were built up. The Spalding's wall-function is employed for wall-layer modeling. This formulation is particularly useful when dealing with complex geometries, where it is not possible to guarantee $y^+ > 50$ everywhere at solid boundaries.

$$y^+ = u^+ + e^{-B\kappa}\left[e^{\kappa\, u^+} - 1 - \kappa u^+ - \frac{\left(\kappa\, u^+\right)^2}{2!} - \frac{\left(\kappa\, u^+\right)^3}{3!} - \frac{\left(\kappa\, u^+\right)^4}{4!}\right] \tag{3.1}$$

3.2 LES grid

As already anticipated in section 3.1, the LES grid used is similar in topology to the one used for the RANS simulations. The wake blocks has been changed in order to increase the resolution and to use a grid as much uniform as possible. This is shown in figure 3.1(a) where the wake blocks connectors are colored in red. Also, the distribution of the cells on the submarine surface has been modified to reduce the elongation in streamwise direction, that is typical of RANS-grids. As it can be seen, the cells on the surface assume a quadratic shape (cubical considering also the wall normal direction), typical of a WM-LES computation. A detail of the surface mesh on the hull and the boundary layer block is shown in figure 3.1(b).

The overall grid quality is excellent. Table 3.1 reports the grid quality measured with different criteria.

3.3 Solver and numerical schemes

The solution algorithm for pressure-velocity coupling is a customized Pressure-Implicit with Splitting of Operators (PISO) scheme (Issa *et al.*, 1986), with 2 corrections loop and one extra loop for non-orthogonality. The solver used for the pressure

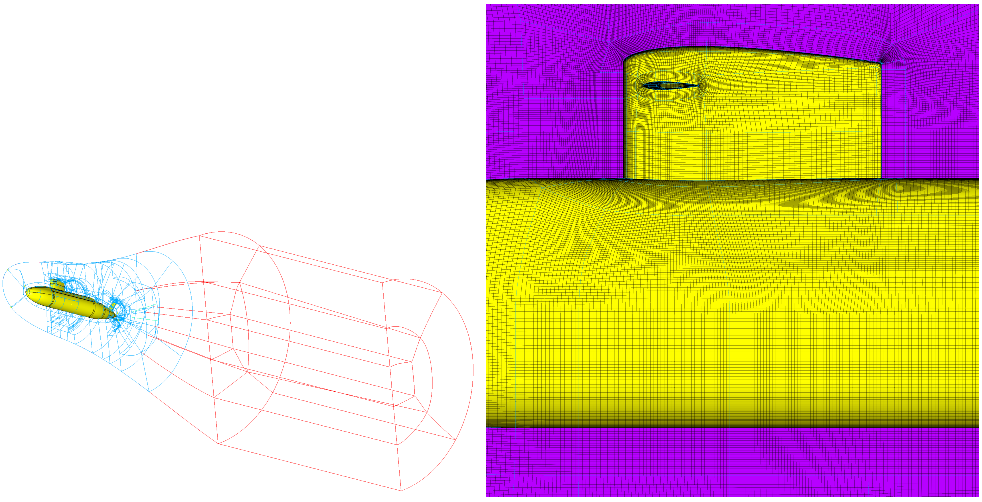

(a) Grid topology in the wake

(b) Zoom-in of surface mesh on the hull and the boundary layer blocks

Figure 3.1: LES grid details

is the standard OpenFOAM iterative PCG together with FDIC preconditioner. The solver used for the velocity is the PBiCG, with DILU preconditioner.

Table 3.2 collects the relevant information about spatial discretization schemes used in LES. In order to improve the stability, especially at the interface between tetrahedral and hexahedral grid elements, the LUST scheme has been adopted. It is a blend between linear (75 %) and second order upwind (25 %).

Item	Discretization	Type	Accuracy Order
$\nabla \bar{U}$	Gauss cellMDLimited Gauss Linear 1	limited central differencing	II
$\nabla \bar{p}$	Gauss linear	central differencing	II
$\nabla \cdot (\phi, \bar{U})$	Gauss LUST	blend 75% linear and 25% 2nd order upwind	II
$\nabla \cdot \bullet$	Gauss linear	central differencing	II
$\nabla \cdot \nu (\nabla \bar{U})^T$	Gauss linear	unbounded central differencing	II
∇^2	Gauss linear corrected	unbounded central differencing	II

Table 3.2: LES discretization schemes

Quality criteria	**Value**
Max cell-openess	10^{-15}
Max aspect-ratio	52
Min volume	10^{-12}
Max non-orthogonality	74.57
Average non-orthogonality	15
Max-skewness	2.22

Table 3.1: LES grid quality check

3.4 Initial and boundary conditions

As initial condition we use the steady-state RANS solution at $Re_L = 1.2 \times 10^6$ (discussed in section 2.3). The enforced boundary conditions on physical and computational boundaries are listed in table 3.3, grouped in patches. With **sub-walls** we intend all the solid boundaries of the submarine, i.e. hull, sail, sail plane, rudders. A zero-gradient condition was applied to the physic variables at top, bottom, and the two lateral patches of the computational domain.

		Inlet	**Outlet**	**Sub-walls**
$\bar{U}$	$\left[\frac{m}{s}\right]$	-3	zero-gradient	noSlip
$\bar{p}$	$\left[\frac{m^2}{s^2}\right]$	zero-gradient	0	zero gradient
ν_t	$\left[\frac{m^2}{s}\right]$	calculated	calculated	nutUSpaldingWallFunction

Table 3.3: LES boundary conditions

The time step is $1.57 \times 10^{-4}\, t_c$ (with $t_c = \frac{tU_\infty}{L}$) and guarantees CFL number always below 0.5. Figure 3.2 (a) shows the statistically stationary velocity signal sampled for $3t_c$. The velocity signal is sampled close to the bottom side of the hull, along the negative z-direction, for x/L=0.5 and wall-normal distance from the hull equal to 70 wall-units. Figure 3.2 (b) shows the energy spectrum E_{uu}, calculated from the product of the streamwise velocity fluctuations. The spectrum presents the -5/3 Kolmogorov's slope in the inertial subrange and does not show energy pile-up neither cuts at the high-frequencies.

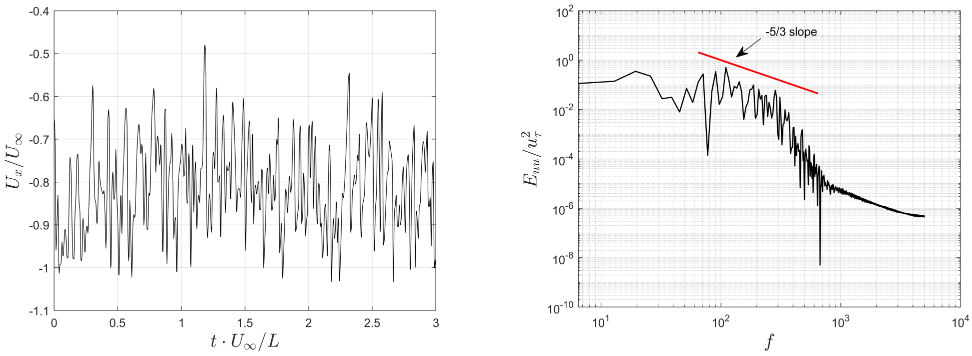

(a) (b)

Figure 3.2: (a) Time-signal of the resolved streamwise velocity at x/L=0.5, y/L=0 and distance from the bottom side of the hull in negative z-direction of 70 wall-units. (b) Uni-dimensional velocity spectrum

3.4.1 Numerical tripping

The velocity at the inlet patch is uniform and equal to U_∞ (see table 3.3). This uniform velocity field reaches the bow of the submarine, determining a stagnation point. Moving downward, the flow tends to remain laminar. To stimulate the transition to turbulence, it is necessary to force the flow with some fictitious disturbances. This is analogous to the methodology employed in laboratory experiments, where transition is forced by placing pins on the hull of the ship model, at the position where it is expected to occur. In our study the pins are replaced by a random volume forces, with zero mean value, applied over a small portion of the computational domain. Figure 3.3 shows the trace of the tripping loads on the submarine's surface

$(0.9 \leq x/L \leq 0.925)$. In this case the transition switches on at x/L≈0.84. The body forces are generated at every step of the PISO loop, based on the resolved LES velocity, on the mean RANS velocity and on the amount of turbulent kinetic energy (both computed in the precursor RANS, which becomes part of the model). This ”tripping” procedure has been developed some years ago at university of Trieste, in collaboration with the university’s spin-off *IE-Fluids*, in order to prescribe a turbulent inlet boundary condition. For the present application few modifications to the original version have been done, to change its nature from synthetic turbulence at inflow to a localized tripping.

In OpenFOAM it is possible to mark a set of cells, obeying a certain mathematical condition, using the native function ”funkySetFields”. Doing that, it is possible to select the portion (volumetric) of the computational domain interested by the tripping.

Looking at the LES equation 3.2, we add a body force term in the momentum equation, restricted to $\Omega_1 \subset \Omega$, where Ω represents the entire domain. It means that if $\mathbf{x} \in \Omega_1$, the momentum equation to be solved is:

$$\frac{\partial \bar{U}_i}{\partial t} + \frac{\partial}{\partial x_j}(\bar{U}_i \bar{U}_j) = -\frac{1}{\rho}\frac{\partial \bar{p}}{\partial x_i} + \frac{1}{\rho}\frac{\partial \tau^R_{ij}}{\partial x_i} + \nu \nabla^2 \bar{U}_i + f_i \tag{3.2}$$

Otherwise, when $\mathbf{x} \in \Omega \setminus \Omega_1$, the momentum equation to solve is the equation 1.23. Subdomain Ω_1 has cylindrical shape with radius 2D and height equal to 0.025L. Its symmetry axis is co-axial with that of the submarine.

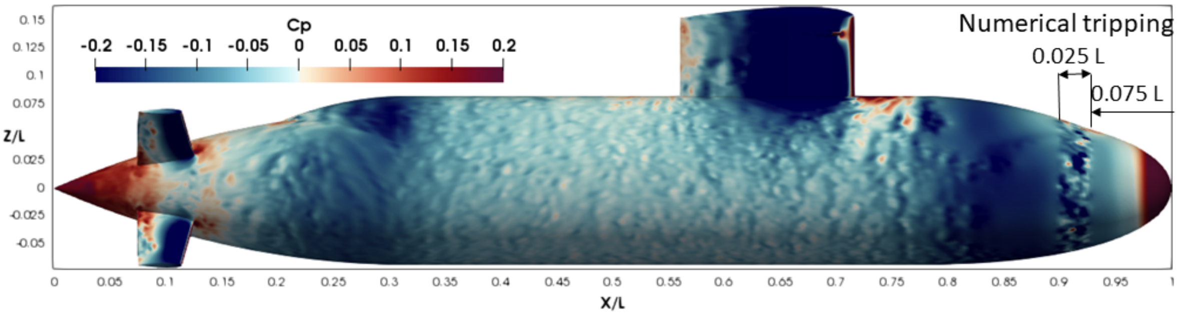

Figure 3.3: Body forces of the numerical tripping acting on the submarine surface

3.5 Pressure and skin-friction coefficients

Figure 3.4 shows the mean pressure coefficient over the submarine's surface. Statistics have been computed with data sampled oveer the solid surfaces over $9\,t_c$. The pressure coefficient of figure 3.4 (a) is in qualitatively good agreement with the solution obtained using RANS (see figures 2.22 (a) and (b)).

Figure 3.5 (a) shows the time-averaged pressure coefficient over the intersection curve between the submarine and the semi-plane $z \leq 0$, with normal vector oriented as y-axes direction and passing through the origin of the coordinate system. Comparison is carried out with RANS results, both in wall-resolved case and wall-modeled one, and with experimental data by Huang *et al.* (1992) for DARPA submarine. Experiments were conducted at Re$=12 \times 10^6$ and here rescaled, based on the Reynolds numbers ratio (Posa & Balaras, 2016). On the central region, $0.3 < x/L < 0.7$, all the numerical and experimental data are in a rather good agreement. DARPA's data move away at the bow and at the stern, probably due to the geometry differences between DARPA and the BB2.

Figure 3.5 (b) shows the skin-friction coefficient C_f on the same location of the C_p. The comparison is made again between WM-LES, the scaled experimental data by Huang *et al.* (1992) and Anderson *et al.* (2012) and the two RANS (WR and WM). WM-LES dramatically underestimates C_f. The WR-RANS shows rather good agreement with experiments. RANS with wall-model overestimates C_f in the central region of the hull (as we already discussed in chapter 2). It has to be highlighted that, since we are focused on the hydroacoustics of the submarine, our interest is not on the flow field close to the wall, rather on the flow field outside the boundary layer and in the wake. With this focus, WM-LES simulations are one of the most suitable approaches; to be noted that Ianniello *et al.* (2013) discusses the inadequacy of unsteady RANS methodology to characterize the hydro-acoustic signature of a body. Indeed, as it will be shown later (section 3.7), the WM-LES estimation of the flow field in the wake it is in rather good agreement with available experimental data, theory and WR-LES predictions by other authors.

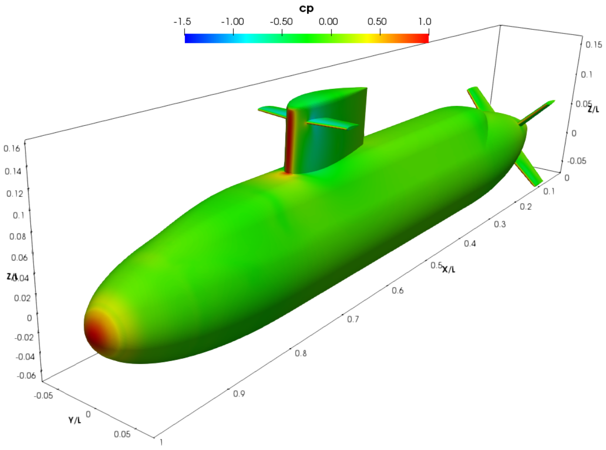

Figure 3.4: Time-averaged pressure coefficient over the BB2 submarine

3.6 The hull turbulent boundary layer (TBL)

Transition to turbulent switches on approximately at $x/L \approx 0.84$. At $x/L \approx 0.7$ the transition is complete and the boundary layer is fully developed. Figures 3.6 (a) and (b) show a cross-sectional picture of instantaneous velocity and vorticity contours, on the W-plane. Figures 3.6 (c) and (d) show the mean resolved axial velocity u and the mean resolved turbulent kinetic energy k. The W-plane is located just behind the sail, at 50% of the submarine length (see figure 2.2). Comparing the mean fields from WM-LES with those from WM-RANS (figures 2.24 and 2.25), we observe that LES estimates a higher velocity deficit. Moreover, the level of the mean turbulent kinetic energy calculated with resolved LES velocity fluctuating field is not as intense as that obtained with RANS $k-\varepsilon$ simulation.

Looking at the instantaneous velocity and vorticity contours we observe the trace of the sail and sailplane wake. The turbulent boundary surrounds the hull, depicting the characteristic eddies.

It is well know that the turbulent boundary layer is characterized by a complex dynamic (Robinson, 1991; Pope, 2000), such as:

1. Low-speed streaks in the viscous sub-layer

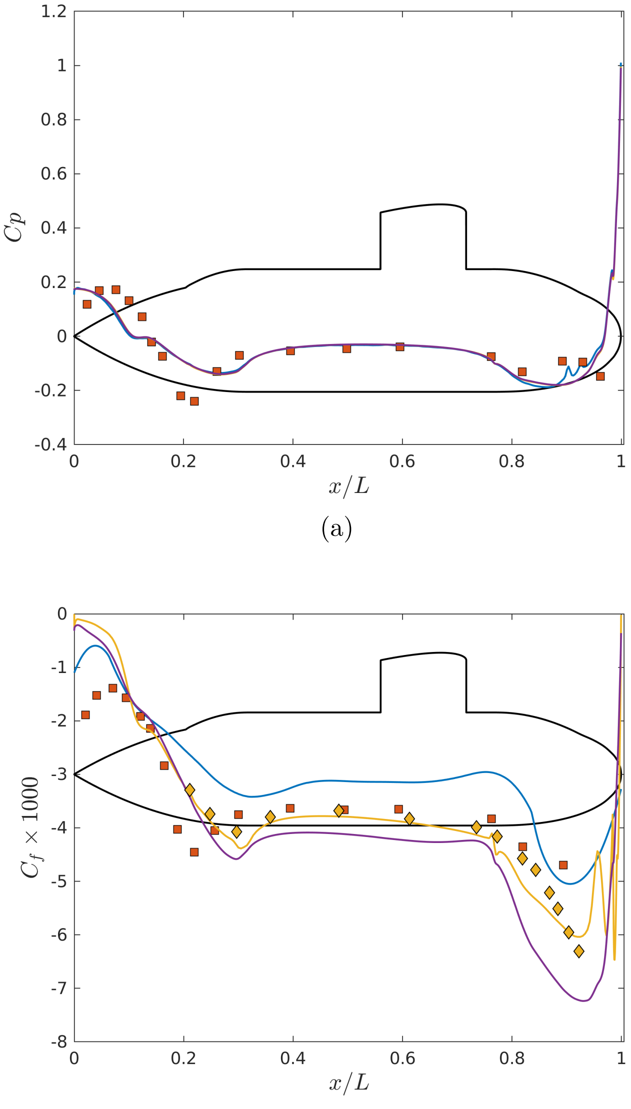

(a)

(b)

Figure 3.5: Time-averaged pressure and skin friction coefficients over the bottom side of the hull. Present LES computation (—); Experimental data over DARPA-SUBOFF at $Re_L = 12 \times 10^6$ (■) (Huang *et al.*, 1992); Experimental data over DSTO generic submarine (BB1) at $Re_L = 5.4 \times 10^6$ (◆) (Anderson *et al.*, 2012); Wall-resolved RANS $k - \omega$ SST (—) at $Re_L = 1.2 \times 10^6$; Wall-modeled RANS $k - \varepsilon$ (—) at $Re_L = 1.2 \times 10^6$; Experimental data were rescaled, based on the Reynolds numbers ratio (Posa & Balaras, 2016).

2. Ejection of low-speed fluid from the wall
3. Sweeps of high-speed fluid toward the wall
4. Vortical structures of various forms, such as horseshoes and hairpins
5. Large (δ scale) motions capped by three-dimensional bulges in the outer turbulent/potential interface
6. Shear-layer ”backs” of large-scale outer-region motions, consisting of sloping (δ scale) discontinuities in the streamwise velocity

In the present case, we are modeling a part of the boundary layer, up to $y^+ \approx 50$. This means that we can not see structures within the viscous sublayer, because the grid does not resolve them (Piomelli & Balaras, 2002). The wall-model is able to model the effect of these structures in a statistical sense; indeed, with reference to figure 3.7 (a), where the outermost part of the boundary layer is depicted, we can clearly see ejections of low-speed fluid from the wall (indicated with a blue arrow pointing upward) and sweeps of high-speed fluid toward the wall (indicated with a black arrow pointing downward; i.e. items 2 and 3 of the previous list).

In figure 3.7 (b) streamwise vorticity contours suggest the presence of large eddies or bulges. Considering that we have transition at about $0.2L$ from the bow (see figure 3.3), at $x/L = 0.4$ an estimation of the non-dimensional boundary layer thickness based on present LES simulation is δ/L=0.013 (non-dimensional boundary layer thickness from theoretical power-law is δ/L=0.012). Vorticity is distributed along areas inclined by about 20-25 degrees, in the direction of the free stream. These areas are separated by valleys of non-turbulent flow. Looking for tiny white areas in the picture, we can recognize valleys.

All these (apparently) chaotic eddies give rise to a behavior which can represented following statistic laws. In this central zone of the hull, the boundary layer can be considered similar to that developing over a zero-pressure-gradient flat plate, so that it is possible to make comparison with well-established theoretical results. Figure 3.8 (a) shows the mean axial velocity profile, made dimensionless using the friction velocity u_τ, as a function of the nondimensional distance from the wall (expressed in wall units). The data are sampled along a line at (x/L=0.5, 0, z<0). The sampling frequency is 100 Hz and the sampling period is equal to 9 t_c. The velocity is plotted using different two different values of the friction velocity: in the green dashed line it is scaled using the wall-shear stress coming from the present simulation, while in the dash-dotted blue line, it is calculated using the nominal wall-shear stress of the WR-RANS. In this way it is possible to give a measure of the log-layer mismatch (Mukha, 2018; Mukha & Liefvendahl, 2015; Larsson *et al.*, 2016; Yang *et al.*, 2017). Following the definition given by Yang *et al.* (2017), the log-layer mismatch is a chronic problem affecting WM-LES, where the modeled wall-shear stress deviates from the true one by approximately 15%. Even more evident (and may be expected) is the mismatch for the second order statistics in comparison with available data for a ZPGTBL estimated with WR-LES (Eitel-Amor *et al.*, 2014), as shown in figure 3.8 (b).

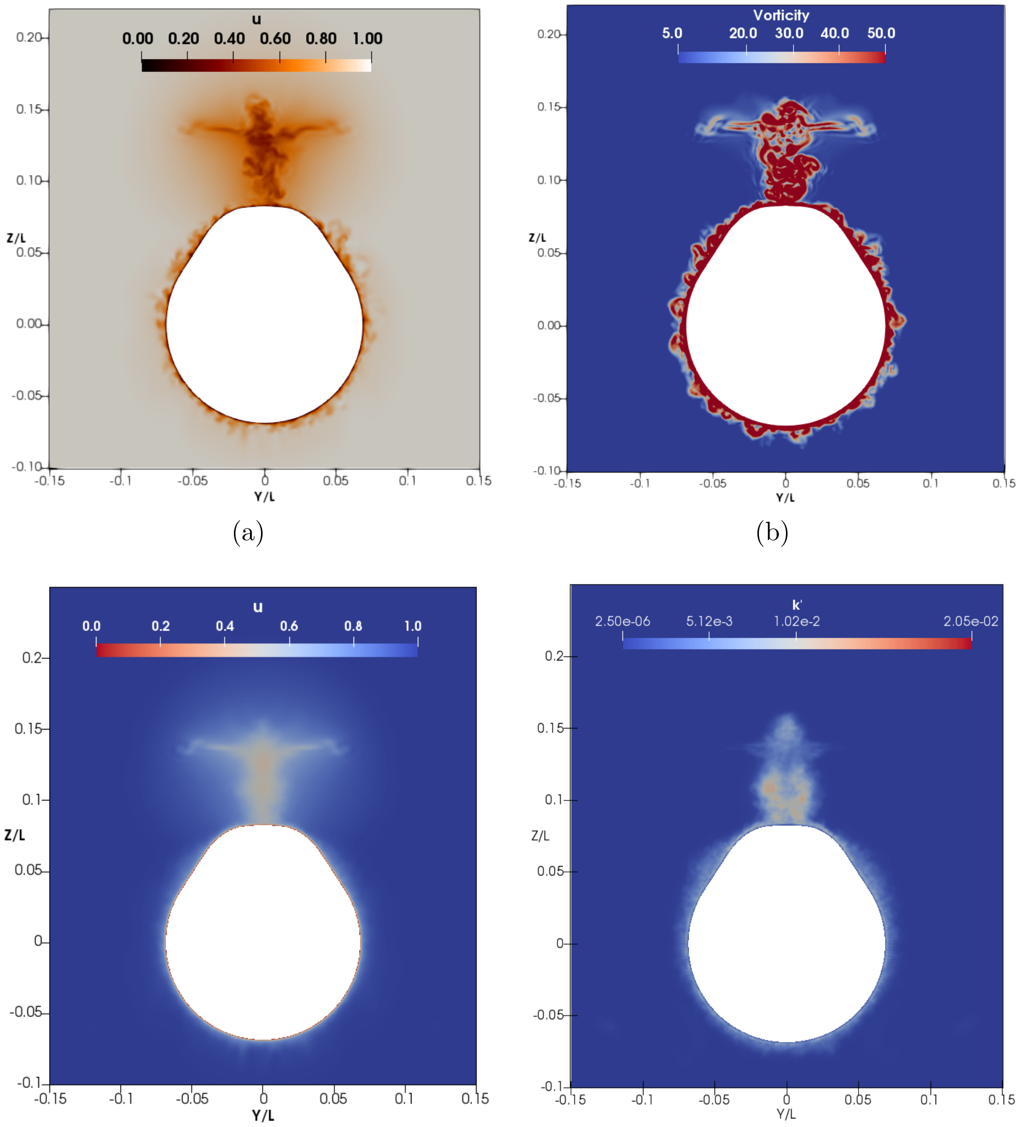

(a) (b)

(c) (d)

Figure 3.6: Instantaneous and time-averaged flow quantities at the plane W: (a) axial velocity field $u = U/U_\infty$; (b) Vorticity magnitude $|\omega| * U_\infty/L$; (c) Mean axial velocity field $u = \langle U \rangle/U_\infty$; (d) turbulent kinetic energy $k = \frac{u^2+v^2+w^2}{2}$

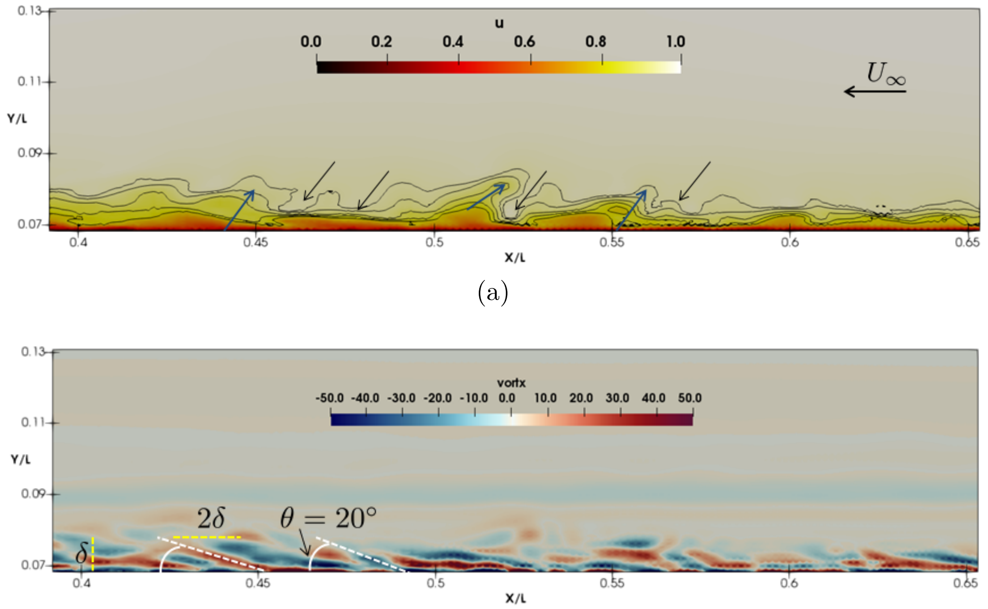

(a)

(b)

Figure 3.7: Instantaneous physical quantities at the plane H: (a) axial velocity field $u = U/U_\infty$; (b) non dimensional x-vorticity $\omega_x * U_\infty/L$

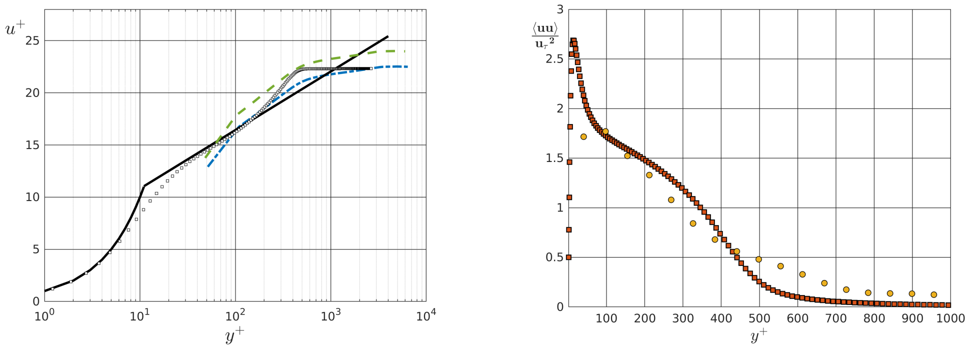

(a) (b)

Figure 3.8: (a) First order statistics. The law-of-the-wall (——); Present computation (- - -); Present computation scaled using u_τ from WR-RANS (-·-·); Wall-resolved LES data of turbulent flat plate at $Re_\theta = 1410$ from Eitel-Amor *et al.* (2014) (□) (b) Second order statistics. Present computation (●) Wall-resolved LES data of turbulent flat plate at $Re_\theta = 1410$ from Eitel-Amor *et al.* (2014) (■) ;

3.7 The turbulent wake

In this section the study of turbulent wake will be addressed, making comparison with theoretical results and experimental data. The physical model that better describes the physics of the wake is the axisymmetric wake. In our case, because of the submarine appendages and the shape of the hull itself, the wake is not perfectly axisymmetric; however, limiting the analysis to the plane H (see figure 2.2), we are still able to describe our wake using the axisymmetric wake theory (Johansson *et al.*, 2003).

Figure 3.9 shows the instantaneous turbulent wake in terms of non-dimensional velocity contours over two planes: the horizontal plane H (figure (a)) and the transverse plane Y (figure (b)). In figure 3.9 (a), the wake resembles the one generated by a streamlined body, whereas, on plane Y (figure 3.9 (b)) the trace of the sail along the entire wake is evident.

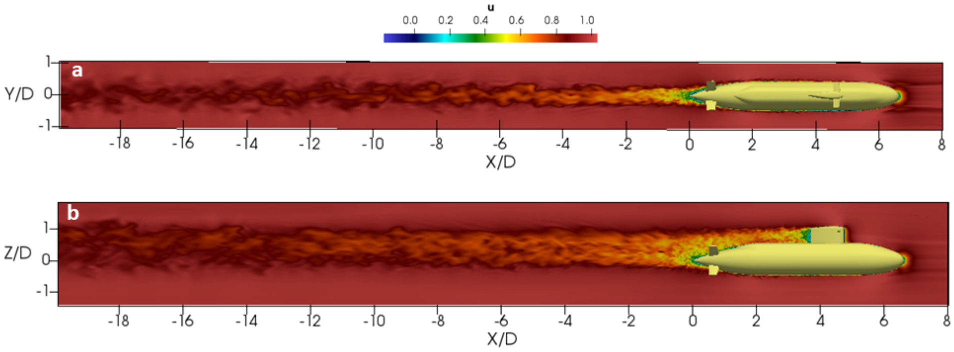

Figure 3.9: The turbulent wake: contours of instantaneous axial velocity $u = \bar{U}/U_\infty$. (a) Horizontal plane H. (b) Transverse plane Y

To develop the analysis it is comfortable to use a frame of reference as shown in figure 3.10. In this new frame of reference, streamwise direction is oriented as positive x.

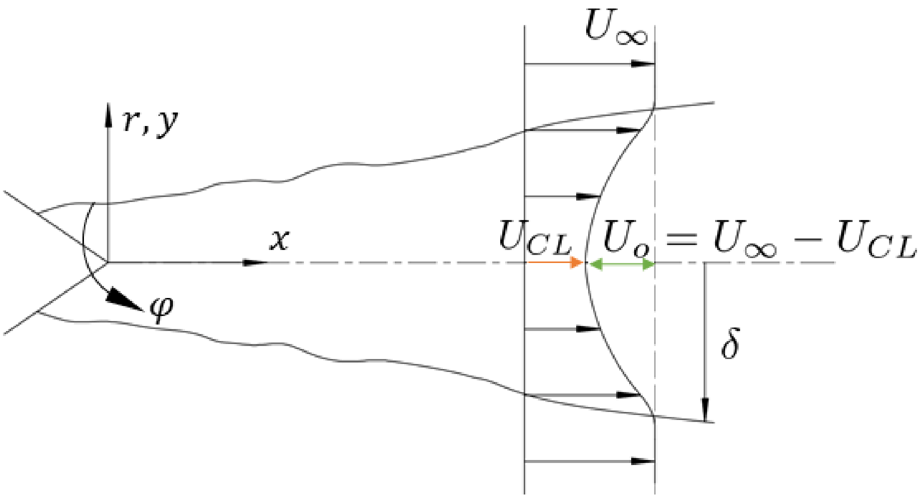

Figure 3.10: The turbulent wake: wake's coordinate system and schematic

The origin of the frame of reference is located at the stern of the submarine.

The study of the axisymmetric turbulent wake requires the definition of a set of new variables (Tennekes & Lumley, 1972; Pope, 2000). The velocity along the symmetry axis will be denoted with U_{CL}. The difference between the free-stream velocity U_∞ and U_{CL} is the velocity deficit, U_0. The radial distance from the center-line to the radius where U_0=0 is indicated by the Greek letter δ. The radial distance from the center line where the velocity deficit is $U_0/2$ is the half-wake width l_0. Turbulent axisymmetric wake can be characterized by the two scales U_0 and l_0. From a practical perspective is more convenient to calculate δ_* rather than l_0. δ_* is defined as:

$$\delta_*{}^2 = \lim_{R\to\infty} \frac{1}{U_0} \int_0^R (U_\infty - U) r dr \tag{3.3}$$

These two quantities are related as:

$$l_0 = \sqrt{2\,\ln 2}\delta_* \tag{3.4}$$

Moving downstream from the generator, the wake decays and spreads, the mean velocity profiles changes, maintaining its own shape (self-similarity), as shown in figure 3.11.

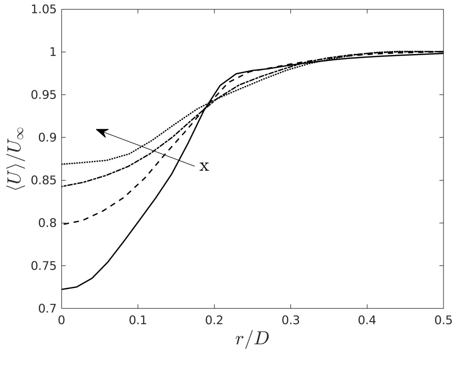

Figure 3.11: The turbulent wake: mean velocity profiles scales by far field velocity: $x/D = 3$ (——); $x/D = 6$ (- - -); $x/D = 9$ (-·-·); $x/D = 12$ (·····)

The region of the wake close to the body generator is called ”near wake” and it is a non-equilibrium region. This means that the wake is evolving. After a state of equilibrium has been reached (we will define ”equilibrium” in the next paragraph), the wake may achieve a state of *self-similarity*. Taking the mean axial momentum equation and integrating its leading terms over a cross section (Tennekes & Lumley, 1972), yields:

$$U_0\, {\delta_*}^2 = U_\infty\, \theta^2 \tag{3.5}$$

where θ is the momentum thickness, defined as:

$$\theta^2 = \lim_{R\to\infty} \frac{1}{{U_\infty}^2} \int_0^R U\,(U_\infty - U) r dr \tag{3.6}$$

At this stage, the average axial velocity profiles $U(x,r)$ scaled by the velocity deficit U_0 and δ_* collapse over a single curve, as shown in figures 3.12. To allow an easier visualization of the data they have been plotted into two different figures: figure 3.12 (a) shows the scaled mean axial velocity profiles for locations in the region $10 < x/\theta < 59$; figure 3.12 (b) shows the results for $65 < x/\theta < 107$. All these locations correspond to a distance $0.5 < x/D < 18$.

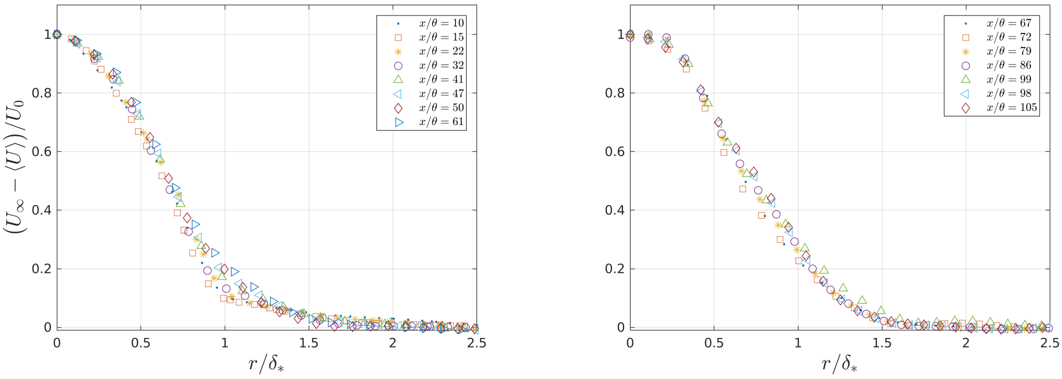

(a) (b)

Figure 3.12: The turbulent wake: mean axial velocity against radial distance scaled by velocity deficit and the wake's width. Data are averaged between the semi-planes at $\varphi = 0$ and $\varphi = \pi$.

George (1989) first argued that the classic similarity theory (for example as reported in Tennekes & Lumley (1972)) was based on not reliable assumptions. In particular, as shown in Johansson *et al.* (2003) the following evidences were observed:

- The wake growth rate depends on the generator geometry and on Re_θ
- The mean velocity profiles from all experiments collapse into a single curve when scaled with centerline velocity deficit and δ_*
- The turbulence intensity profiles might collapse if sufficiently downstream from the generator. In this case data available in literature are not completely in agreement.
- Data points for the scales U_0 and l_0 (Johansson *et al.*, 2003) might be fitted equivalently well by a power law with exponent (1/3), as predicted by the classic theory formulation (Pope, 2000; Tennekes & Lumley, 1972), or with exponent (1/2).

George (1989) proposed a new theory called *equilibrium similarity analysis*. He demonstrated that the mean velocity profiles from the different experiments collapse when scaled by U_0 and l_0, even if the wakes grow at different rates (i.e. even if the wakes were generated by different geometries). The differences caused by the geometry of the generator can be appreciated only on the spreading rate and on higher turbulence moments (Johansson *et al.*, 2003).

Differently from the classical theory, in the equilibrium similarity one, the local Reynolds number plays a fundamental role. Two different equilibrium similarity solutions indeed exist, and they depend on the local Reynolds numbers. So it is possible to make a distinction between ”high local Reynolds number” and ”low local Reynolds number” solutions. The mathematics yielding these two formulations is accurately formulated and developed in Johansson & George (2001); Johansson *et al.* (2003); When reaching the state of equilibrium self-similarity, the wake continues to evolve and decade, but the relative terms in the governing equations (momentum and Reynolds stress components) maintain the same relative importance. During this equilibrium decaying process the local Reynolds number monotonically decreases. For high local Reynolds number, an infinite Reynolds solution does exist , where viscosity is negligible compared to inertial effects. Momentum is conserved and the ratio between the maximum (radial direction) of the mean axial velocity fluctuation over the mean velocity deficit $\max(u)/U_0$ is constant. Moreover, in this region the velocity spectrum shows a developed inertial subrange region. In accordance with this theory, when the local Reynolds number drops below a certain level, the wake goes into unsteadiness, in the sense that the relative importance in the terms in the flow equations changes, evolving into a new equilibrium state; In this zone, $\max(u)/U_0$ assumes a constant value again, evidently different form the value in the high-Re regime. This new equilibrium regime is called *low-Reynolds*. According to theoretical arguments of Gourlay *et al.* (2001) (supported by DNS data analysis), in this region $\delta_* \sim x^{1/2}$ and $U_0 \sim x^{-1}$. Johansson *et al.* (2003) and Gourlay *et al.* (2001), analyzed the wake generated by a disk and a sphere and found that the transition from high-Re to a low-Re regime occurs at downstream distances of $x/\theta \approx$ 500-1000 (and Re_{l_0} about 500).

Following Johansson *et al.* (2003), Kumar & Mahesh (2018) found that for a streamlined generators, i.e. the axisymmetric not-appended DARPA submarine, the transition from high-Re to low-Re solution occurs at $x/D \approx 2$ and local Reynolds number $Re_{l_0} \approx 7000$. The velocity spectra evolution did not show any change in the inertial region, apparently contradicting the analysis of George (1989). On the other hand, Posa & Balaras (2016) in the analysis of the same submarine with appendages, did not observe the transition to low-Re solution (they studied the wake up to 12 D from the stern).

Johansson *et al.* (2003) found that, for high Reynolds regime, similarity scales U_0 and l_0 follow power-law relationships of the form

$$U_0 = A\left(\frac{x + x_0}{D}\right)^{-2/3} \tag{3.7}$$

$$l_0 = B\left(\frac{x + x_0}{D}\right)^{1/3} \tag{3.8}$$

This is clearly the same result as the physical law of classic theory (Townsend, 1956).

Applying the similarity scales of equation 3.8 to the present LES simulation of the BB2 submarine, we can obtain the value of A, B and x_0 using a non-linear curve fits. In particular, the best fit is obtained by minimization of the squared residuals

σ^2 and keeping x_0/D to be equal in the two relationships:

$$U_0 = 0.887\left(x/D + 2.827\right)^{-2/3} \tag{3.9}$$

$$l_0 = 0.129\left(x/D + 2.827\right)^{1/3} \tag{3.10}$$

For comparison purposes, table 3.4 lists the power laws proposed by Jiménez *et al.* (2010b) (experimentally) and Posa & Balaras (2016) (numerically).

Item	$\mathbf{Re_L}$	**A**	**B**	$\mathbf{x_0/D}$
Present LES	1.2×10^6	0.89	0.13	2.83
Jiménez *et al.* (2010b)	1.1×10^6	1.18	0.113	2.08
Posa & Balaras (2016)	1.2×10^6	1.57	0.13	4.58

Table 3.4: The turbulent wake: power laws relationships coefficients for u_0 and l_0.

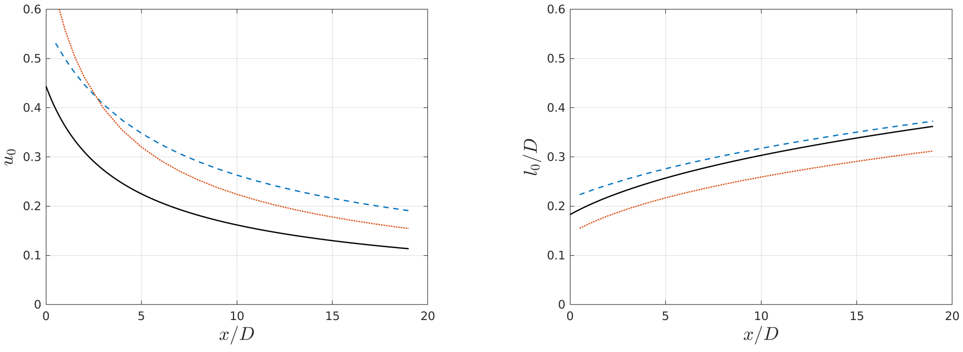

(a) (b)

Figure 3.13: The turbulent wake: data fitting for velocity and length scales. Present LES (——); Posa & Balaras (2016) (dashed line); Jiménez *et al.* (2010b) (dotted line)

Figure 3.13 shows the behavior of $u_0 = U_0/U_\infty$ and l_0 during the wake evolution. The correlations for the DARPA-SUBOFF proposed by numerical work of Posa & Balaras (2016) (dashed lines) and experimental data from Jiménez *et al.* (2010b) (dotted) are shown for comparison.

Figure 3.14 shows the local Reynolds number evolution. At 18 diameters downstream from the stern its value is still elevated. As shown in figure 3.15, the present data solution are well fitted using a power of (1/3), and they are close to the high-Re solution of Kumar & Mahesh (2018). Table 3.5 shows comparison between the curve fit coefficients for δ_*/θ.

Item	$\mathbf{Re_L}$	**A**	$\mathbf{x_0/D}$
Present LES	1.2×10^6	1.16	1.89
Kumar & Mahesh (2018) High-Re	1.1×10^6	1.17	2.08
Kumar & Mahesh (2018) Low-Re	1.1×10^6	0.78	2.08

Table 3.5: The turbulent wake: power laws relationships coefficients for δ_*/θ

In addition, looking at the velocity spectra of figure 3.16 we do not see changes in the extension of the inertial subrange region, as Johansson *et al.* (2003) suggests for predicting the wake passage to a low-Re regime. For all these reasons we may argue that the present wake is still in a high-Re number solution state.

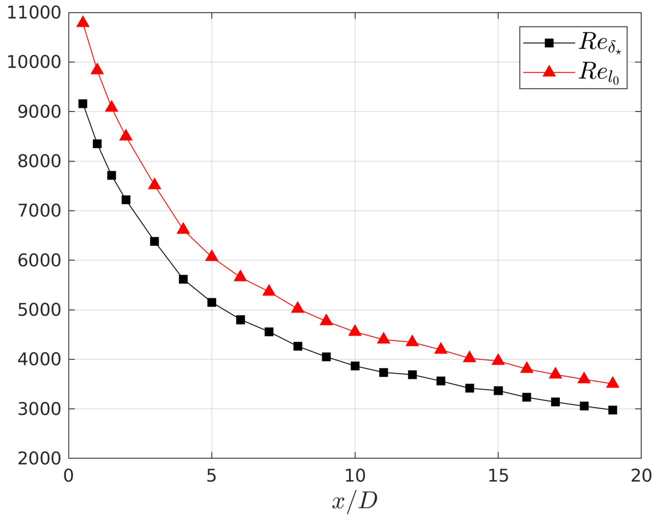

Figure 3.14: The turbulent wake: the local Reynolds number $Re_{l_0} = U_0 \, l_0/\nu$ and $Re_{\delta_*} = U_0 \, \delta_*/\nu$

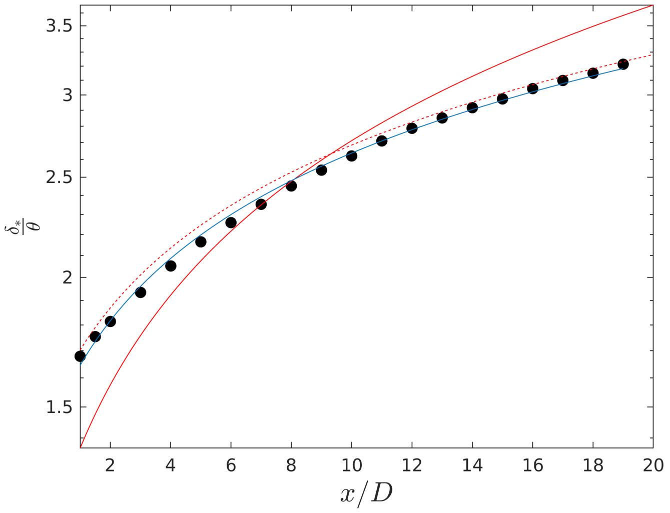

Figure 3.15: The turbulent wake: evolution of the wake width scaled by momentum thickness. Present simulation (●). Power law for the present simulation $\delta_*/\theta = 1.16\,(x/D + 1.89)^{1/3}$ (—); High-Re solution $\delta_*/\theta = 1.17\,(x/D + 2.08)^{1/3}$ (- - -) (Kumar & Mahesh, 2018). Low-Re solution $\delta_*/\theta = 0.78\,(x/D + 2.08)^{1/2}$ (—) (Kumar & Mahesh, 2018).

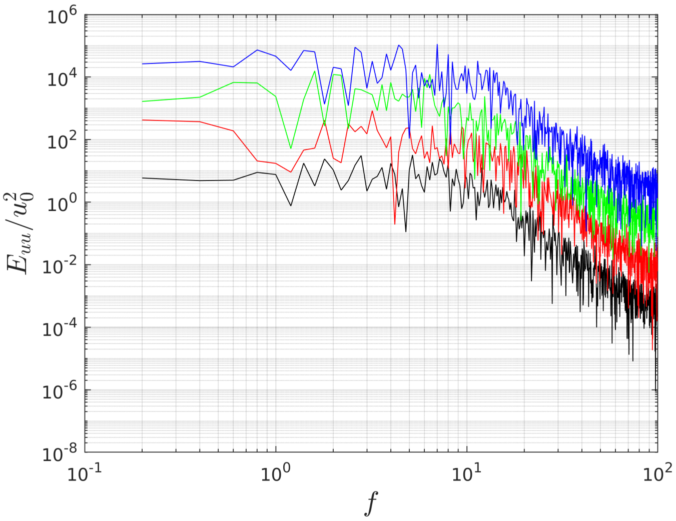

Figure 3.16: The turbulent wake: evolution of streamwise velocity spectra. (Data are moved upward as: at $3D$ $E_{uu} \times 10^2$, at $6D$ $E_{uu} \times 10^3$, at $9D$ $E_{uu} \times 10^5$

Further, looking at the ratio between turbulence velocity fluctuations and velocity deficit (figure 3.17) we can assert that turbulence governing laws are still evolving to a state of equilibrium, as intended by George (1989). Figure 3.18 shows the turbulent kinetic energy profiles at 3, 6, 9 and 12 diameters from the stern. Solution at $9D$ is in rather good agreement with numerical data from Posa & Balaras (2016) at the same distance from the stern. The two peaks characterizing TKE in H plane derive from the turbulent boundary layer transported downstream (Posa & Balaras, 2016). Away from the stern the velocity deficit rapidly decreases, and turbulent fluctuations maintain their intensity also in the far wake (Gourlay *et al.*, 2001; Johansson *et al.*, 2003). The two peaks of turbulent kinetic energy are also clearly visible looking at the color plot of k/U_∞^2 in the near-wake region (figure 3.19).

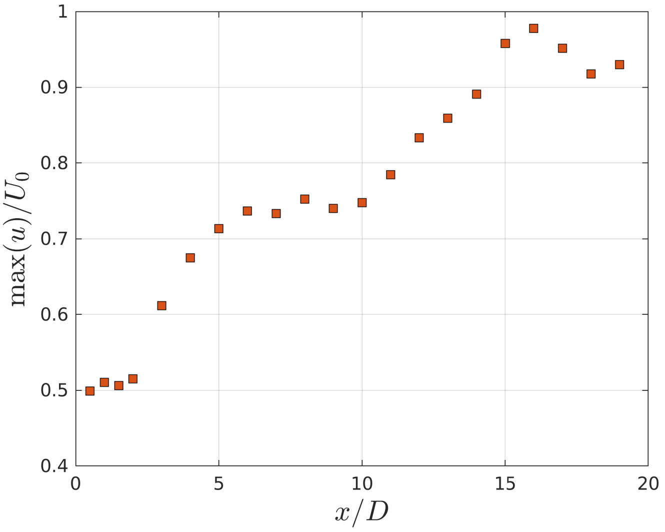

Figure 3.17: The turbulent wake: evolution of maximum velocity fluctuations scaled by the velocity deficit

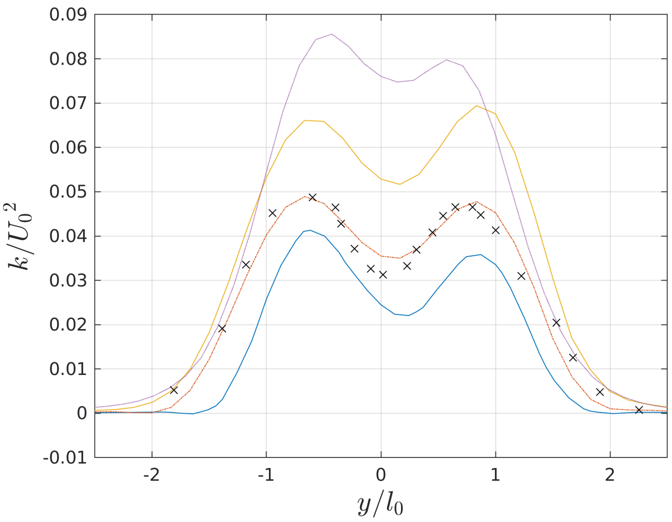

Figure 3.18: The turbulent wake: evolution of the non-dimensional turbulent kinetic energy. $6D$ (—); $9D$ (—); $12D$ (—); $15D$ (—); numerical data from Posa & Balaras (2016) $9D$ (×)

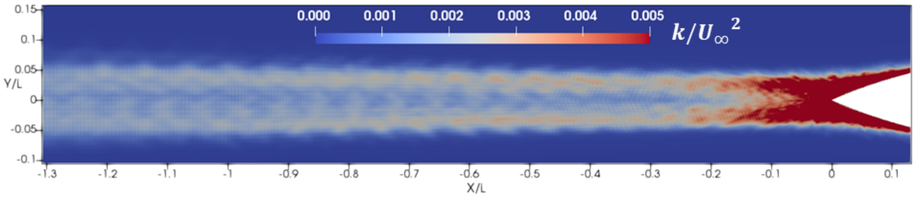

Figure 3.19: The turbulent wake: turbulent kinetic energy in the near-wake region

4

Hydroacoustic analysis

In this chapter we discuss the computational hydroacoustic analysis of the BB2 submarine at $Re_L = 1.2 \times 10^6$.

4.1 CHA of the fully appended BB2 submarine

In this section, the results from the hydroacoustic analysis of the LES data of chapter 3 will be presented. The BB2 submarine is at model scale. The RANS and LES were conducted considering the submarine submerged in a moving medium. Thus the formulation of the FW-H equation adopted here is the formulation 1D (Cianferra *et al.*, 2019*a*), for the wind tunnel problems (see equation 1.51 and equation 1.52). The hydroacoustic solver has been extensively validated in Cianferra (2017); Cianferra *et al.* (2019*a*,*b*). The surface f coincides with the submarine body and the volume integrals are calculated over the whole computational domain. Under these conditions, the contribution to the noise derives from both the loading and quadrupole terms. The thickness term is null everywhere, as explained in section 1.5.6.

The computation is done under the common hypothesis that the contribution of the viscous forces to noise is small compared the one coming from pressure and turbulence. As a consequence, the compression tensor $P_{ij} = (p - p_0)\delta_{ij} - \sigma_{ij}$, where σ_{ij} is the viscous stress tensor, can be approximated only with the first term on the RHS. It has to be highlighted that, this approximation is well suitable with use the wall-functions. Indeed, in chapter 3 we saw that using Spalding's formulation for the law-

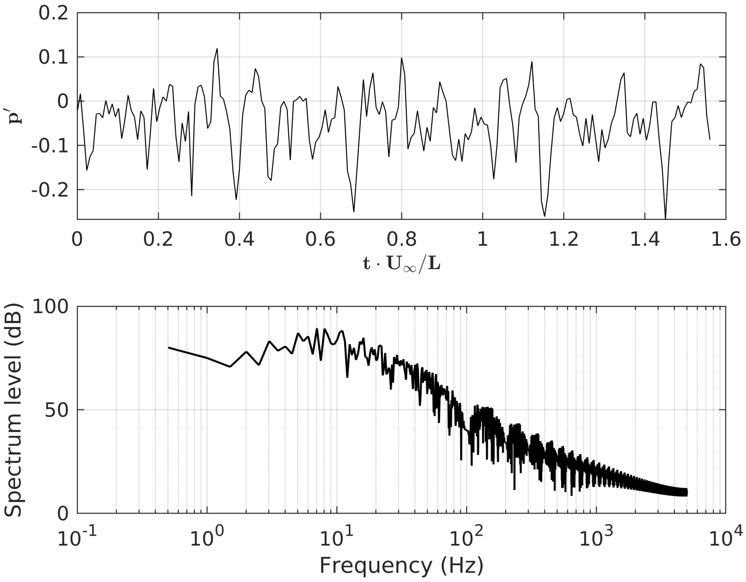

Figure 4.1: Pressure signal and relative spectrum sampled at (0.5 L, 0, 0.12 L)

of-the-wall with the WALE sub-filter scale model, yields to underprediction of the skin-friction factor. From fluid-dynamics point of view this is a drawback ,whereas it can be considered a problem of minor importance from acoustics perspective. Moreover, as shown in section 3.7) the wake develop in the high local Reynolds number regime where viscosity effects are in general negligible.

Before starting the acoustic analysis using analogies, the LES pressure signal has been sampled at specific locations near the submarine to determine which is the maximum relevant frequency. For example, figure 4.1 shows the signal and the relative spectrum sampled using a probe located in the plane behind the sail with coordinates (0.5 L, 0, 0.12 L). The sampling time is about 1.5 t_c. The maximum relevant fluid-dynamic frequency it is equal to $f_{max} = 100\,Hz$. The spectra of the pressure signals sampled at the other characteristic positions, as for example close to the hull, in the plane behind the sail or in the wake, decades even faster.

Thus, since $f_{max} = 100Hz$, positioning the hydrophones in the near field, the calculation of time delays can be avoided, because MPF>1.

Hydroacoustic analysis

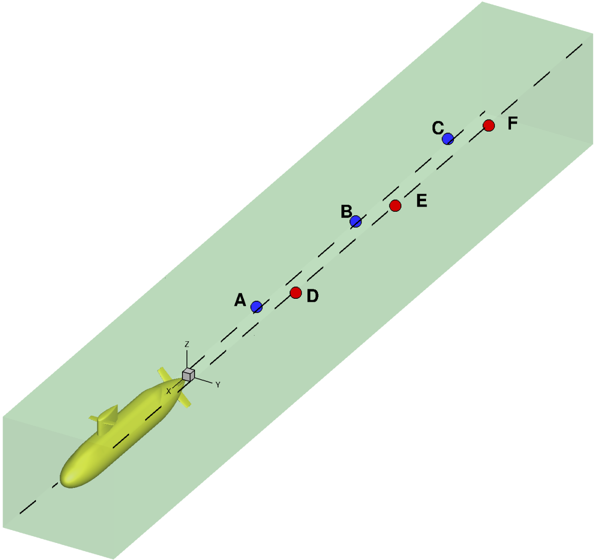

Figure 4.2: Hydrophones' locations

The positions of the hydrophones considered in the present analysis is shown schematically in figure 4.2, while table 4.1 reports the coordinate of the locations. These hydrophones are suitable for the characterization the hydroacoustic of the turbulent wake.

Figures 4.4, 4.5, 4.6, 4.7, 4.8, 4.9, show the sound pressure levels, in decibel, against the frequency for each virtual hydrophone (hereinafter we will avoid to use the adjective "virtual" when referred to the hydrophones). The contribution of the loading term are shown in figures (a). Turbulence is mainly present in the quadrupole term which contributes mostly to the sound pressure level and, differently from the aeroacoustic case, it is clear that it can not be neglected. Loading term contribution is smaller than quadrupole one. This is probably due to the model dimensions and the absence of a rotating propeller. Hydrophones in position D, E and F recorded the highest level of noise and this probably means that the sail contribution to the noise is significant. The maximum value is about $100dB$ at $1Hz$, evidenced by a characteristic peak. The same maximum SPL (without the peak) was found sampling pressure during LES (figure 4.1). We associate this frequency to the noise

Hydrophone ID	x/D	y/D	z/D
A	-5	-2	-2
B	-10	-2	-2
C	-18	-2	-2
D	-5	2	2
E	-10	2	2
F	-18	2	2

Table 4.1: Hydrophones' positions

produced by the sail wake flow. Figure 4.3 shows time-contours visualization of the sail wake.

The loading term is negligible compared to the quadrupole and, in absence of the propeller, it could be omitted in the estimation of the noise.

Figure 4.10 shows the comparisons of the spectra at different locations. In figure (a) the spectra from hydrophones A, B and C are reported; Figure (b) shows the spectra of the signal sampled at positions D, E and F. Figure (c) compares spectrum B with spectrum E. As we can see, the noise associated to the high frequencies grows farther from the submarine. A reason of this is that close to the submarine the characteristic length of the largest turbulent structures can be taken of the same order of magnitude of diameter of the main body. These vortices are characterized by large characteristic times and so they have small characteristics frequencies. The breaking up process of these vortices starts just downstream the propeller plane and, as a consequence, the wealth of small structures increases downstream. Small eddies have low characteristic time and, thus, large characteristic frequency.

Figure 4.11 shows the directivity pattern of the sound pressure. The data are plotted in a cylindrical-coordinate frame of reference (ϑ, p_{rms}), where the radius indicates the RMS pressure at the observer location. Hydrophones are distributed over a circumference centered at (-10D, 0, 0), and radius of R=2D, on a plane orthogonal to the submarine axis. The azimuthal distance between two consecutive hydrophones is 15°. From $\vartheta = \frac{3}{2}\pi$ to $\vartheta = \pi$, p_{rms} is approximately homogeneous in ϑ direction. The effect of the junctions between the sail and the hull, the sailplane and the sail, and - even more important - the effect of the whole wake (with the

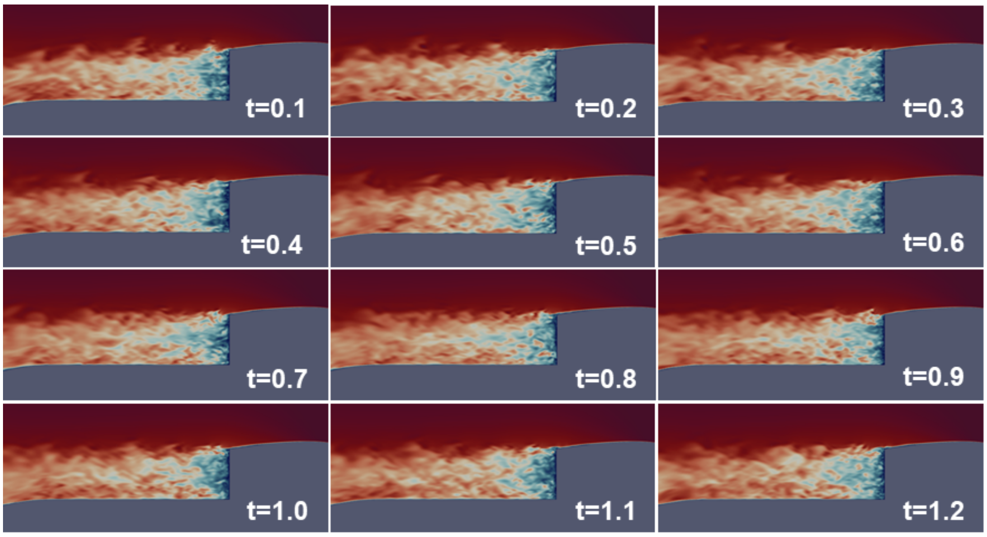

Figure 4.3: Time-contours plots of the sail wake

contribution from the TBL and sail wake), determines an increase of the sound level in the second (and first) quadrant.

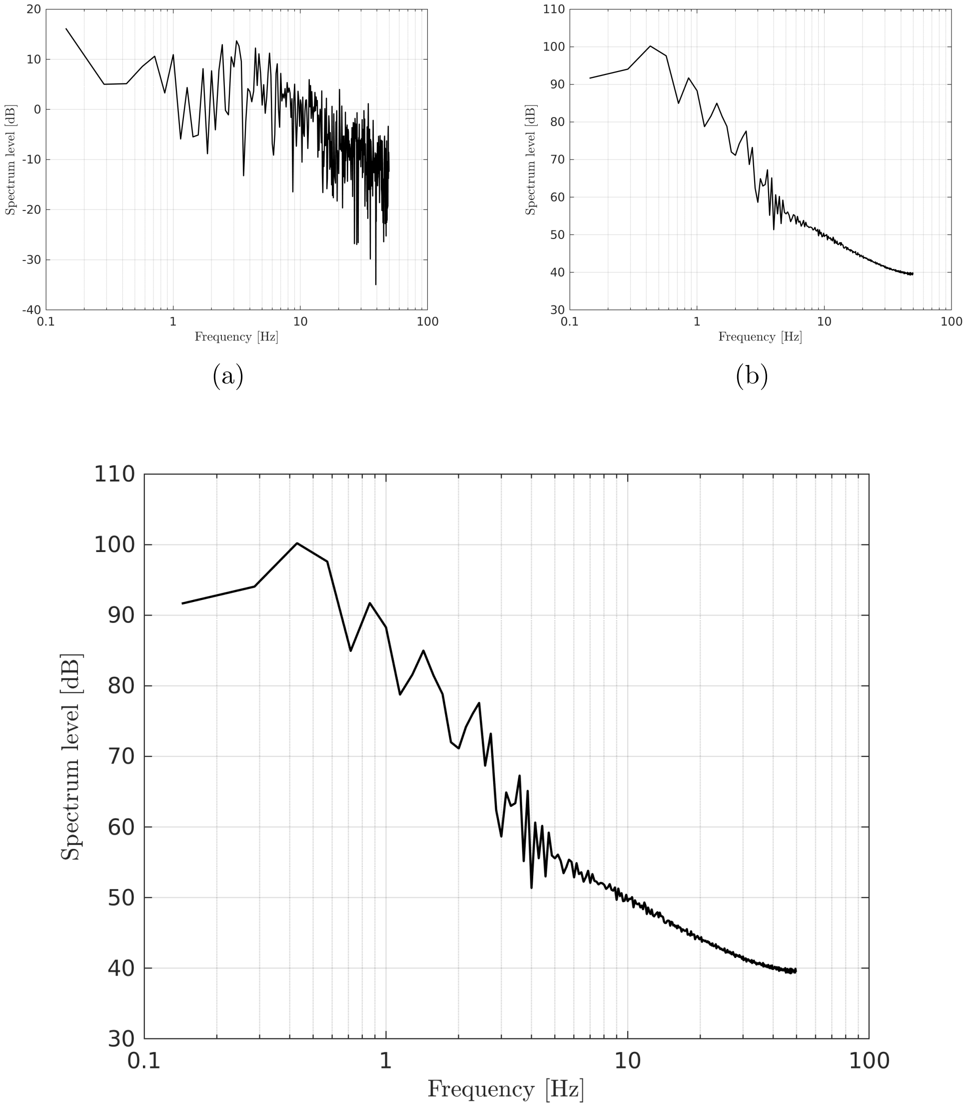

(a) (b)

(c)

Figure 4.4: Sound pressure level sampled by hydrophones in position A. Linear Term p_L (a); Quadrupole term p_Q (b); Contribution of all terms $p_L + p_Q$.

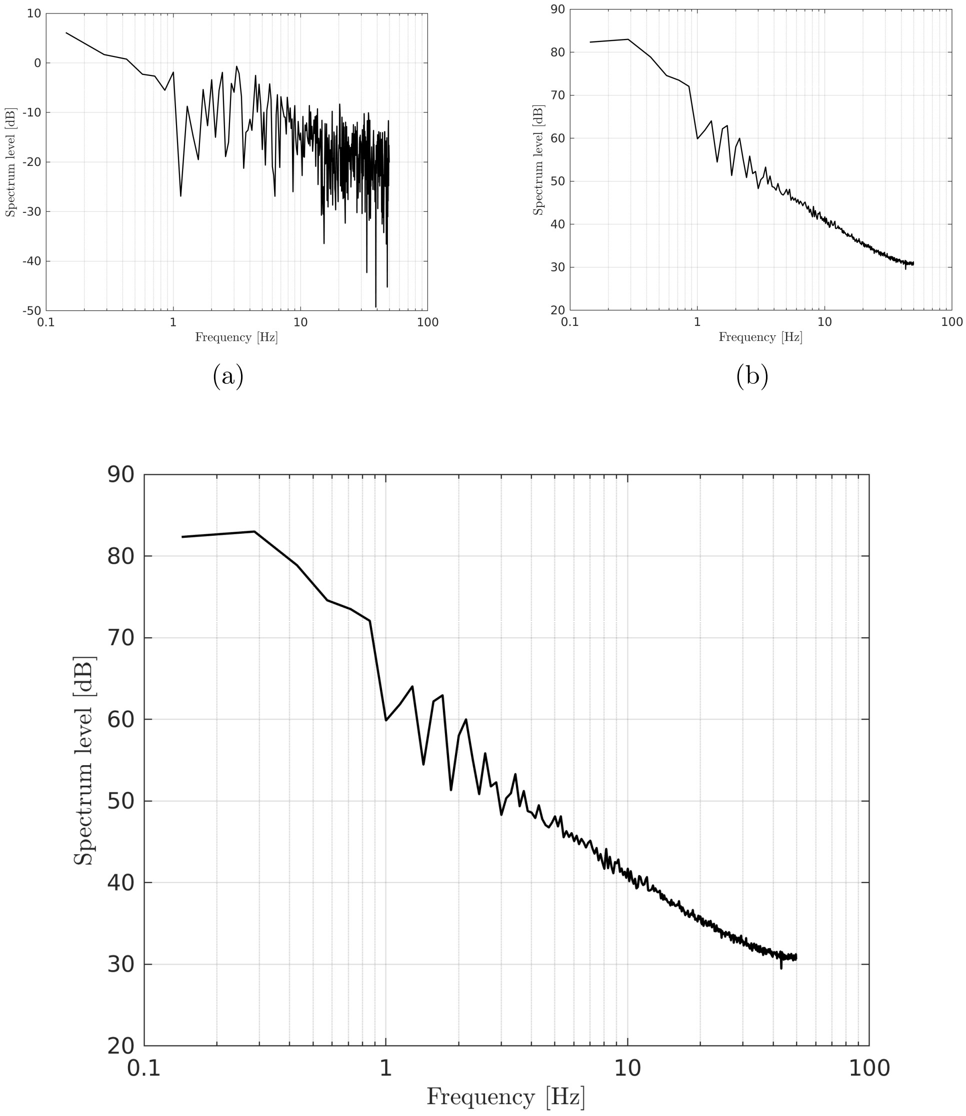

(a)

(b)

(c)

Figure 4.5: Sound pressure level sampled by hydrophones in position B. Linear Term p_L (a); Quadrupole term p_Q (b); Contribution of all terms $p_L + p_Q$.

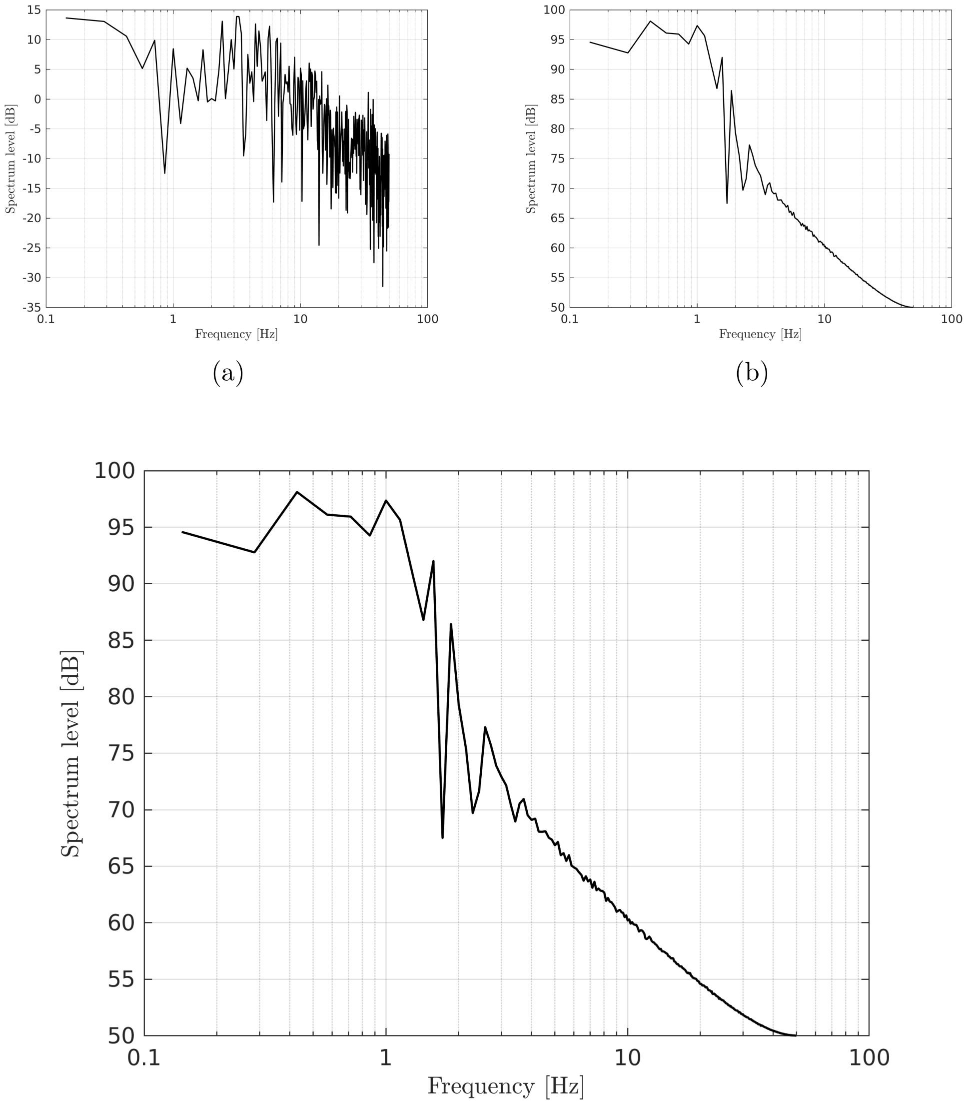

(a)

(b)

(c)

Figure 4.6: Sound pressure level sampled by hydrophones in position C. Linear Term p_L (a); Quadrupole term p_Q (b); Contribution of all terms $p_L + p_Q$.

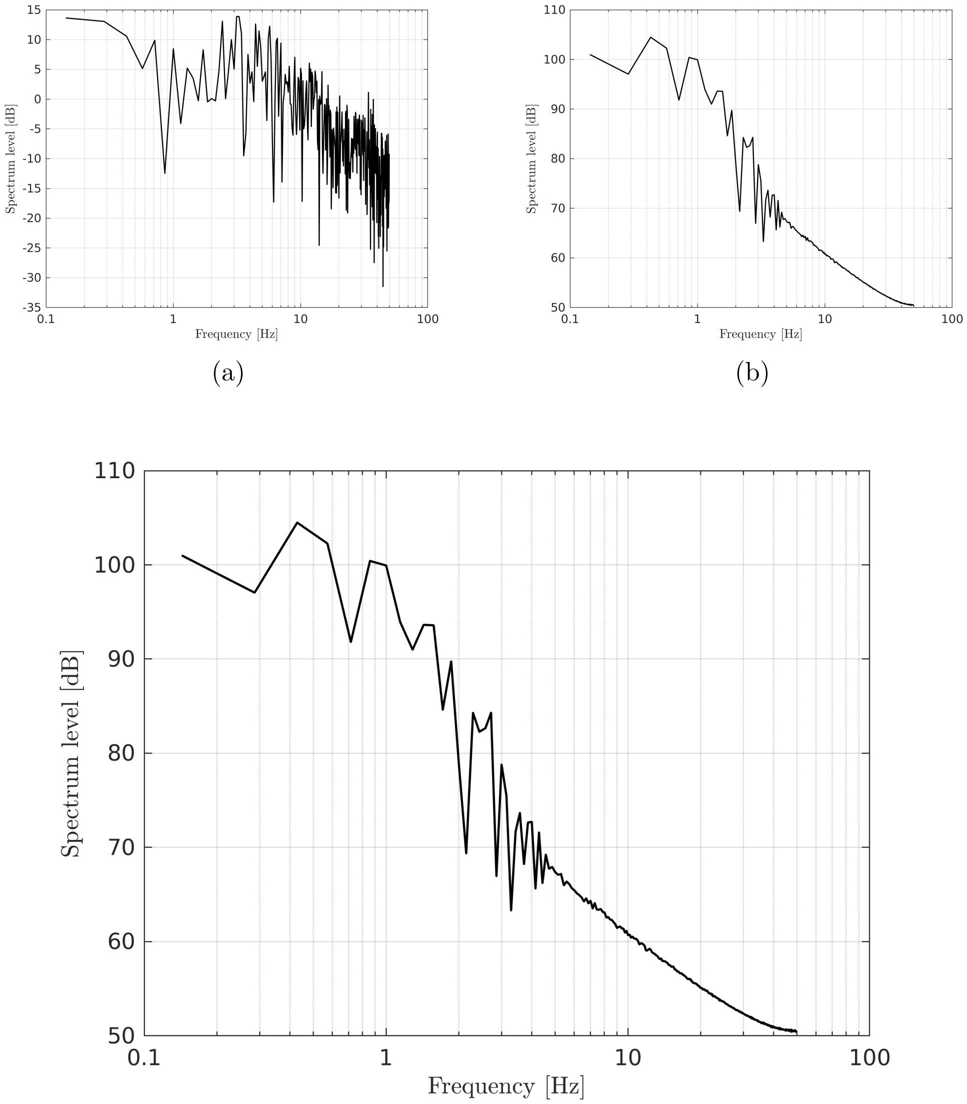

(a) (b)

(c)

Figure 4.7: Sound pressure level sampled by hydrophones in position D. Linear Term p_L (a); Quadrupole term p_Q (b); Contribution of all terms $p_L + p_Q$.

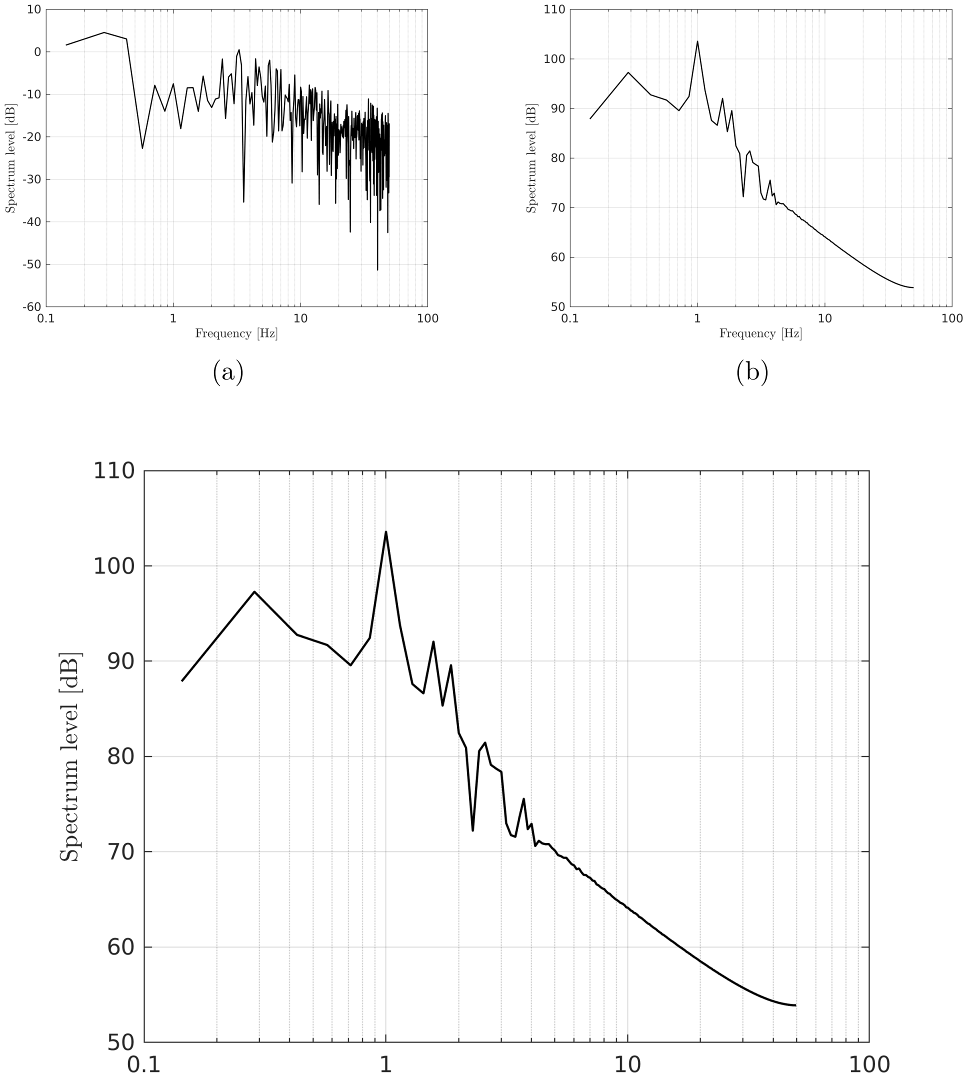

(a)

(b)

(c)

Figure 4.8: Sound pressure level sampled by hydrophones in position E. Linear Term p_L (a); Quadrupole term p_Q (b); Contribution of all terms $p_L + p_Q$.

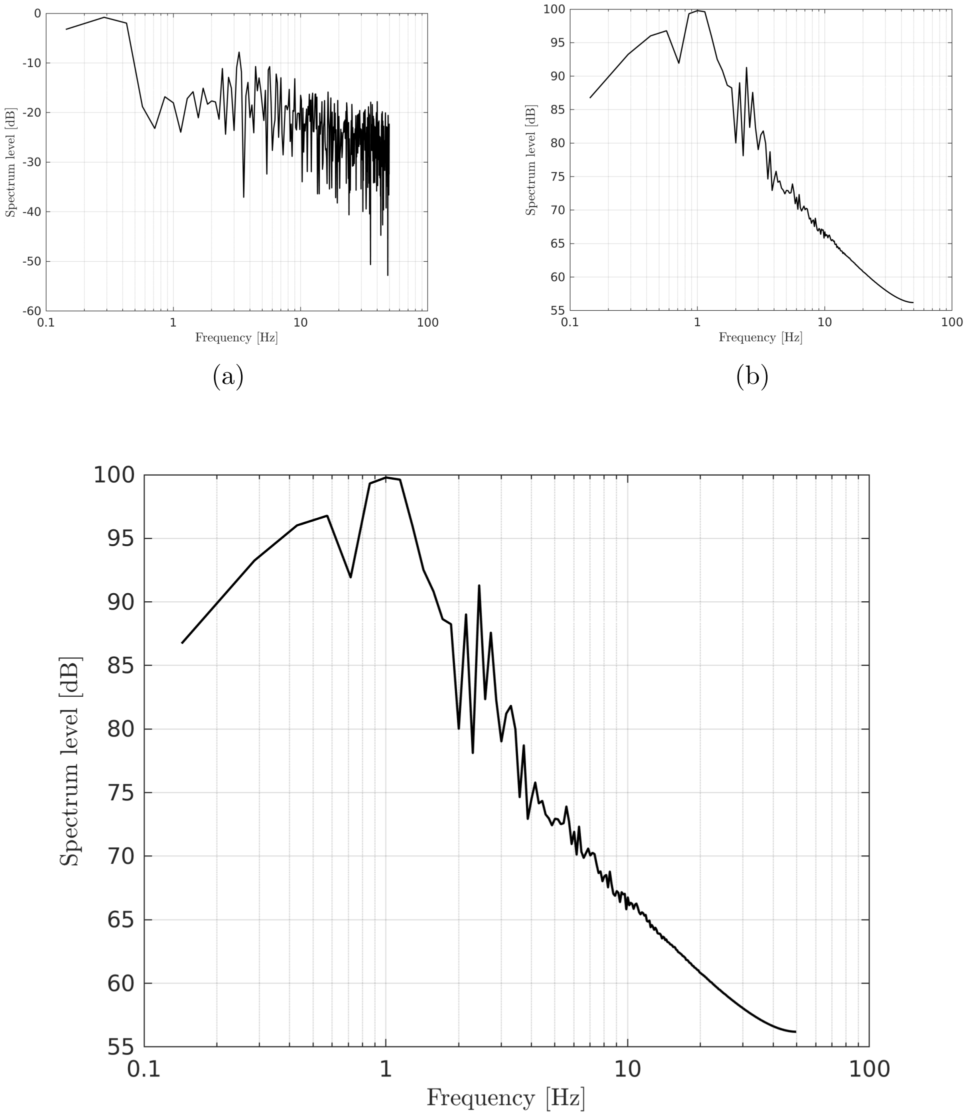

(a) (b)

(c)

Figure 4.9: Sound pressure level sampled by hydrophones in position F. Linear Term p_L (a); Quadrupole term p_Q (b); Contribution of all terms $p_L + p_Q$.

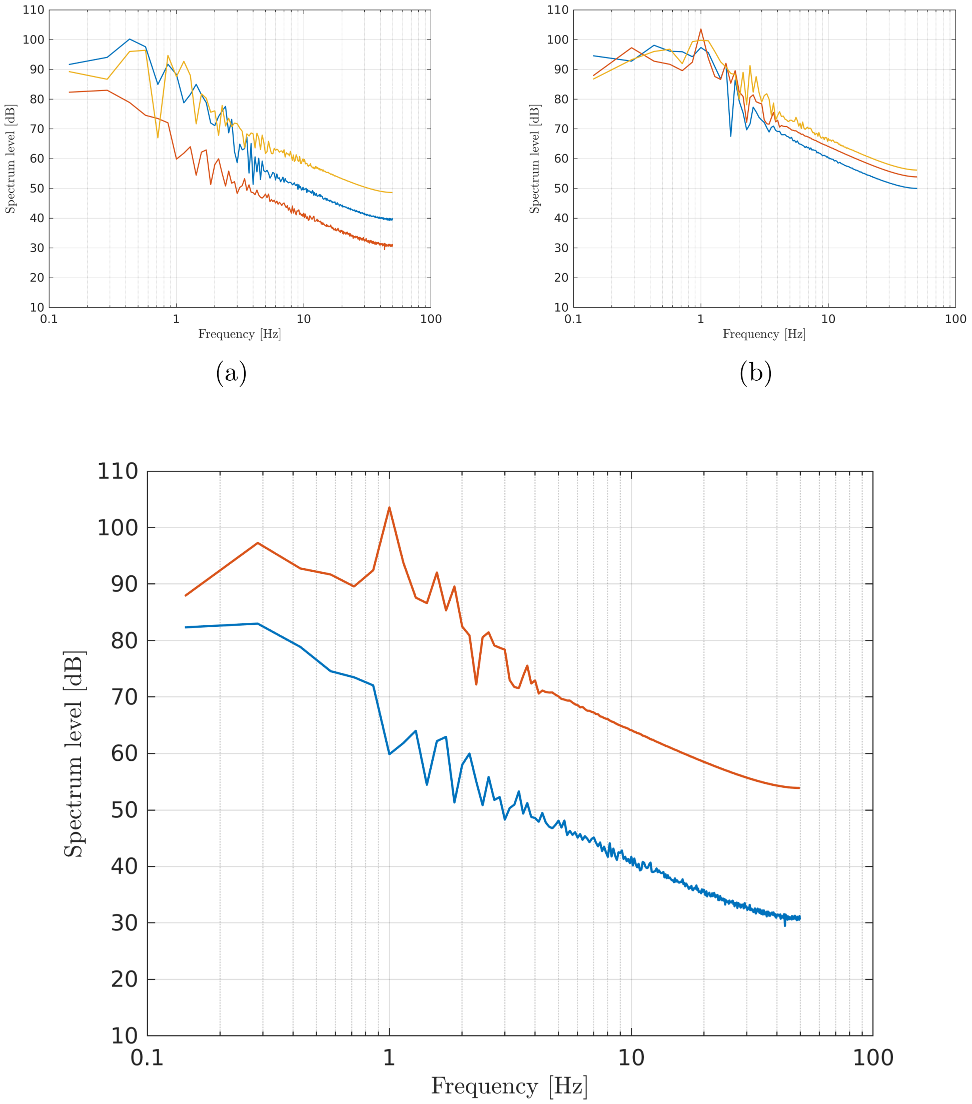

(a)

(b)

(c)

Figure 4.10: (a) Sound pressure level from hydro-phones in position A (—), B (—) and C (—); (b) Sound pressure level from hydro-phones in position D (—), E (—) and F (—); (c) Sound pressure level from hydro-phones in position B (—) and E (—);

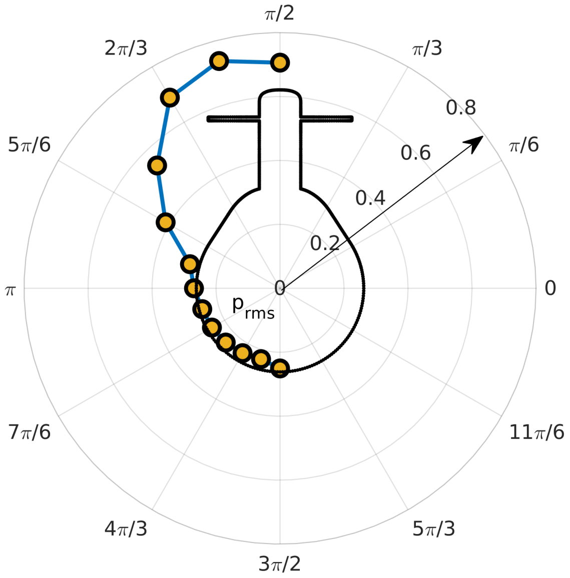

Figure 4.11: Directivity pattern of the sound pressure calculated at $10D$ downstream from the stern

5

Conclusions

The present thesis focuses on the computational characterization of both hydrodynamics and hydroacoustics of a notional submarine, namely the BB2.

Applying the advective form of the FW-H equation together with Wall-Modeled LES to the BB2 submarine allowed to provide a complete characterization of the computational hydrodynamics and hydroacoustics. The utilization of the advective form of FW-H equation (here named *formulation 1D*) represents a novelty and opens to detailed information about the turbulence generated sound of such complex bodies.

WM-LES allows to obtain a significant reduction of computational resources with a high-fidelity representation of the fluid-dynamic and turbulence features of the wake.

The flow conditions are those of a typical ”wind-tunnel” problem, i.e. in straight ahead advancement at zero-degree drift angle. Numerical simulations and radiated noise estimations have been performed at model scale (scale factor $\lambda = 0.054$, $Re_L = 1.2 \times 10^6$, $U_\infty = 0.2613\, m/s$). To perform the numerical simulations we employed a customized version of the open-source library OpenFOAM. Regarding the turbulence model, CFD analysis was conducted using two approaches, respectively RANS and WM-LES. In case of RANS simulations turbulence is completely modeled, while in LES, after applying an implicit filter operation, only a relatively small part of turbulence spectrum is modeled (the so-called sub-grid scales, i.e. the approach directly resolves the larger energy-carrying scales and models the smaller energy dissipating ones).

Conclusions

The analysis of the RANS simulations was preparatory to the study performed by means of LES approach, both to become familiar with OpenFOAM and prepare the best computational mesh. RANS has been performed at two different advancement speeds, $U_\infty = 3\,m/s$ and $U_\infty = 0.38\,m/s$, i.e. at Reynolds numbers, $Re_L = 9.57 \times 10^6$ and $Re_L = 1.2 \times 10^6$, respectively.

At higher Reynolds number, $k - \omega\, SST$ model has been utilized for the simulations. Both WR and WM approaches have been employed. At Reynolds number 1.2×10^6, $k - \omega\, SST$ model has been applied to the WR simulation, while $k - \varepsilon$ model to the RANS with wall-functions. The wall-function adopted for the WF simulations at high- and low-Reynolds number, is the Spalding's continuous formulation.

RANS solution has been utilized as initial condition in LES at $Re_L = 1.2 \times 10^6$. In order to reduce the computational effort for the LES, the near-near wall behavior was modeled (adopting again the Spalding's continuous formulation of the law-of-the-wall). The transition to turbulent of the boundary layer on the hull has been triggered using a numerical tripping, which is constituted by a zero-mean spatial distribution of random body forces. In the analysis of the LES solution, special attention has been paid to the characterization of the turbulent wake because, in absence of a propeller, it represents the major source of noise. To be noted that the presence of propeller is not considered in the present study, since it is the first literature study where the acoustic signature of the BB2 submarine is investigated. For this reason, it is more convenient to focus on the main body in order to obtain a full characterization. Otherwise, the interaction with the propeller may vary the acoustic signature also in view of the characteristics of the propeller.

LES opens to the possibility of an accurate characterization of the acoustic signature of the submarine. In fact, as suggested in Ianniello (2016), fluid dynamic solutions obtained using URANS are not adequate to conduct an accurate hydroacoustic analysis. At this scope, Cianferra *et al.* (2019*a*) extended the work of Najafy-Yazdi *et al.* (2010), allowing to add the quadrupole noise source term to the integral advective form of FW-H. The advective form of FW-H equation applies to wind-tunnel problems and the quadrupole term it is of fundamental importance in hydroacoustic problems (in the past it was often neglected because considered important only at very high $Mach$ number, as it happens in CAA). Thanks to these theoretical achievements, the CHA toolkit was implemented as a post-processing tool of OpenFOAM and extensively validated in Cianferra *et al.* (2019*a*), Cianferra *et al.* (2019*b*).

Conclusions

From RANS simulations we observed that at high-Re the numerical solutions obtained using WR- and WM-RANS are in good agreement with reference literature data, in terms of both hydrodynamic loads and fluid dynamic fields. The pressure distribution on the hull was accurately captured in both cases. The skin-friction coefficients also showed a good agreement between the two approaches, with exception of the zone in front of the sail (at the junction with the hull) where WM-RANS failed in predicting the two vortices (it actually predicted a single vortex). At Re=1.2×10^6, we noted that RANS with WM estimates higher wall-shear stress over the hull then the WR counterpart. RANS with WM predicts higher streamwise and vertical loads (of about 10%) then WR.

The utilization of LES together with wall-models was imposed by the availability of computational resources and justified by the fact that, for the purpose of a successive acoustic analysis, the wake is the most significant contribution to noise, and the solution provided by a WMLES reveals to be suitable for our purposes. In fact, we found a rather good agreement with numerical and experimental results from of Posa & Balaras (2016) and Jiménez *et al.* (2010a,b), respectively, for what concerns the characteristic length l_0 and velocity u_0 scales of the wake. A (1/3) power-law well fits the evolution of the wake width, made non-dimensional by momentum thickness, i.e. $\delta_\star/\theta$. Moreover, following the equilibrium similarity theory (George, 1989; Johansson & George, 2001; Johansson *et al.*, 2003), we were able to determine that, up to a distance of 18 D downstream, the wake is still in a state of development towards a high-Re equilibrium similarity solution. Indeed, to attains the state of equilibrium similarity, the ratio between the maximum fluctuations in streamwise direction u and U_0 should not vary in space (Johansson *et al.*, 2003). Differently from Kumar & Mahesh (2018), no transition from high- to low-Re solution was observed. Indeed, the local Reynolds number at 18 D downstream was still relatively high ($Re_{\delta_\star} \approx 3500$). The mean velocity profiles collapsed into a single curve when scaled with the centerline velocity deficit and the wake width, (Tennekes & Lumley, 1972). In the wake the decay of turbulent kinetic energy is slower than that of momentum deficit. In fact, the non-dimensional k profiles increases downstream and the dual peak is associated with turbulence coming from the boundary layer over the stern, as in (Jiménez *et al.*, 2010a; Posa & Balaras, 2016).

The utilization of wall-models in LES leads to underestimation of the wall-shear stress over the hull (Larsson *et al.*, 2016; Mukha & Liefvendahl, 2015) with respect to experiments and WR RANS results at the same value of Reynolds number. As expected, also the non-dimensional Reynolds stress tensor component $\langle uu \rangle / u_\tau$ was underestimated with respect to ZPGTBL WRLES data of Eitel-Amor *et al.* (2014).

The acoustic solver was fed by numerical data gather during LES computation. The novel formulation 1D (Cianferra *et al.*, 2019*a*) of FW-H equation has been employed. The advantage of formulation 1D is that it is written in advective form (it is the formulation required to solve wind-tunnel problems) and, differently from the previous formulation 1C (Najafy-Yazdi *et al.*, 2010), accounts for the non-linear quadrupole source term. In particular, the loading term has been integrated over the submarine surface, while the quadrupole one has been integrated in the volume region surrounding the underwater vessel (see equation 1.51 and equation 1.52). LES data were stored with a frequency of 100 Hz (as suggested by the spectra of the LES pressure signal sampled at significant locations) for about 9 t_c (Ianniello, 2016; Ianniello *et al.*, 2013; Ianniello, 2007). The acoustic noise was calculated at specific locations by virtual hydrophones. The main contribution to the noise was brought from the non-linear quadrupole term (turbulence and vorticity effects). For the BB2 submarine at model scale, maximum noise has been estimated to be about 100 dB. The level of noise is already remarkable and dangerous for the traceability of the submarine, since it is already well above the ocean background noise. The spectra of the acoustic pressure, sampled from hydrophones located near the sail, were characterized by a peak at 1Hz. This value was also confirmed by the analysis in frequency of the fluid dynamic pressure and we believe it is related to the sail wake displacement. The noise associated to high frequencies (from 10 to 80 Hz) grows downstream as a consequence of the breaking up process of the eddies in the wake.

The quadrupole term appears as the leading term in the calculation of hydroacoustic noise. For this reason in the close future we plan to address further investigations about BB2 submarine acoustic signature, taking into account also the effect of the ocean stratification. In fact, it is well known (Pal *et al.*, 2016; Jones & Paterson, 2018; Armenio & Sarkar, 2002) that stratification strongly influences the distributions of Reynolds stresses in the wake and, as a consequence of this, it could affect the resulting noise. To make the model even more realistic, the marine propeller should be then considered. As shown in Cianferra *et al.* (2019*b*), the propeller creates a persistent turbulent wake with a well-defined shape that interacts with the wake of the submerged advancing body. Moreover, to perform simulations at (as much as possible) higher Reynolds number will be of fundamental importance.

In the end, the combination of WM-LES and FW-H equation (formulation 1D) reveals to be a powerful tool to perform accurate numerical investigation and design optimizations, at reasonable computation cost, for a wide range of engineering problems.

List of Figures

List of Tables

Bibliography

Alin, N., Bensow, R., Fureby, C., Huuva, T. & Svennberg, U. 2010 Current capabilities of des and les for submarines at straight course. *Journal of Ship Research* **54**, 184–96.

Anderson, B., Chapuis, M., Erm, L., Fureby, C., Giacobello, M., Henbest, S., Jones, D., Jones, M., Kumar, C., Liefvendahl, M., Manovski, P., Norrison, D., Quick, H., Snowden, A., Valiyff, A., Widjaja, R. & Woodyatt, B. 2012 Experimental and computational investigation of a generic conventional submarine hull form. In *29th Symposium on Naval Hydrodynamics*. Gothenburg, Sweden.

Armenio, V. & Sarkar, S. 2002 An investigation of stably stratified turbulent channel flow using large-eddy simulation. *Journal of fluid mechanics* **459**.

Bettle, M. C., Gerber, A. G. & Watt, G. D. 2009 Unsteady analysis of the six dof motion of a buoyantly rising submarine. *Computers & Fluids* **38** (9), 1833–49.

Bhushan, S., Alam, M. F. & Walters, D. K. 2013 Evaluation of hybrid rans/les models for prediction of flow around surface combatant and suboff geometries. *Computers & Fluids* **88**, 834 –49.

Bose, S., Moin, P. & You, D. 2010 Grid-indipendent large-eddy simulation using explicit filtering. *Physics of fluid* .

Bradshaw, P. & Huang, G. P. 1995 The law of the wall in turbulent flow. *Proc. R. Soc. Lond.* **451**, 165–188.

BIBLIOGRAPHY

Broglia, R., Dubbioso, G., Durante, D. & Di Mascio, A. 2013 Simulation of turning circle by cfd: analysis of different propeller models and their effect on manoeuvring prediction. *Applied Ocean Research* **39**, 1–10.

Broglia, R., Dubbioso, G., Durante, D. & Mascio, A. Di 2015 Turning ability analysis of a fully appended twin screw vessel by cfd. part i: Single rudder configuration. *Ocean Engineering* **105**, 275–86.

Broglia, R., Zaghi, S., Muscari, R. & Salvadore, F. 2014 Enabling hydrodynamics solver for efficient parallel simulations. In *International Conference on High-Performance Computing & Simulation (HPCS)*, pp. 803–10. Bologna, Italy.

Carrica, P. M., Kerkvliet, M., Quadvlieg, F., Pontarelli, M. & Martin, J. E. 2016 Cfd simulations and experiments of a maneuvering generic submarine and prognosis for simulation of near surface operation. In *31st Symposium on Naval Hydrodynamics*. Monterey, CA, USA.

Carrica, P. M., Kim, Y. & Martin, J. E. 2018 Near surface operation of a generic submarine in calm water and waves. In *32nd Symposium on Naval Hydrodynamics*. Hamburg, Germany.

Casalino, D. 2003 An advanced time approach for acoustic analogy predictions. *Journal of Sound and Vibration* **261**, 583–612.

C.Groves, N., Huang, T. T. & Chang, M. S. 1989 Geometric characteristcs of the darpa suboff models. *Tech. Rep.* DTRC/SHD-1298-01. David Taylor Research Center, Bethesda, MD.

Chase, N. & Carrica, P. M. 2013 Submarine propeller computations and application to self-propulsion of darpa suboff. *Ocean Engineering* **60**, 68 – 80.

Chase, N., Michael, T. & Carrica, P.M. 2013 Overset simulation of a submarine and propeller in towed, self-propelled and maneuvering conditions. *International Shipbuilding Progress* **60**, 171–205.

Cianferra, M. 2017 Use of the Ffowcs Williams and Hawkings equation for the prediction of hydroacoustic noise for single-phase and cavitating flows. PhD thesis, School of Earth Science and Fluid Mechanics, University of Trieste.

BIBLIOGRAPHY

Cianferra, M., Ianniello, S. & Armenio, V. 2019*a* Assessment of methodologies for the solution of the Ffowcs Williams-Hawkings equation using les of incompressible single-phase flow around a finite-size square cylinder. *Journal of Sound and Vibration* **453**, 1–24.

Cianferra, M., Petronio, A. & Armenio, V. 2019*b* Non-linear noise from a ship propeller in open sea condition. *Ocean Engineering* **191**, 1064–74.

Curle, N. 1955 The influence of solid boundaries upon aerodynamic sound. *Proceedings of Royal Society* **A231** (1187), 505–14.

Davidson, P. A. 2004 *Turbulence. An introduction for scientists and engineers.* Oxford university press.

Davidson, P. A., Kaneda, Y., Moffatt, K. & Sreenivasan, K. R. 2011 *A Voyage Through Turbulence*. Cambridge University Press.

Di Mascio, A., Broglia, R. & Muscari, R. 2007 On the Application of the One-Phase Level Set Method for Naval Hydrodynamic Flows. *Computers & Fluids* **36** (5), 868–86.

Dubbioso, G., Broglia, R. & Zaghi, S. 2017 Cfd analysis of turning abilities of a submarine model. *Ocean Engineering* **129**, 459–79.

Eitel-Amor, G., Örlü, R. & Schlatter, P. 2014 Simulation and validation of a spatially evolving turbulent boundary layer up to Reθ= 8300. *International Journal of Heat and Fluid Flow* **47**, 57–69.

Farassat, F. 1975 Theory of noise generation from moving bodies with an application to helicopter rotors. *NASA Technical Report* **R-451**.

Farassat, F. 1981 Linear acoustic formulas for calculation of rotating blade noise. *AIAA Journal* **19(9)**, 1122–30.

Farassat, F. 2007 Derivation of formulation 1 and 1a of farassat. *Tech. Rep.*. NASA TM-2007-214853.

BIBLIOGRAPHY

Farassat, F. & Succi, G. P. 1980 A review of propeller discrete frequency noise prediction technology with emphasis on two current methods for time domain calculations. *Journal of Sound and Vibration* **71(3)**, 399–419.

Ffowcs-Williams, J.E. & Hawkings, D.L. 1969 Sound generation by turbulence and surfaces in arbitrary motion. *Philosophical Transaction of Royal Society* **A264** ((A1151)), 321–42.

Fischer, J., Rowan, M., Jacquemin, P., Lamos, D., Vargas, O., Malcolm, J., Skvortsov, A. & Doolan, C. 2017 Wind tunnel flow noise measurements using a random design acoustic array. In *Proceedings of ACOUSTICS 2017*. Perth, Australia.

Francescantonio, P. Di 1997 A new boundary integral formulation for the prediction of sound radiation. *J. Sound Vib.* **202**, 491–509.

Fureby, C., Anderson, B., Clarke, D., Erm, L., Henbest, S., Giacobello, M., Jones, D., Nguyen, M., Johansson, M., Jones, M., Kumar, C., Lee, S.-K., Manovski, P., Norrison, D., Petterson, K., Seil, G., Woodyatt, B. & Zhu, S. 2016 Experimental and numerical study of a generic conventional submarine at 10° yaw. *Ocean Engineering* **116**, 1 – 20.

G. Dubbioso, D. Durante, A. Di Mascio & Broglia, R. 2016 Turning ability analysis of a fully appended twin screw vessel by cfd. part ii: Single vs. twin rudder configuration. *Ocean Engineering* **117**, 259–71.

George, W. K. 1989 The self-preservation of turbulent flows and its relation to initial conditions and coherent structures. In *Advances in Turbulence*, pp. 39–73. Hemisphere Press.

Germano, M., Piomelli, U., Moin, P. & Cabot, W. H. 1991 A dynamic subgrid-scale eddy viscosity model. *Physics of Fluids A: Fluid Dynamics* **3**.

Girimaji, S. S. & Suman, S. 2012 Partially Averaged Navier-Stokes (PANS) method for turbulence simulations: Theory and practice. In *Progress in Hybrid RANS-LES Modelling*, pp. 29–43. Berlin, Heidelberg: Springer Berlin Heidelberg.

BIBLIOGRAPHY

GOURLAY, M. J., ARENDT, S. C., FRITTS, D. C. & WERNE, J. 2001 Numerical modeling of initially turbulent wakes with net momentum. *Physics of Fluids* **13** (12), 3783–802.

HUANG, T., LIU, H. L., GROVES, N., FORLINI, T., BLANTON, J. & GOWING, S. 1992 Measurements of flows over an axisymmetric body with various appendages in a wind tunnel: the darpa suboff experimental program. In *In Proceedings of the 19th Symposium on Naval Hydrodynamics*. National Academy Press.

IANNIELLO, S. 2007 New perspectives in the use of the Ffowcs Williams-Hawkings equation for aeroacoustic analysis of rotating blades. *Journal of Fluid Mechanics* **570** (20), 79–127.

IANNIELLO, S. 2016 The Ffowcs Williams-Hawkings equation for hydroacoustic analysis of rotating blades. The rotpole. *Journal of Fluid Mechanics* **797**, 345–88.

IANNIELLO, S., MUSCARI, R. & DI MASCIO, A. 2013 Ship underwater noise assessment by the acoustic analogy. Part i: Nonlinear analysis of a marine propeller in a uniform flow. *Journal of Marine Science and Technology* **18**.

ISSA, R.I, GOSMAN, A.D & WATKINS, A.P 1986 The computation of compressible and incompressible recirculating flows by a non-iterative implicit scheme. *Journal of Computational Physics* **62** (1), 66–82.

JIMÉNEZ, J. M., HULTMARK, M. & SMITS, A. J. 2010a The intermediate wake of a body of revolution at high reynolds nnumbers. *J. Fluid Mech.* **659**, 516–39.

JIMÉNEZ, J. M., REYNOLDS, R. T. & SMITS, A. J. 2010b The effect of the fins on the intermediate wake of a submarine model. *ASME J. Fluids Eng.* **132(3)**.

JOHANSSON, P. B. V. & GEORGE, W. K. 2001 On the effect of finite Reynolds number and initial conditions on the axisymmetric wake. In *Proceedings of the Second International Symposium on Turbulence and Shear Flow Phenomena*, pp. 323–28.

JOHANSSON, P. B. V., GEORGE, W. K. & GOURLAY, M. J. 2003 Equilibrium similarity, effects of initial conditions and local reynolds number on the axisymmetric wake. *Physics of Fluids* **15** (3), 603–17, arXiv: https://doi.org/10.1063/1.1536976.

Jones, M. & Paterson, E. 2018 Influence of propulsion type on the stratified near wake of an axisymmetric self-propelled body. *Journal of Marine Science and Engineering* **6** (2), 46.

Joubert, P. N. 2004 Some aspects of submarine design part 1 - hydrodynamics, dsto report dsto-tr-1622. *Tech. Rep.*. DSTO Melbourne, Australia.

Joubert, P. N. 2006 Some aspects of submarine design part 2 - shape of a submarine 2026, dsto report dsto-tr-1920. *Tech. Rep.*. DSTO Melbourne.

Kim, J., Moin, P. & Moser, R. 1986 Turbulence statistics in fully developed channel flow at low reynolds number. *Journal of Fluid Mechanics* .

Kumar, C., Manovski, P. & Giacobello, M. 2012 Particle image velocimetry measurements on a generic submarine hull form. In *18th Australasian Fluid Mechanics Conference.*

Kumar, P. & Mahesh, K. 2018 Large-eddy simulation of flow over an axisymmetric body of revolution. *J. Fluid Mech.* **853**, 537–63.

Larsson, J., Kawai, S., Bodart, J. & Bermenio-Moreno, I. 2016 Large eddy simulation with modeled wall-stress:recent progress and future directions. *Bulletin of the JSME. Mech. Eng. Review* **3** (1).

Launder, B. E. & Spalding, D. B. 1974 The numerical computation of turbulent flows. *Computer Methods in Applied Mechanics and Engineering* **3** (2), 269–89.

Lee, S. K., Manovski, P. & Kumar, C. 2019 Wake of a cruciform appendage on a generic submarine at 10° yaw. *Journal of Marine Science and Technology* .

Lighthill, M. J. 1952 On sound generated aerodynamically. i general theory. *Proceedings of Royal Society* **A 211** (11079), 564–87.

Lilly, D. K. 1992 A proposed modification of the germano subgrid-scale closure method. *Physics of Fluids A: Fluid Dynamics* .

Lyrintzis, A. S. 1994 Review: The use of kirchhoff's method in computational aeroacoustics. *Journal of Fluids Engineering* **116** (4), 665–76.

Martin, J. E., Michael, T. & Carrica, P. M. 2015 Submarine maneuvers using direct overset simulation of appendages and propeller and coupled cfd/potential flow propeller solver. *Journal of Ship Research* **59**, 31–48.

Menter, F. & Egorov, Y. 2010 The Scale-Adaptive Simulation method for unsteady turbulent flow predictions. Theory and model description. *Flow Turbulence Combust* **85**, 113–38.

Morino, L. 1974 A general theory of unsteady compressible potential aerodynamics. *Tech. Rep.*. NASA-CR-2464, TR-73-01, TR-72-01.

Mukha, T. 2018 Modelling techniques for large-eddy simulation of wall-bounded turbulent flows. PhD thesis, Uppsala Univeristy.

Mukha, T. & Liefvendahl, M. 2015 Large-eddy simulation of turbulent channel flow. *Tech. Rep.*. Uppsala University.

Najafy-Yazdi, A., Bres, G. A. & Mongeau, L. 2010 An acoustic analogy formulation for moving sources in uniformly moving media. *Proc. R. Soc.* **467**, 144–65.

Nicoud, F. & Ducros, F. 1999 Subgrid-scale stress modelling based on the square of the velocity gradient tensor. *Flow Turbul. Combust.* **62** (3), 183–200.

Norrison, D., Sidebottom, W., Anderson, B., Petterson, K. & Fureby, C. 2016 Numerical study of a self-propelled conventional submarine. In *31st Symposium on Naval Hydrodynamics*. Monterey, CA, USA.

Overpelt, B., Nienhuis, B. & Anderson, B. 2015 Free running manoeuvring model tests on a modern generic ssk class submarine (bb2). In *Pacific International Maritime Conference*. Sydney, Australia.

Pal, A., Sarkar, S., Posa, A. & Balaras, E. 2016 Regeneration of turbulent fluctuations in low-froude-number flow over a sphere at a Reynolds number of 3700. *Journal of Fluid Mechanics* **804**, R2.

BIBLIOGRAPHY

Patankar, S. V. 1980 *Numerical Heat Transfer and Fluid Flow*. Taylor & Francis.

Petterson, K., Fureby, C., Liefvendahl, M., Norrison, D. & Sidebottom, W. 2018 Les of a full-scale self-propelled conventional submarine at ±10 yaw. In *32nd Symposium on Naval Hydrodynamics*. Hamburg, Germany.

Piomelli, U. & Balaras, E. 2002 Wall-layer models for large-eddy simulations. *Annual Review of Fluid Mechanics* **34** (1), 349–74.

Piomelli, U., Streett, C. L. & Sarkar, S. 1997 On the computation of sound by large-eddy simulations. *Journal of Engineering Mathematics* **32**, 217–36.

Pope, S. B. 2000 *Turbulent Flows*. Cambridge university press.

Posa, A. & Balaras, E. 2014 Model-based near-wall reconstructions for immersed-boundary methods. *Theor. Comput. Fluid Dyn* **28**, 473–83.

Posa, A. & Balaras, E. 2016 A numerical investigation of the wake of an axisymmetric body with appendages. *J. Fluid Mech.* **792**, 470–98.

Posa, A. & Balaras, E. 2020 A numerical investigation about the effects of Reynolds number on the flow around an appended axisymmetric body of revolution. *J. Fluid Mech.* **884** (A41).

Quick, H., Widjaja, R., Anderson, B., Woodyatt, B., Snowden, A. & Lam, S. 2012 Phase i experimental testing of a generic submarine model in the dsto low speed wind tunnel. technical note tn-1101. *Tech. Rep.*. Defence Science and Technology, Australia.

Quick, H. & Woodyatt, B. 2014 Phase ii experimental testing of a generic submarine model in the dsto low speed wind tunnel. technical note tn-1274. *Tech. Rep.*. Defence Science and Technology, Australia.

Renilson, M. 2018 *Submarine Hydrodynamics, 2nd edn.*. Springer, Berlin.

Robinson, S. K. 1991 Coherent motions in the turbulent boundary layer. *Annu. Rev. Fluid Mech.* pp. 601–39.

Salsa, S. 2008 *Partial differential equations in action*. Springer.

SPALART, S. F. 2009 Detached-eddy simulation. *Annual Review of Fluid Mechanics* **41** (1), 181–202.

TENNEKES, H. & LUMLEY, J. 1972 *A First Course in Turbulence*. Cambridge, Mass. : MIT Press.

TOWNSEND, A. A. 1956 *The Structure of Turbulent Shear Flow*, , vol. 1(5). Cambridge University Press.

TOXOPEUS, DR IR S.L. 2017 Report no. 29347-8-rd. *Tech. Rep.*. Marin.

WILCOX, D. C. 1994 *Turbulence Modeling for CFD*. University of Michigan.

YANG, XIA., PARK, GI. & MOIN, P. 2017 Log-layer mismatch and modeling of the fluctuating wall stress in wall-modeled large-eddy simulations. *Phys Rev Fluids* .